

## Supplemental Material

### Deep magma mobilization years before the 2021 Fagradalsfjall eruption, Iceland

**M. Kahl<sup>1</sup>, E.J.F. Mutch<sup>2</sup>, J. Maclennan<sup>3</sup>, D.J. Morgan<sup>4</sup>, F. Couperthwaite<sup>5</sup>, E. Bali<sup>6,7</sup>, T. Thordarson<sup>7</sup>, G.H. Guðfinnsson<sup>6</sup>, R. Walshaw<sup>4</sup>, I. Buisman<sup>3</sup>, S. Buhre<sup>8</sup>, Q.H.A. van der Meer<sup>6</sup>, A. Caracciolo<sup>6</sup>, E.W. Marshall<sup>6</sup>, M.B. Rasmussen<sup>6</sup>, C.R. Gallagher<sup>6</sup>, W.M. Moreland<sup>6</sup>, Á. Höskuldsson<sup>6</sup>, R.A. Askew<sup>9</sup>**

<sup>1</sup>*Institut für Geowissenschaften, Universität Heidelberg, 69120 Heidelberg, Germany*

<sup>2</sup>*Lamont-Doherty Earth Observatory, Columbia University, New York, 10964, USA*

<sup>3</sup>*Department of Earth Sciences, University of Cambridge, Cambridge, CB2 3EQ, UK*

<sup>4</sup>*School of Earth & Environment, University of Leeds, Leeds LS2 9JT, UK*

<sup>5</sup>*CEOAS, Oregon State University, Corvallis, Oregon 97331, USA*

<sup>6</sup>*Institute of Earth Sciences, University of Iceland, 101 Reykjavik, Iceland*

<sup>7</sup>*Faculty of Earth Sciences, University of Iceland, 101 Reykjavik, Iceland*

<sup>8</sup>*Institut für Geowissenschaften, Johannes Gutenberg Universität Mainz, 55128 Mainz, Germany*

<sup>9</sup>*Icelandic Institute of Natural History, 210 Garðabær, Iceland*

\*Corresponding author. Email: [Maren.Kahl@geow.uni-heidelberg.de](mailto:Maren.Kahl@geow.uni-heidelberg.de)

#### **This PDF file includes:**

Materials and Methods

Supplementary Text

Figs. S1 to S56

Captions for Data S1 to S8

Supplementary materials reference list

## Materials and Methods

### 1. Analytical Methods

#### 1.1 Electron microprobe analysis

Fresh olivine macrocrysts in the size range 2.0-1.0 mm and 1.0-0.5 mm were hand-picked from crushed lava flow samples erupted on March 20, March 23 and from airfall tephra samples erupted on April 28 and May 06 of the recent eruption at Fagradalsfjall. Picked olivine macrocrysts were mounted in epoxy resin for microanalysis. High-resolution BSE images of compositionally zoned olivine macrocrysts were taken using the JEOL JXA-8200 electron probe microanalyzer at the Institute of Geosciences at Mainz University. BSE images were taken using an acceleration voltage of 20kV, 20nA beam current, a working distance of 11mm and a scanning rate of 10 (~80s). Greyscale intensity profiles perpendicular to crystal faces were extracted from BSE images using the ImageJ software to pre-select locations for analytical traverses suitable for diffusion modelling. The grayscale values were calibrated to the major element compositions (Costa and Morgan, 2010) obtained from analyses of the same olivine crystal using electron microprobe analysis.

A total of 182 concentration profiles of major and minor elements (Si, Fe, Mg, Mn, Ca, Ni, Cr, Al, Ti) from 138 olivine crystals were acquired using the JEOL JXA-8200 electron probe microanalyzer. Compositional transects were analysed using a 20kV accelerating voltage, 40nA beam current, and 2 $\mu$ m spot size, with spacing of ~4-17 $\mu$ m. Peak count times for olivine were set to 30s for Mg, 36s for Si, Ti, Al, 50s for Ca, Mn, Fe and 80s for Ni. Background count times were 20s for Mg, 30s for Si, 32s for Ti, 36s for Al, Fe, 40s for Cr, Ca, Mn and 80s for Ni. Primary standards used for calibration were: Al<sub>2</sub>O<sub>3</sub> for Al; Cr<sub>2</sub>O<sub>3</sub> for Cr; Fe<sub>2</sub>O<sub>3</sub> for Fe; NiO for Ni; Rhodonite for Mn; TiO<sub>2</sub> for Ti; Wollastonite for Ca; Olivine and kSt18 (Springwater meteorite) for Mg and Si. Internal data reduction for olivine analysis was performed using the ZAF quantitative correction program. Precision was estimated by repeat measurements of the Olivine standard during each session. Two sigma precisions are within 0.70 wt% for SiO<sub>2</sub>, 0.14 wt% for FeO, 0.46 wt% for MgO and 0.01 wt% for MnO, Ni and CaO. Olivine forsterite content [ $Fo = 100 \times Mg / (Mg + Fe^{2+})$ ] was determined with a precision of  $2\sigma = \pm 0.14$  mol% (n=182).

77 rim-core profiles in plagioclase macrocrysts from the mounts of the material sampled from March 20, March 21, March 23, April 02, April 28 and May 06 have been acquired on the Cameca SX100 at the University of Cambridge. The elements Si, Al, Ca, Na, Fe, Mg, K, Ti and Mn were analysed with a method similar to that employed by Mutch et al. (2021). Plagioclase profiles were measured with a focussed 1  $\mu$ m beam and with an accelerating voltage of 15 kV and a working current of 10 nA for major (Ca, Al, Si, Na) and minor elements (Mg, Ti, K, Fe). On peak count times of 20 s were used for major elements and 90–110 s for minor and trace elements, with half count times off peak. The data was collected in long batch acquisitions over 9 analytical sessions. A secondary standard of Labradorite - 115900 (Smithsonian) was analysed multiple times during each batch, typically with clusters of 6-8 points taken once every 12-15 hours. This data was used to check for drift in the calibration and to assess the overall precision and accuracy of the results. No drift corrections were applied. The overall precision (1 $\sigma$ ) across all runs for XAn is 0.9 mol%, with variation in individual sessions being closer to 0.3 mol%. The Mg shows a relative standard deviation of 5.9% across all sessions and Fe is 3.6%. K, Mn and Ti

show relative standard deviations above 15% and are not discussed further. The BSE scans showed that most crystals had rims of lower anorthite content than the cores and the point spacing in the profiles was adapted to capture the likely spatial gradients in Mg expected to be found close to the rims. Individual profiles were typically 500 microns long and the spatial resolution in the 200 microns at the rim was 5 microns, while spacing increased up to 15 microns further into the crystal cores.

## 1.2 Electron backscatter diffraction (EBSD).

Diffusive anisotropy in olivine was corrected for by characterizing the orientation of the crystallographic a-, b- and c-directions in olivine using electron backscatter diffraction (EBSD) mapping (Costa et al., 2004; Prior et al., 1999) on the FEI Quanta 650 FEGSEM at the University of Leeds Electron Microscopy and Spectroscopy Centre (LEMAS) equipped with an Oxford Instruments Symmetry® EBSD detector. EBSD data were acquired using an accelerating voltage of 20.0 kV, a working distance of 28 mm, a specimen tilt of 69.8° and a detector insertion distance of 158.9 mm. Data collection and pattern indexing were performed using the AZtecSynergy software. Orientation maps of individual olivine crystals (Kahl et al., 2017) were collected using a step size of 10µm. EBSD data clean up and post-processing were performed using the AZtecCrystal post-processing software enabling the extraction of thousands of orientation measurements from single orientation maps of individual crystals. Measured Euler angles were converted into trends and plunges of the olivines crystallographic a-, b- and c-axis directions using an Excel™ spreadsheet developed by Dr. D. Morgan (University of Leeds, UK). The low reported anisotropy of Mg diffusion in plagioclase means that no EBSD data were collected from plagioclase mounts (Van Orman et al., 2014; Faak et al., 2013).

## 2. Diffusion modelling

### 2.1 Olivine

180 time estimates from modelling the diffusive relaxation of Fe-Mg zoning profiles in 123 olivine crystals have been obtained using Autodiff, an objective, rapid-modelling approach that exploits the self-similarity of one-dimensional diffusion profiles with similar boundary conditions to allow timescales to be determined quickly (Couperthwaite et al., 2021 and 2020; Pankhurst et al., 2018; Allan et al., 2017; Hartley et al., 2016). The number of independent estimates (n=180) is larger than the number of crystals modelled (n=123) because some crystals record multi-stage events, which were modelled stepwise (Fig. 2). Lava olivines were modelled using 1236±20°C and 5±1.3 kbar for the crystal interiors and 1200±20°C and 2±1.3 kbar for the rims. Tephra olivines from April 28 and May 06 were modelled using temperatures of 1230±20°C and 1220±20°C and pressures of 5.2±1.3 and 4.5±1.3 kbar, respectively. These selected temperatures and pressures are consistent with constraints using OPAM (olivine-plagioclase-augite-melt) barometry (Hartley et al., 2018; Yang et al., 1996) and liquid-only thermometry (Putirka, 2008) in groundmass glasses and melt inclusions of primitive macrocryst cores. For all models, oxygen fugacity conditions of  $\Delta \log fO_2$  (QFM) -0.3 were used in accordance with olivine-spinel oxybarometry results. A full account of the applied geothermobarometers, oxybarometers and filtering criteria is provided in **section 3. Estimation of intensive parameters.**

*Autodiff* allows step or externally-buffered models, the choice of which was based on the shape of the profile and its position in the crystal. Some of the following method description is excerpted from Couperthwaite et al. (2020) with appropriate expansions for the modelling undertaken here. For one-dimensional diffusion under the same conditions of composition dependence, profiles differing in terms of diffusion time are self-similar and differ only in terms of the profile width. *Autodiff* contains a database of profiles calculated with a full range of composition dependences. There are two versions of *Autodiff* relating to two different sets of boundary conditions. The first is a stranded profile, also known as a square-wave, where interdiffusion is contained entirely within the crystal between two domains of differing but initially uniform forsterite content. The second set of boundary conditions is an edge-buffered scenario, where an initially homogeneous crystal is changed by diffusive interaction with melt at the crystal margin, without any considerations of crystal growth. The higher diffusivity in the melt is represented through a fixed composition at the external margin of the crystal.

When employing *Autodiff* models, the boundary conditions – the inner and outer values of forsterite for the modelling – specifically determine which profile within the database is most appropriate based on the magnitude of compositional contrast. Additional input parameters of crystal orientation and traverse direction, the magmatic residence temperature and ambient  $fO_2$  – determine the precise value of diffusivity for the traverse. Both the database curve and the observed crystal profile are measured, in *Autodiff* the model looks at the central 60% of the compositional range between the two boundary condition values (between the 20<sup>th</sup> and 80<sup>th</sup> percentiles). This then leads to a stretch factor that can be determined by the width ratio of the two profiles (natural profile width over database synthetic width), and which is used as a multiplier to overlay the database profile onto the observed profile.

As the database is calculated under known conditions of diffusivity, composition dependence and time, and the diffusivity in the natural sample can be determined using the full set of input parameters, we can solve for the timescale by relating the absolute amount of diffusion in each instance with the stretch factor.

$$D_{Magma}t_{natural} = F^2 D_{synthetic}t_{database}$$

Which rearranges to

$$t_{natural} = \frac{F^2 D_{synthetic}t_{database}}{D_{Magma}}$$

Therefore, the stretch factor combined with the known amount of diffusion in the database and a constraint on the natural diffusivity allows the timescale to be simply determined from a set of known values. The modelling approach is rapid, as all of the diffusion math is encapsulated in a pre-calculated database, and it is objective, since the appropriate boundary conditions selected for modelling are derived from the profile to be fitted. It is also worth noting that the method is also limited in that it only considers simple scenarios of diffusion, and any degree of mismatch can be considered to represent a degree of complexity in natural scenarios (e.g. changing boundary conditions, crystal growth and other situations where diffusion is convolved with another process) that the modelling is not capturing. Further discussion of this is discussed in depth in Couperthwaite et al. (2020 and 2021).

Diffusivities are calculated using the updated (corrected) version of the Fe-Mg diffusion coefficients obtained by Dohmen and Chakraborty (2007) and Dohmen et al. (2007) as quoted in

Chakraborty (2010), accounting for composition dependence, anisotropy, oxygen fugacity and potentially variable diffusion mechanism. Uncertainties can be propagated in several different ways. It is worth noting that the uncertainties in the diffusion expression, usually of Arrhenian form:

$$D = e^{\frac{-\Delta H}{RT}}$$

...are not independent. Specifically,  $D_0$  and  $-\Delta H/R$  can be considered as the y-axis intercept and gradient, respectively, of the straight line of experimental diffusivity values plotted on a  $\text{Log}_{10}$  Diffusivity versus  $1/T(\text{K})$  diagram. As such, uncertainties in  $D_0$  and  $\Delta H$  have to be covaried and are not completely independent.

Treating them as wholly interdependent and combining 1 sigma values appropriately to produce extreme bounds on diffusivity, combined with 1 sigma temperature uncertainties gives an uncertainty for these conditions of  $\sim 0.31$  log units. Due to combining extremes, this effectively explores a larger range than strictly 1 sigma, and is a worst case scenario estimate.

A more sophisticated statistical treatment which separates independent and interdependent aspects, can use a Monte-Carlo approach to further factor in uncertainties from analytical conditions, thermometry, oxygen fugacity, BSE to microprobe calibration, the quality and spatial resolution of the data and the resolution of the fits. Even with conservatively large values – thus likely overestimating the uncertainty – the values come in at one sigma uncertainty of  $\sim 0.28$  log units, representing how dominant the diffusivity and temperature uncertainties are.

### 2.1.1 Olivine timescale correction for multi-stage thermal history

Following reviewer suggestion, a correction was undertaken for the differential thermal histories of crystals with both inner zones (modelled at  $1236^\circ\text{C}$ ) and outer rim zones (modelled at  $1200^\circ\text{C}$ ). The initial modelling considered isothermal conditions with any inner and outer zones modelled independently due to the nature of the model used (Autodiff, used in several other studies as cited). The correction necessary (i.e., that outer zones diffuse under cooler conditions, and would mean that the inner profile represents diffusion under two different temperature regimes) causes the inner profiles to become slightly older, by an amount equivalent to the difference in timescale between running the outermost zone at the temperature conditions of the inner region ( $1236^\circ\text{C}$ ) and the temperature used for the outer region ( $1200^\circ\text{C}$ ).

Considering an example:

- Consider a crystal with an inner timescale of 1000 days at  $1236^\circ\text{C}$ , and a rim of 100 days at  $1200^\circ\text{C}$ .
- The diffusion speed at  $1236^\circ\text{C}$  is 1.7414 times faster than at  $1200^\circ\text{C}$ , meaning that a rim zone age of 100 days at  $1200^\circ\text{C}$  is equivalent in diffusion extent to  $\sim 57$  days at  $1236^\circ\text{C}$ .
- Therefore, rather than 1000 days at  $1236^\circ\text{C}$ , the inner boundary has experienced (1000-57) or 943 days at  $1236^\circ\text{C}$  followed by another 100 days at  $1200^\circ\text{C}$  whilst the outer rim annealed, for a total timescale of 1043 days.

- In effect therefore, each crystal with an inner and outer zone has had its inner zone timescale increased by  $(0.43 \times \text{outer zone timescale})$  to account for this differential history.

This means that we can account for this differential thermal history with an offline correction where the innermost zones get older by an amount equivalent to 0.43 times the timescale of the outermost zone. The correction ranges therefore from 2 days up to 74 days with a mean of 16 days.

For many crystals, the correction is proportionally very small due to the large difference in timescale between inner and outer regions – inner regions have average timescales of  $\sim 500$  days. For a minority of crystals ( $n=6$ ) the timescale change can be over 10%, and so for completeness, for all crystals where we have two boundaries we have performed this correction. We provide the corrected timescale in supplementary data table S5 alongside the original timescale data. All changes have been factored into figure 3 displaying the updated olivine diffusion dataset.

## 2.2 Plagioclase

The DFENS method described by Mutch et al. (2021) was used to model diffusion of Mg in 51 plagioclase crystals. This approach solves the diffusion equation that minimizes gradients in the chemical potential of Mg in plagioclase (Costa et al., 2003). DFENS uses a flexible finite element solver (FEniCS; Alnæs et al., 2015) for the forward problem and a Bayesian (PyMultiNest; Buchner et al., 2014; Feroz et al., 2009) approach to explore the range of model parameters that provide acceptable fits to the observations. This approach is computationally intensive but gives powerful constraints on the uncertainty structure and trade-offs in the parameters.

As with all diffusion models, it is necessary to provide initial and boundary conditions for the Mg in the profile. The zonation of anorthite content in plagioclase, which develops during growth at variable P-T-X and undergoes negligible diffusive modification over the timescales of interest, provides an important constraint on suitable initial conditions. These were set under the assumption that the high-anorthite cores of the plagioclase macrocrysts were initially in equilibrium for Mg. The partitioning relationship for this magmatic system was refined using the long core profiles in crystals which had sufficient variation in anorthite content to allow the influence of anorthite content on the Mg partitioning to be established. This follows the approach of Mutch et al. (2021), and established an  $A_{\text{Mg}}$  parameter of -72.8.

Diffusion of trace elements in plagioclase, such as Mg, mostly rely on partitioning behaviour, and need not require the growth of new anorthite zones. The change in the composition and temperature of the exterior liquid is more than sufficient to create a chemical potential gradient in the plagioclase that induces trace element diffusion. The changing conditions at the exterior of the crystal created by mush disaggregation exert a change in boundary conditions which we can use in the modelling.

In some profiles, minimal or no rim overgrowth had taken place on the face of crystal against the glass. Some of these overgrowths may have been too thin to sample given the  $5 \mu\text{m}$  spatial resolution of our profiles. In others, a rim of lower anorthite content up to 100 microns was present. Rimless crystal faces were prominent in tephra samples, whilst crystals with rims were more common in quenched lava flow samples. These observations suggest that rim growth

dominantly took place in the lava flow. This is supported by the fact that the lava flow groundmass glass is in equilibrium with An<sub>79</sub>. We have therefore assumed that diffusion gradients of Mg observed in the crystal cores developed prior to rim growth, and have thus modelled all of the profiles without the rims. This modelling approach captures the final diffusion event prior to rim growth (i.e. no additional zones in the core were modelled). For each crystal we plotted up the equivalent of ‘activity’ profiles, calculated by using:

$$a_{\text{Mg}} = RT \ln C_{\text{Mg}} - A_{\text{Mg}} X_{\text{An}} - B_{\text{Mg}}$$

where  $C_{\text{Mg}}$  is the Mg composition,  $X_{\text{An}}$  is anorthite content, and  $A_{\text{Mg}}$  and  $B_{\text{Mg}}$  are the slope and intercept of the plagioclase partitioning relationship (Mutch et al., 2021). For this we used the temperature and Mg composition of the tephra glass. This presented each profile in a form that looks like a standard diffusion gradient and made it easier to generate initial conditions. In this space, we defined step-like initial conditions with the plateaus defined by the equilibrated core and the edge. A Dirichlet boundary condition was applied to the outer boundary of the crystal using the edge composition.

Given the uncertainty surrounding the diffusion mechanism of Mg in plagioclase, we have opted to use two different diffusion coefficients: Faak et al. (2013) and Van Orman et al. (2014). The former has a dependence on the activity of silica ( $a_{\text{SiO}_2}$ ) and does not depend on anorthite content, whilst the latter shows a dependence on anorthite content. We used the parameterizations of these diffusion coefficients presented by equation 7 in Mutch et al. (2021). It has previously been shown by Mutch et al. (2021) that timescales estimated by the diffusion coefficient of Faak et al. (2013) provided the best match with olivine timescales from an Icelandic eruption where textural evidence indicates that the olivine and plagioclase timescales should be equivalent. Furthermore, Faak et al. (2013) used gabbroic powders for their experimental starting materials, which more closely match the bulk composition of Fagradalsfjall than the synthetic powders of Van Orman et al. (2014). For those reasons, we mostly focus on the timescales calculated using the diffusion coefficient of Faak et al. (2013), but include Van Orman et al. (2014) models for completeness.

Using the DFENS method (Mutch et al., 2021), we inverted for 10 parameters including: time, temperature,  $a_{\text{SiO}_2}$ ,  $A_{\text{Mg}}$ ,  $B_{\text{Mg}}$ , initial condition plateau compositions and the parameters that contribute to the diffusion coefficients. We assigned a log uniform prior to time ( $10^{-2}$  to  $10^4$  days) and independent Gaussian priors for temperature ( $1236 \pm 20$  °C) and the activity of silica ( $0.5 \pm 0.02$ ). These were based on independent estimates of these parameters and their 1 sigma uncertainties. The activity of silica was estimated using the 2<sup>nd</sup> of April tephra glass composition and the liquid's affinity for tridymite calculated in rhyolite-MELTSv1.02 (Gualda et al., 2012; Ghiorso and Sack, 1995). Uniform priors were used for the compositions that define the zones in the initial conditions. Multivariate Gaussian prior distributions were used for the partitioning ( $A_{\text{Mg}}$  of -72.8 and  $B_{\text{Mg}}$  of 15.9) and diffusion coefficient parameters of Mg-in-plagioclase based on their reported values and corresponding covariance matrices (Mutch et al., 2021).

In each forward model, linear Lagrange (Continuous Galerkin) finite elements were used to represent concentrations. A fixed Dirichlet boundary condition ( $C = C_0$  on  $x = 0$ ) was maintained at the crystal edge and a no-flux Neumann boundary condition was maintained in the crystal interior. The models therefore assumed that there was a semi-infinite melt reservoir. The standard number of mesh points for a 1D profile of length  $L$  was set to 500. The number of time steps between each realization was kept constant at 300. The nested sampling Bayesian inversion

was set with 400 livepoints, and the algorithm terminated once convergence of the marginal likelihood was attained. Convergence was generally attained after 3000 – 10000 Monte Carlo realizations. The posterior distributions that provide the best fit to the data (i.e. maximize the log likelihood function) were used for further statistical analysis. Typically the median values and 1 sigma uncertainties on these distributions were used for interpretation.

### **3. Estimation of intensive parameters**

#### **3.1 Geothermobarometry and oxybarometry**

Based on BSE imaging and electron microprobe analyses outermost rims of microphenocrysts commonly show textural and chemical equilibrium with groundmass glass compositions. Thus, pressure was calculated based on the olivine-augite-plagioclase-melt (OPAM; Hartley et al., 2018 Yang et al., 1996) barometer which shows the last equilibrium condition between the melt and its evolved crystal cargo. The uncertainty of these calculations is  $\pm 1.3$  kbar when pressures derived from silicate glass compositions had a probability fit of being on the 4-phase cotectic  $>0.8$  (Hartley et al., 2018). Pressures were also calculated based on evolved clinopyroxene rim – groundmass glass pairs for the first few days of the eruption using the calibration by Neave and Putirka (2017), applying the equilibrium criteria of Mollo et al. (2013) and Neave et al. (2019), where the uncertainty of the calculations are  $\pm 1.4$  kbar and,  $\pm 28^\circ\text{C}$ , respectively. Temperatures from the same glass compositions were determined by using eqn. 15 of Putirka (2008), using OPAM pressures and oxybarometry results as input parameters.

The results of OPAM barometry and related thermometry show that the groundmass glass last equilibrated with the crystal cargo in the pressure range of 0.6 to 2.7 kbars and in the temperature range of 1190 to 1210 °C in the initial stage of the eruption (samples collected in March). This pressure and temperature range was confirmed by the results of clinopyroxene-melt thermobarometry (1.0-1.9 kbars and 1185-1200 °C; Halldórsson et al., 2022). The calculated low pressures are in accordance with the development of a shallow dyke (0-8km) (probably beginning February 24<sup>th</sup>), as observed based on intense ground deformation and high seismicity in the weeks and days prior to the eruption (Sigmundsson et al., 2022). Groundmass glass composition in lavas however is affected by late-stage crystallization of microlites (fig. S2), therefore the calculated values might underestimate the real pressure and temperature where the diffusion in fact started. This is confirmed by olivine macrocryst rims being in chemical equilibrium with the tephra glass collected on 24<sup>th</sup> of April, instead of being in equilibrium with their respective groundmass glass. Thus, the intensive parameters for diffusion modelling were chosen to be on the higher end of the calculated temperatures and pressures (1200 °C and 2 kbars) in this period. For the late-April and early-May tephra samples (intense fire fountaining period) OPAM barometry reveals much higher equilibration pressures and thermometry shows somewhat higher equilibration temperatures with the crystal cargo, compared to those found in March. The groundmass glass last equilibrated with the crystal cargo in the pressure range of 4.4 (6<sup>th</sup> of May) to 5.2 (28<sup>th</sup> of April) kbars and in the temperature range of 1220 °C to 1230 °C (Halldórsson et al., 2022). The groundmass glass composition analysed in the tephra was in fact in chemical equilibrium with the majority of olivine rim compositions analysed in these samples (Fig. S2). Thus, for this period the intensive parameters for diffusion modelling were changed to 5.2 kbars and  $1230\pm 20$  °C for the samples from 28<sup>th</sup> of April and 4.5 kbars and  $1220\pm 20$  °C for the samples on the 6<sup>th</sup> of May.

### 3.2 Oxybarometry

Oxygen fugacity was calculated based on olivine-spinel pairs from a quenched lava sample erupted on March 21<sup>st</sup> using the oxybarometer of Nikolaev et al. (2016) with an experimental reproducibility of  $\Delta \log fO_2 \pm 0.5$ . Olivine-spinel pairs were assigned pressures of 2 kbar and temperatures of 1200°C for rims with  $<Fo_{87}$  and 2 kbar and 1240°C for cores with  $>Fo_{87}$  based on geothermobarometry results. Compositionally homogeneous olivine-spinel pairs give  $K_D^{Mg-Fe} [(Mg/Fe)_{olivine}/(Mg/Fe^{2+})_{spinel}]$  between 3.1 and 3.4, heterogeneous spinel and disequilibrium olivine-spinel pairs outside this range in  $K_D^{Mg-Fe}$  were discarded (Van der Meer et al., 2021). 26 equilibrium olivine-spinel pairs give  $\Delta \log fO_2$  between -0.1 and -0.6 with an average of -0.3, without a clear difference between cores and rims.

## 4. Seismic moment release

The earthquake magnitudes,  $M$ , were taken from the catalogue at <https://skjalftalisa.vedur.is> and the moment release for each event was calculated using the expression  $M_0 = 10^{[1.5 \times M + 9.1]}$  (eq. 4; Hanks & Kanamori, 1979). The cumulative moment release through time was then calculated and plotted.

## Supplementary Text

### 1. Geological background

The Reykjanes Peninsula (RP) in SW-Iceland links the Western Volcanic Zone (WVZ) and the South Iceland Seismic Zone (SISZ) of Iceland to the offshore Reykjanes Ridge (Fig. 1). It is taken to be highly oblique spreading segment, with an obliquity of 25-30° (Hreinsdóttir et al., 2001), with a plate motion of 17-19 mm/yr along left-lateral shear zone striking 80°E, including an extensional component of 7-9 mm/yr (Árnadóttir et al., 2008). This is expressed by a complex surface fracture pattern that includes a distinct zone of north-south trending strike-slip faults and associated N21-40°E fractures trending as the volcanic cone-rows (Clifton and Kattenhorn, 2006). The plate boundary goes onshore at the SW tip of the RP trending N80°E along the peninsula where it meets the Hengill triple junction and splits into the WVZ and the SISZ (Fig. 1; Árnadóttir et al., 2008). The RP features several northeast trending volcano-tectonic lineaments, also referred to as volcanic systems (Sæmundsson et al., 2020; Jakobsson et al., 2008; Thordarson and Höskuldsson, 2008; Clifton and Kattenhorn, 2006; Jakobsson et al., 1978). They are, from east to west, (i) Brennisteinsfjöll, (ii) Krýsuvík/Trölladyngja, (iii) Fagradalsfjall and (iv) Svartsengi and (v) Reykjanes (Fig. 1). These volcano-tectonic lineaments are highly oblique (40-60°) to the plate boundary and plate movement (Sæmundsson et al., 2020; Jakobsson et al., 1978). The oldest bedrock formations on the RP are exposed in its central and eastern parts and date back to the earlier glacial and interglacial periods of the Brunhes epoch ( $\leq 0.78$  Ma; Jónsson, 1978). These pre-Holocene sequences are comprised of subaqueous, subglacial and inter-glacial volcanic constructs which are partly obscured by the more recent postglacial vent constructs and lava flow fields.

Late-glacial pillow-lava ridges and post-glacial lava flow fields span the compositional range of picrite through olivine tholeiite to quartz-normative tholeiite and are products of both fissure and lava shield eruptions (Peate et al., 2009; Gee et al., 1998; Jakobsson et al., 1978). The picrites

(mean MgO = 13±4 wt%, range 10-28 wt%) are present as 12 formations of late-glacial pillow lava ridges and small-volume lava shields that crop out sporadically along the peninsula. The picrite pahoehoe lava shields have a collective volume = 0.7 km<sup>3</sup> and represent the oldest exposed post-glacial formations on the RP (Sæmundsson et al., 2016; Jónsson, 1978; Jakobsson et al., 1978). The RP features at least 14 olivine tholeiite lava shields (av. MgO = 8.5±0.6 wt%, range 7.3-9.85 wt%), which are typified by pahoehoe with macrocrysts of plagioclase and lesser olivine (Sinton et al., 2005; Gee et al., 1998; Jónsson, 1978; Jakobsson et al., 1978). The olivine tholeiite lava shields range in age from 2.5 to 14.1 ka and cover 700 km<sup>2</sup> of the RP with a collected volume 32 km<sup>3</sup>, which is about 75% of the of magma volume (43 km<sup>3</sup>) erupted on the RP in post-glacial time (Thordarson and Höskuldsson, 2008). The ages of the large volume (3.5-9.8 km<sup>3</sup>) shields range from 5.2 to 14.1 ka. In the last 11 ka the RP has produced about one hundred subaerial fissure eruptions, which collectively cover about 600 km<sup>2</sup> and a total volume of 9.8 km<sup>3</sup> (Sinton et al., 2005; Jónsson, 1978).

## 2. 2021 Fagradalsfjall eruption

After a repose period of 781 years, eruptive activity resumed to the Reykjanes Peninsula (SW Iceland) on March 19, 2021 with a basaltic eruption at Geldingadalir within the Fagradalsfjall hyaloclastite complex (Fig. 1) possibly heralding the start of a new period of eruptive activity lasting for several centuries (Bindemann et al., 2022; Halldórsson et al., 2022).

The eruption began on March 19th with opening of several small vents on a 180-m-long, NNE-trending fracture system and subsequently was confined to vents 1a and 1b. It was preceded by intensified seismic unrest in the Fagradalsfjall region beginning February 24, 2021, initially linked to movements on the RP plate boundary as well as emplacement of a 5-7 km-long dyke between Fagradalsfjall and Keilir. Until April 05, 2021 vents 1a and 1b were the only ones active and the venting of the magma was characterized by steady bubble-bursting to weakly fountaining activity accompanied by continuous outflow of lava that supplied the bulk of the lava initially emplaced in Geldingadalir. Between April 05 and 13, five new, initially linear vents opened up along a 1-km-long lineament extending to the north of the initial vents (Fig. 1b), featuring similar eruptive behaviour as typified vents 1a and 1b. All, except vent 5, ceased to be active towards the end of April. From then onward, vent 5 was the locus of activity and has steadily delivered lava to the flow field until September 18, 2021 via internal (sealed) pathways and surface flows, along with a display of episodic venting of magma through lava fountaining of variable intensity and periodicity (Bindemann et al., 2022).

Between March and September, the lava flow field produced a mean lava thickness exceeding 30 m, covered 4.8 km<sup>2</sup> and reached a bulk volume of  $150 \pm 3 \times 10^6$  m<sup>3</sup>. The March–September mean bulk effusion rate was  $9.5 \pm 0.2$  m<sup>3</sup>/s, ranging between 1 and 8 m<sup>3</sup>/s in March–April and increasing to 9–13 m<sup>3</sup>/s in May–September (Pedersen et al., 2022).

## 3. Samples

Samples of fresh lava (March 20-23) and tephra (April 2, April 28 and May 06), quenched during the first weeks of the eruption form the sample set for this study. The samples contain a primitive (i.e., early crystallising) crystal cargo of olivine (Fo<sub>84-89</sub>), plagioclase (An<sub>78-90</sub>), clinopyroxene (Mg#82–88), and Cr spinel (Cr#39–50). Erupted melts (i.e., tephra glass) are of tholeiitic composition and have 7.8–8.7 wt% MgO, 1.0–1.3 wt% TiO<sub>2</sub> and 1.8–2.0 wt% Na<sub>2</sub>O

(Halldórsson et al., 2022; Bindeman et al., 2022). Macrocryst clusters contain direct internal planar boundaries between primitive olivine, clinopyroxene, and plagioclase cores that are not in chemical equilibrium with the external carrier melt. In some instances, high-An plagioclase can be found as inclusions in Mg-rich clinopyroxene (Fig. S2). Low-Fo and -An rims are only present on the *exteriors* of macrocryst clusters, showing that crystal cores co-existed prior to mush mobilisation.

## Supplementary Figures

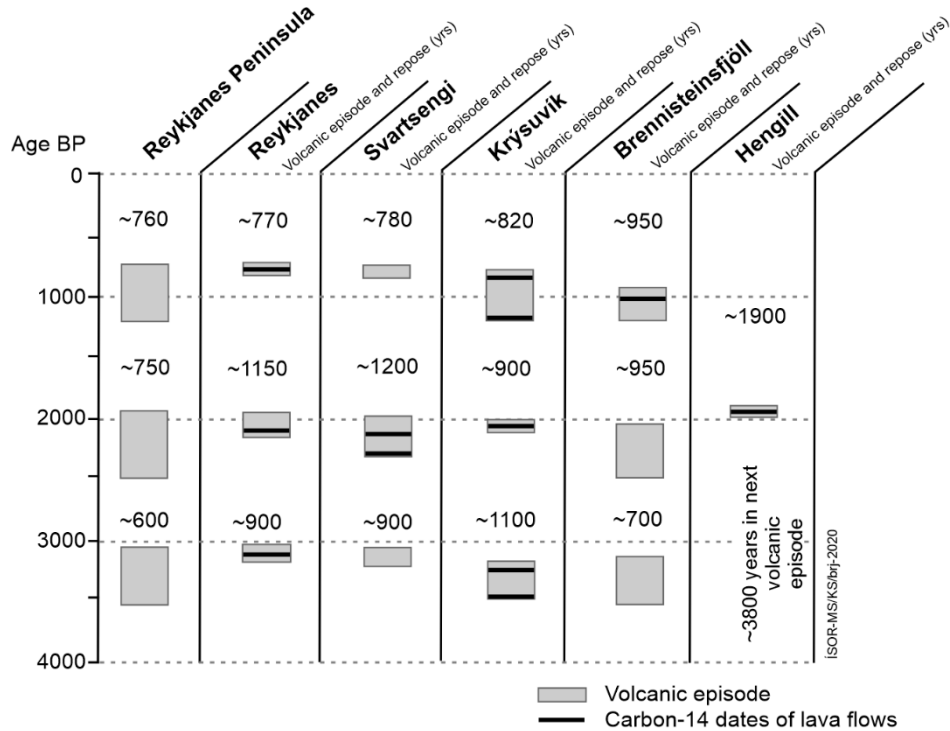


**Fig. S1. Eruption episodes along the Reykjanes Peninsula (RP) within the past 4 ka.** Numbers between grey boxes indicate the repose times between each volcanic episode. Reykjanes, Svartsengi, Krýsuvík and Brennisteinsfjöll refer to the five volcanic systems of the RP. The Hengill volcanic system is included for comparison. Figure from Sæmundsson et al. (2020).

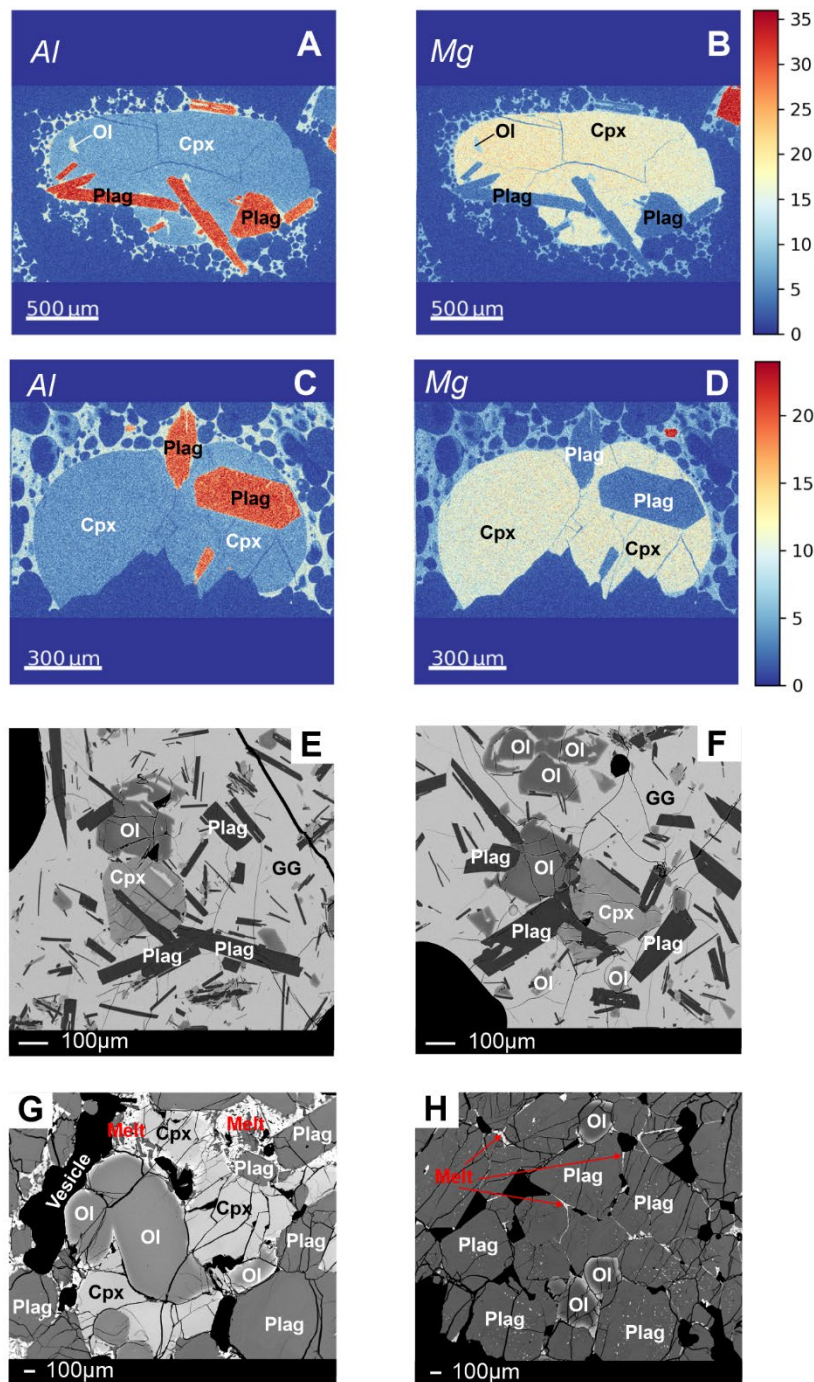


**Fig. S2. Textural characteristics indicating crystal-mush storage.** (A-D) EDS Al (K $\alpha$ ) and Mg (K $\alpha$ ) maps of clinopyroxene oikocrysts containing crystals of olivine and plagioclase. (E-F) BSE images of olivine, clinopyroxene and plagioclase glomerocrysts. (G-H) BSE images of gabbroic (G) and troctolitic (H) xenoliths contained in eruption products collected 24<sup>th</sup> April (G) and 6<sup>th</sup> May (H). Images (G-H) courtesy of W. C. Wenrich, Faculty of Earth Sciences, University of Iceland. Ol: Olivine; Plag: Plagioclase; Cpx: Clinopyroxene; GG: Groundmass glass.

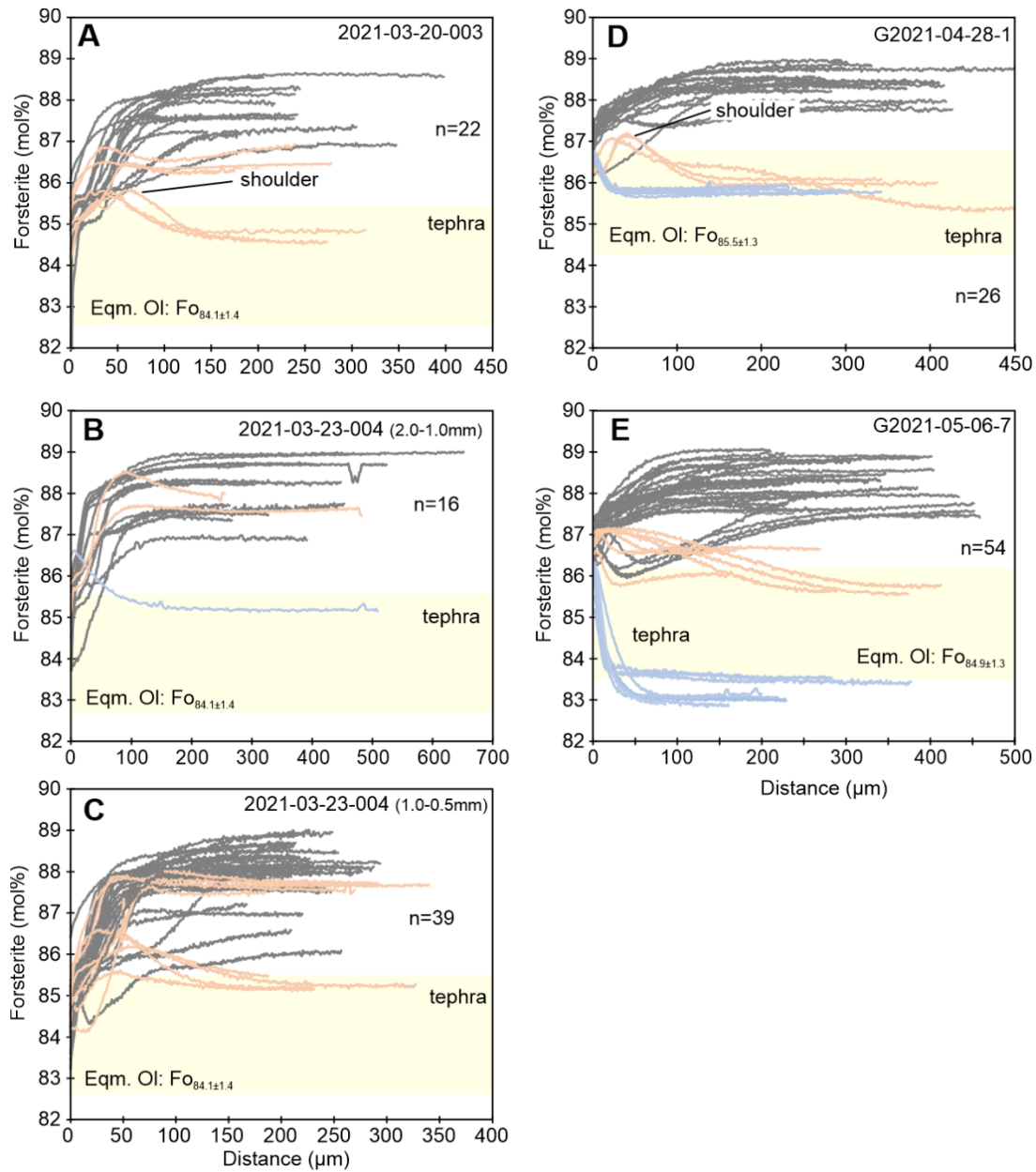


**Fig. S3. Olivine zoning patterns.** Core-to-rim compositional transects highlighting diverse zonation senses and patterns. (A-C) Zoning types of olivine macrocrysts (n=77) from lava samples erupted on March 20 and 23. (D-E) Zoning types of olivine macrocrysts (n=80) from tephra samples erupted on April 28 and May 06. Grey, orange and blue lines: Rim-to-core forsterite ( $100 \times (\text{Mg}/(\text{Mg}+\text{Fe}^{2+}))$ ) concentration profiles. Grey lines: Olivine macrocrysts (73%) displaying normal zoning (i.e.,  $\text{Fo}_{\text{core}} > \text{Fo}_{\text{rim}}$ ) with extensive core plateaux of variable composition ( $\text{Fo}_{86-89}$ ) that decrease by 1-6 mol% forsterite towards the rims ( $\text{Fo}_{83-86}$  lava samples;  $\text{Fo}_{86-88}$  tephra samples). Orange lines: Olivines (16%) displaying complex zoning patterns (i.e.,  $\text{Fo}_{\text{core}} < \text{Fo}_{\text{shoulder}}$ ,  $\text{Fo}_{\text{shoulder}} > \text{Fo}_{\text{rim}}$ ), with crystal interiors of variable composition ( $\text{Fo}_{85-88}$ ) followed by a high-forsterite reverse shoulder zone ( $\text{Fo}_{86-89}$ ), and 16-60  $\mu\text{m}$  of normal zoning at the rim ( $\text{Fo}_{84-86}$  lava samples;  $\text{Fo}_{86.5-87}$  tephra samples). Blue lines: Olivines (11%) showing simple reverse zoning patterns (i.e.  $\text{Fo}_{\text{core}} < \text{Fo}_{\text{rim}}$ ) with extensive core plateaux of

variable composition (Fo<sub>83-86</sub>) that increase by 1-3 mol% forsterite towards the rims (Fo<sub>85-87</sub>). Despite diverse zoning patterns and core compositional records, the olivine rims record relatively uniform rim compositions within the range Fo<sub>83-86</sub> for lava and Fo<sub>85-88</sub> for tephra samples. Yellow areas marked 'tephra' indicate olivine compositions calculated to be in equilibrium with tephra glass compositions erupted on March 24<sup>th</sup>, April 28<sup>th</sup> and May 06<sup>th</sup>. All mineral-melt equilibrium data are provided in table S8.

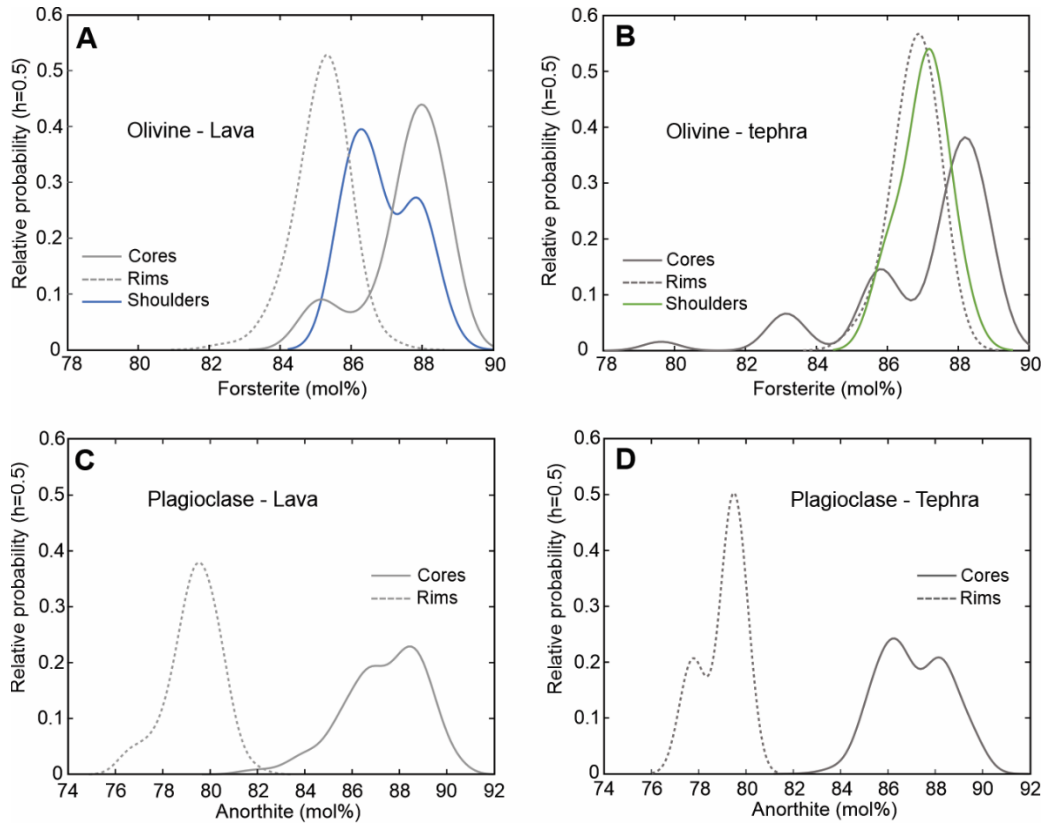


**Fig. S4. Olivine and plagioclase macrocryst compositions.** (A and B) Kernel density estimates (KDEs) depicting forsterite content distributions of olivine cores, shoulders and rims from lava and tephra samples. (C and D) KDEs illustrate anorthite distribution of plagioclase cores and rims from lava and tephra samples. Shoulders refer to high-forsterite shoulder zones of complexly zoned olivines (see Fig. S3). Forsterite [mol%] =  $100 \times (\text{Mg}/(\text{Mg}+\text{Fe}^{2+}))$ ; Anorthite [mol%] =  $100 \times (\text{Ca}/(\text{Ca}+\text{Na}+\text{K}))$ .

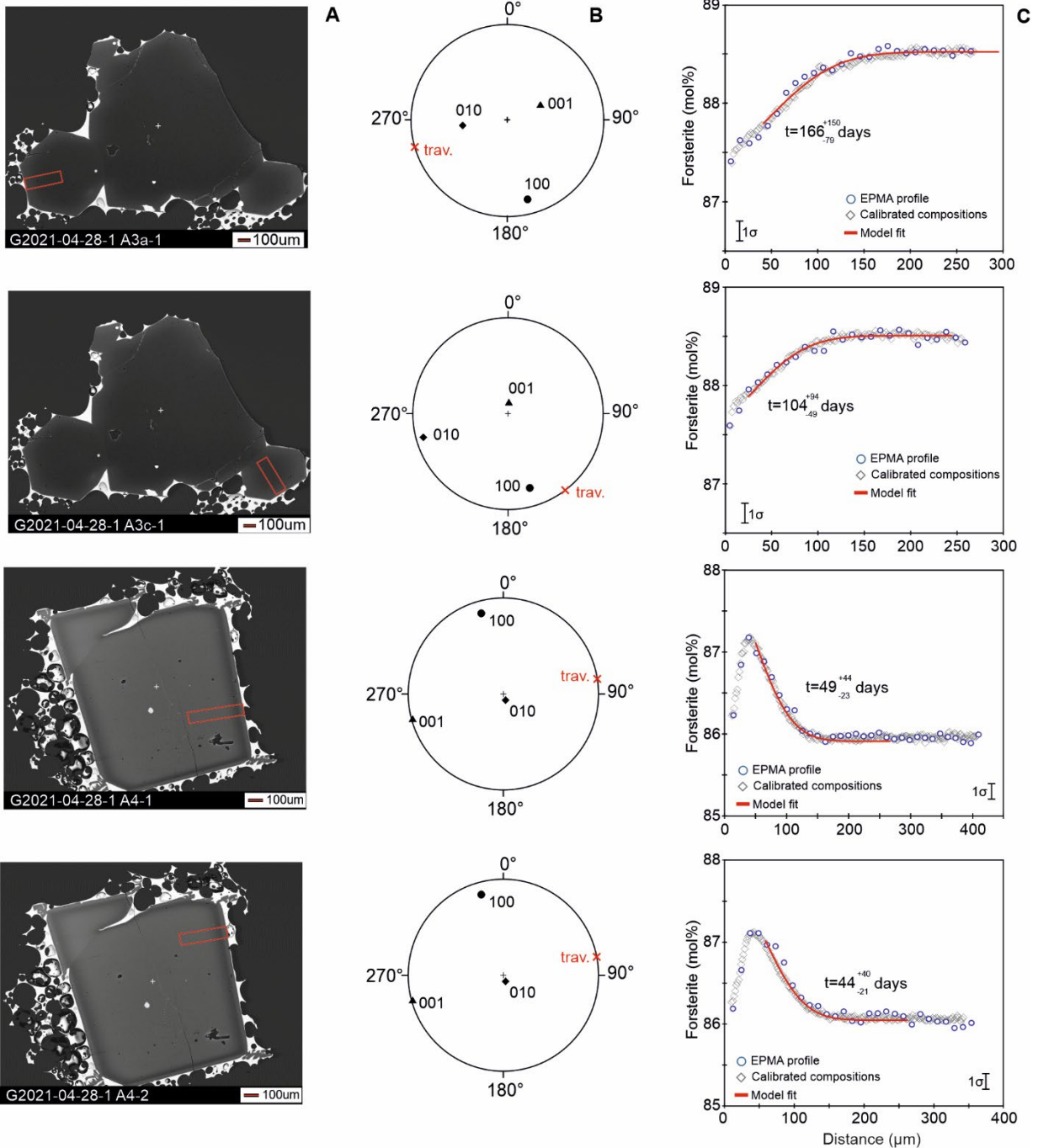


**Fig. S5. Data, initial conditions and best fit olivine diffusion models – April 28, 2021.** (A) Backscattered electron (BSE) images of the analyzed olivine crystals. Red boxes: Directions of EMP traverses. (B) Stereographic lower hemisphere plots depicting the angular relations between the main crystallographic axes in olivine and the directions of the analytical traverses (red x marked 'trav.'). (C) Rim to core concentration profiles of forsterite content. Red and blue curves, best-fit diffusion models for the observed zoning profiles. Numbers in days indicate

diffusive timescales obtained from best-fit model solutions.  $1\sigma$  error bars refer to electron microprobe data.

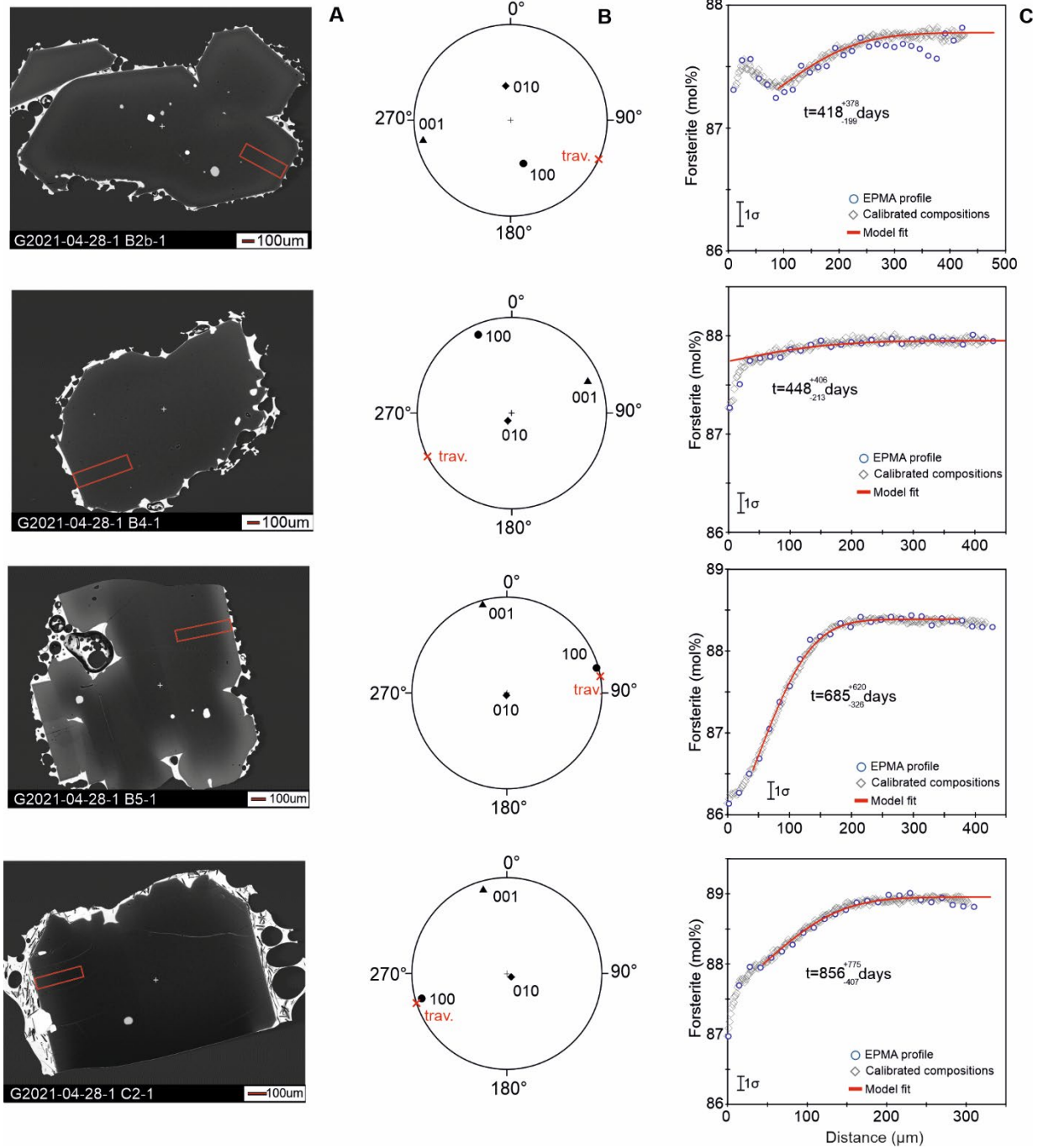


**Fig. S6. Data, initial conditions and best fit olivine diffusion models – April 28, 2021.**  
Caption the same as Supplemental Figure S5.

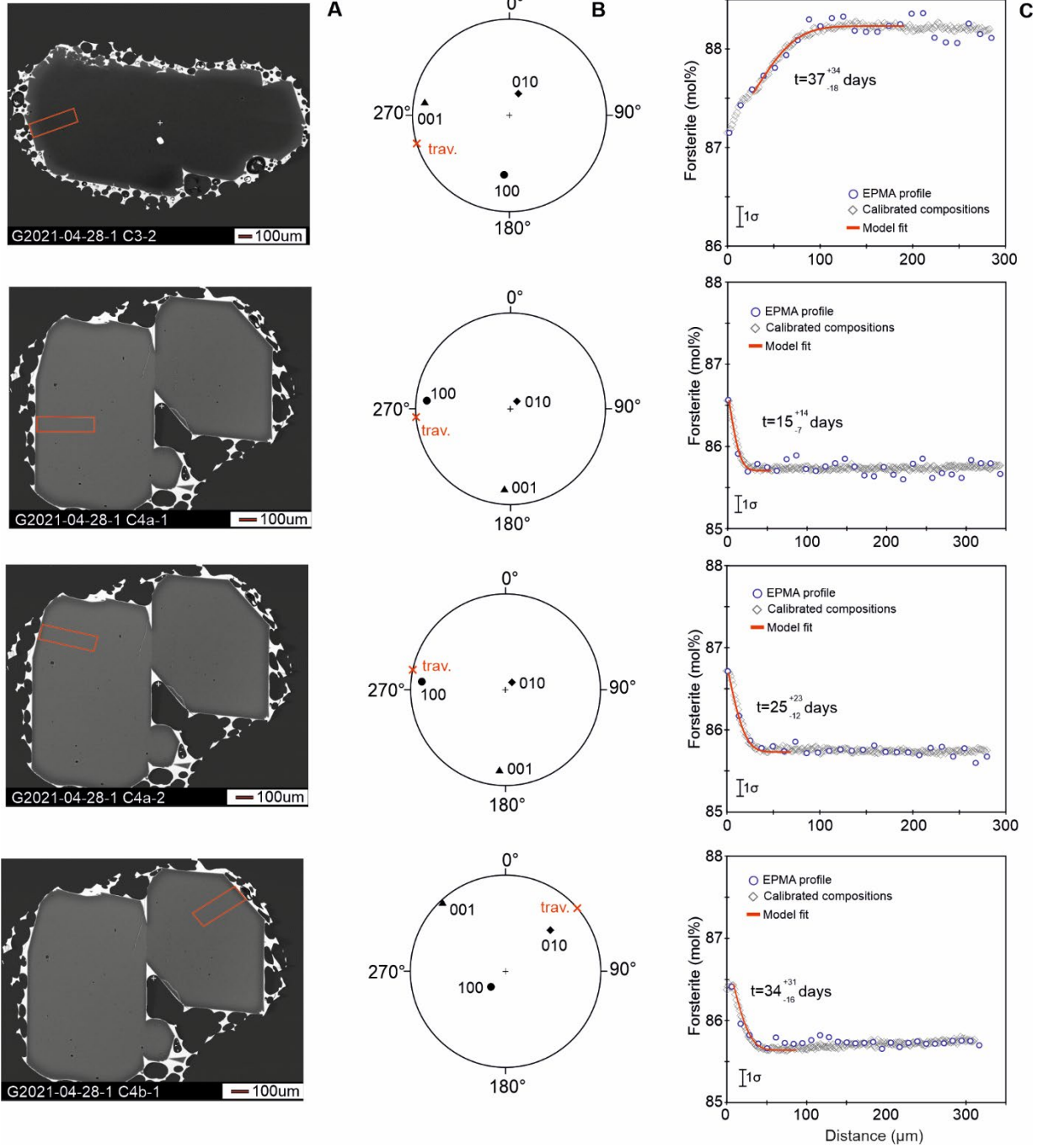


**Fig. S7. Data, initial conditions and best fit olivine diffusion models – April 28, 2021.**  
Caption the same as Supplemental Figure S5.

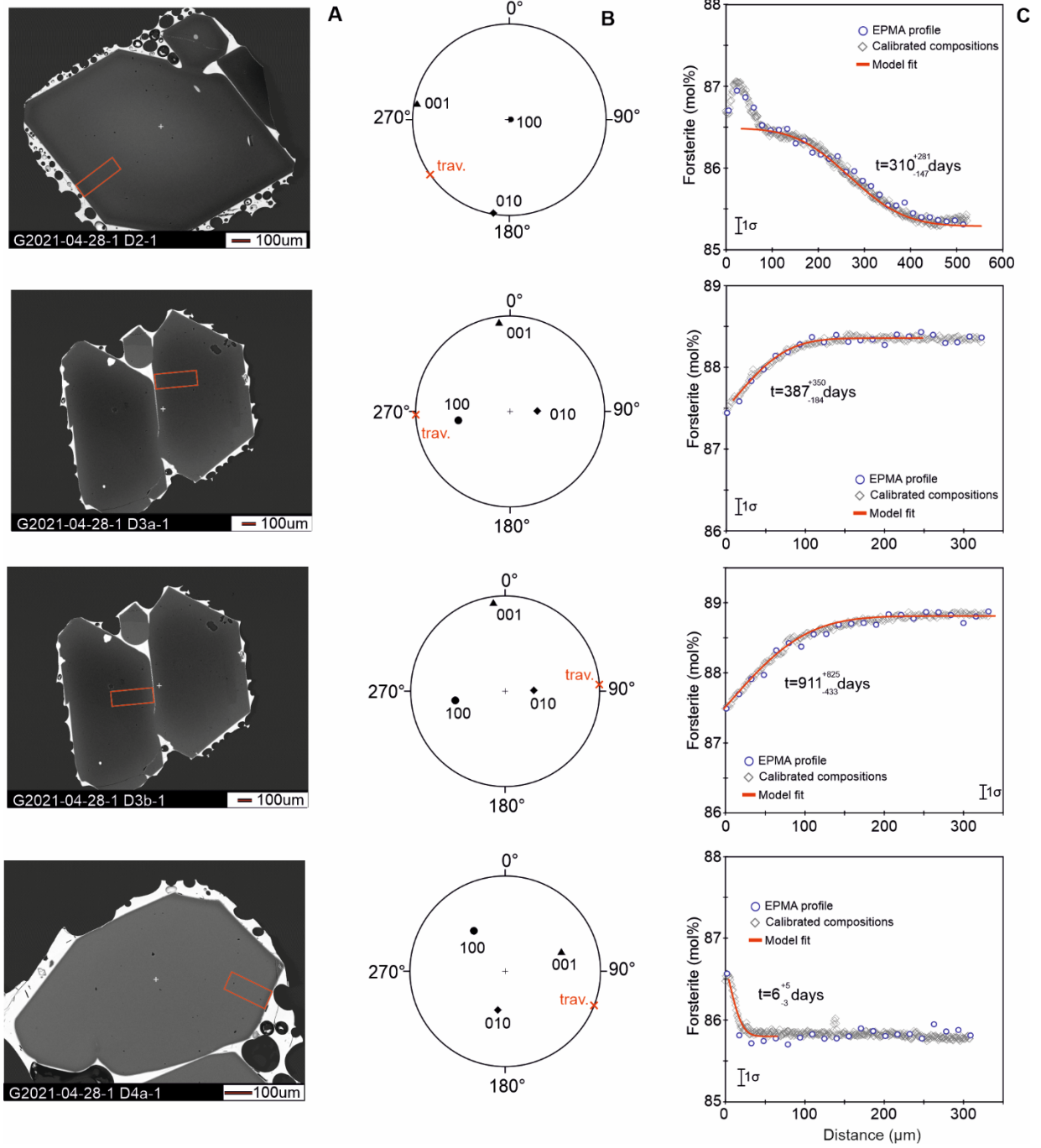


**Fig. S8. Data, initial conditions and best fit olivine diffusion models – April 28, 2021.**  
Caption the same as Supplemental Figure S5.

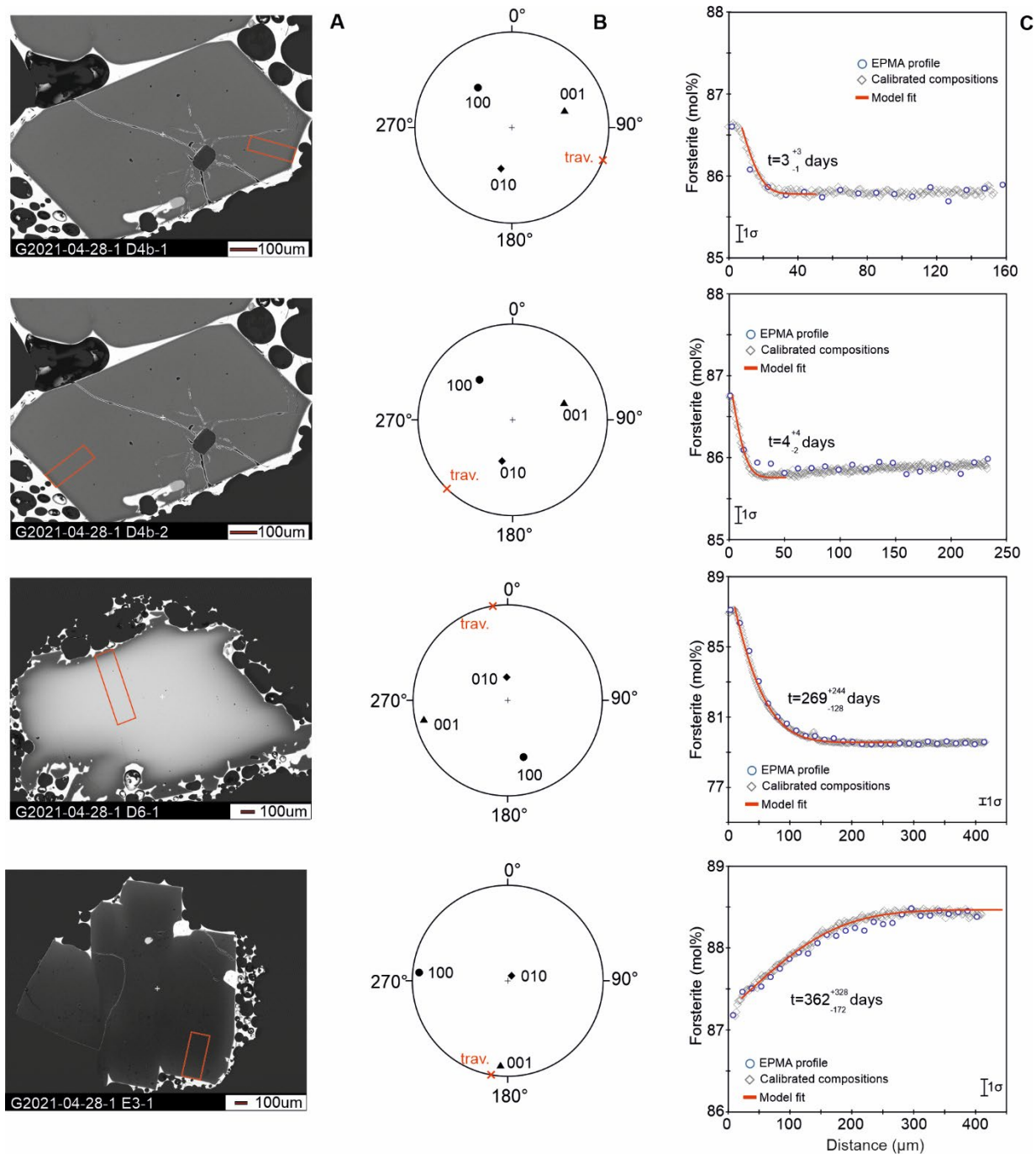


**Fig. S9. Data, initial conditions and best fit olivine diffusion models – April 28, 2021.**  
Caption the same as Supplemental Figure S5.

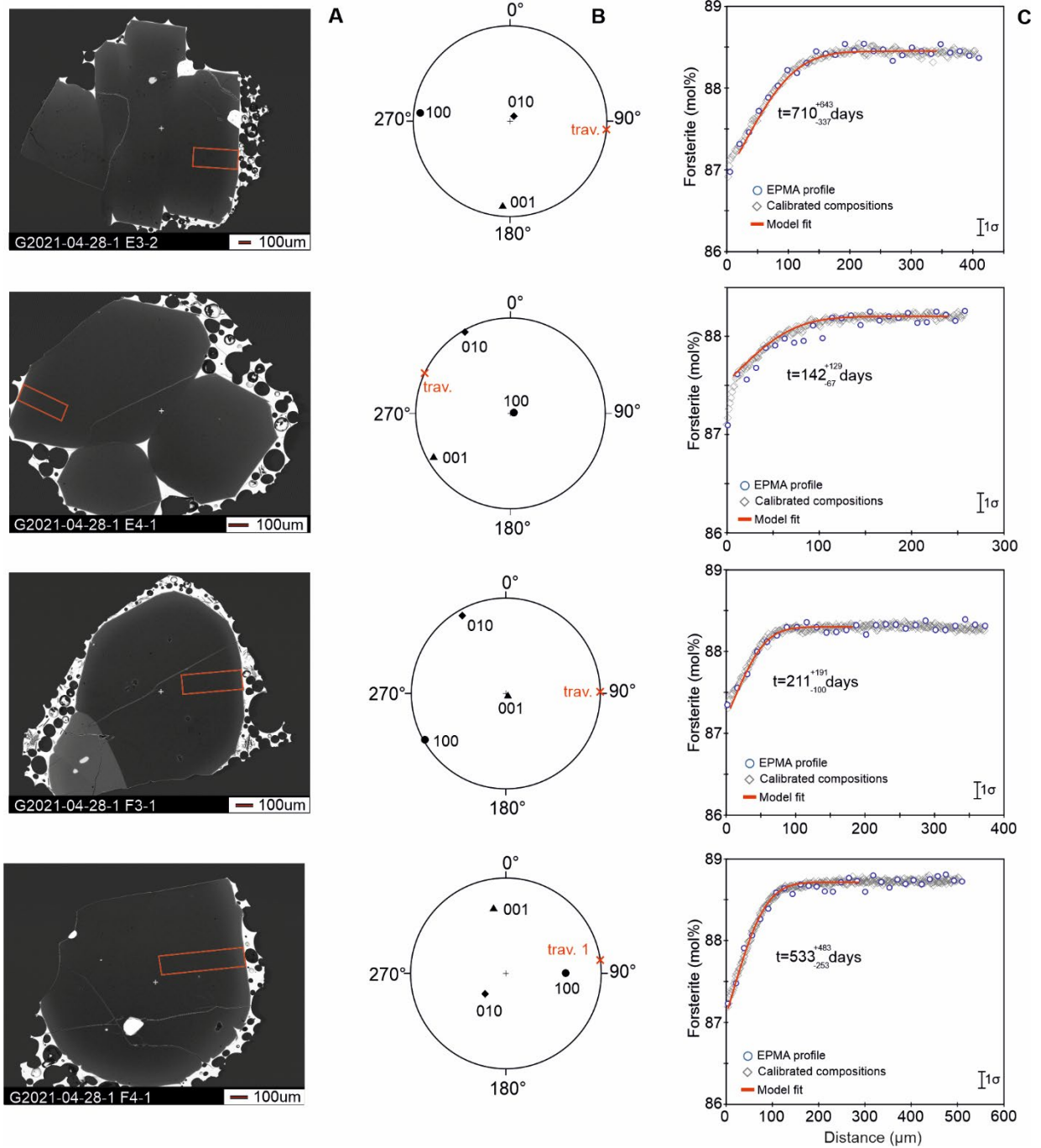


**Fig. S10. Data, initial conditions and best fit olivine diffusion models – April 28, 2021.**  
Caption the same as Supplemental Figure S5.

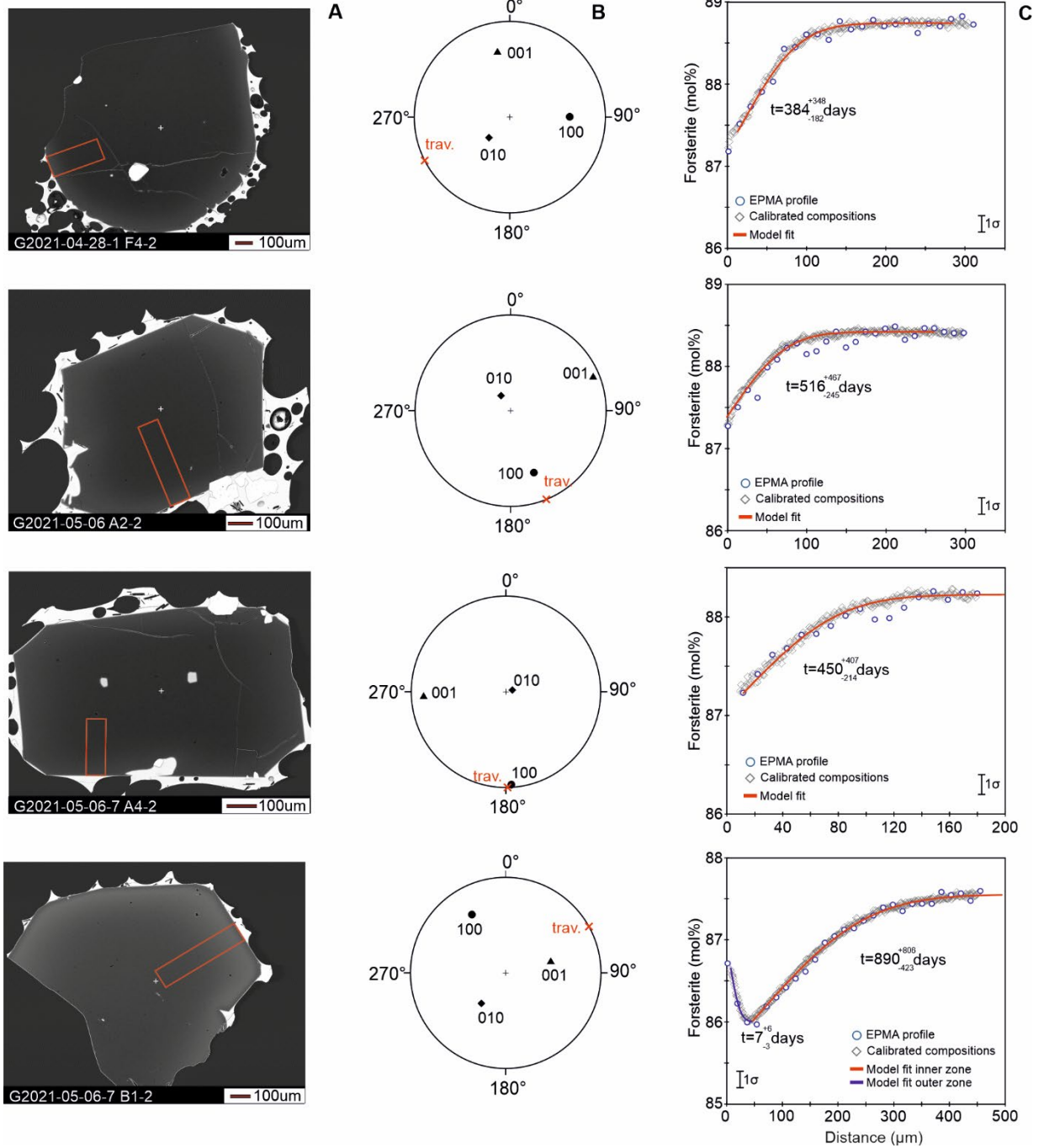


**Fig. S11. Data, initial conditions and best fit olivine diffusion models – May 06, 2021.**  
Caption the same as Supplemental Figure S5.

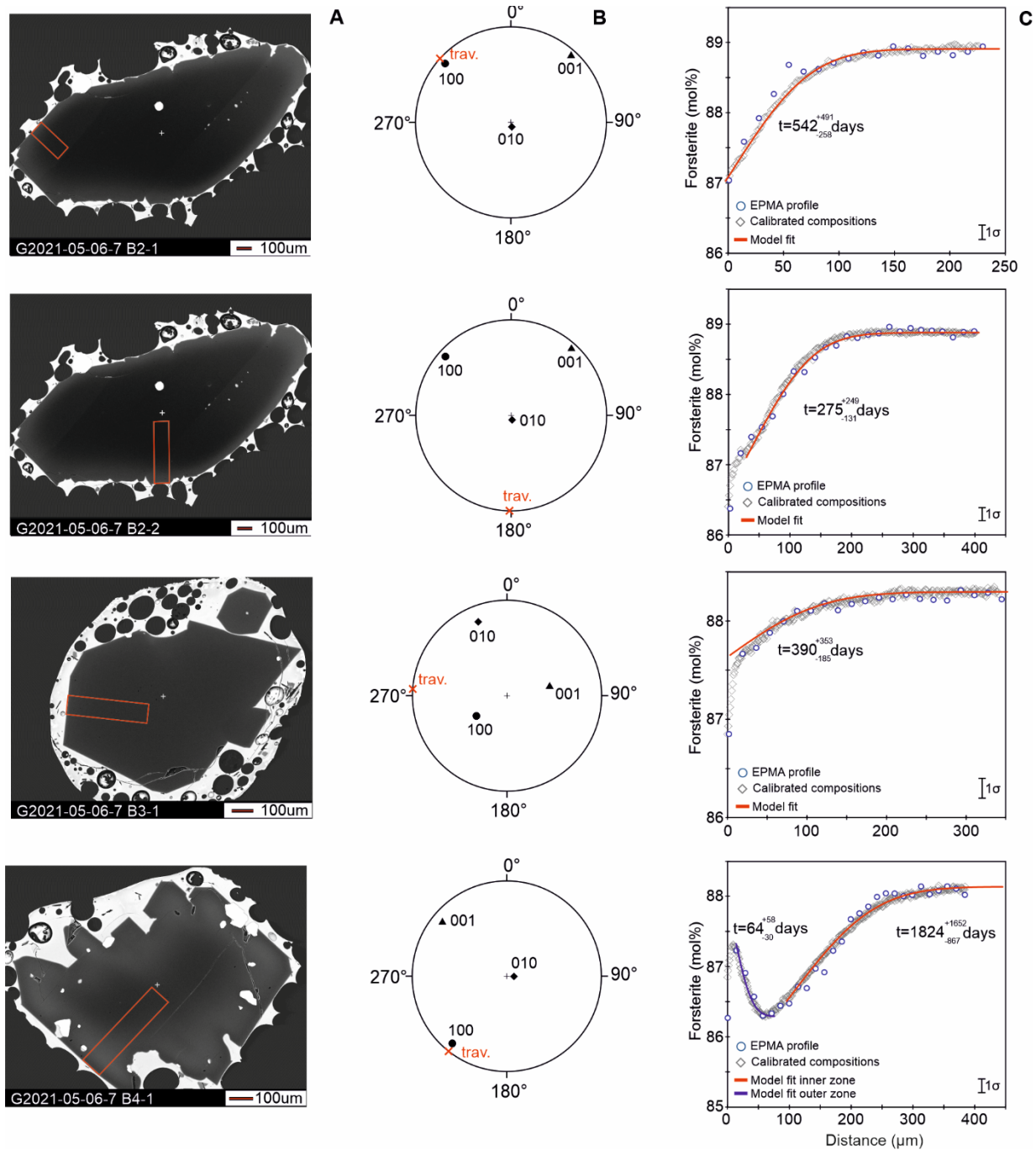


**Fig. S12. Data, initial conditions and best fit olivine diffusion models – May 06, 2021.**  
Caption the same as Supplemental Figure S5.

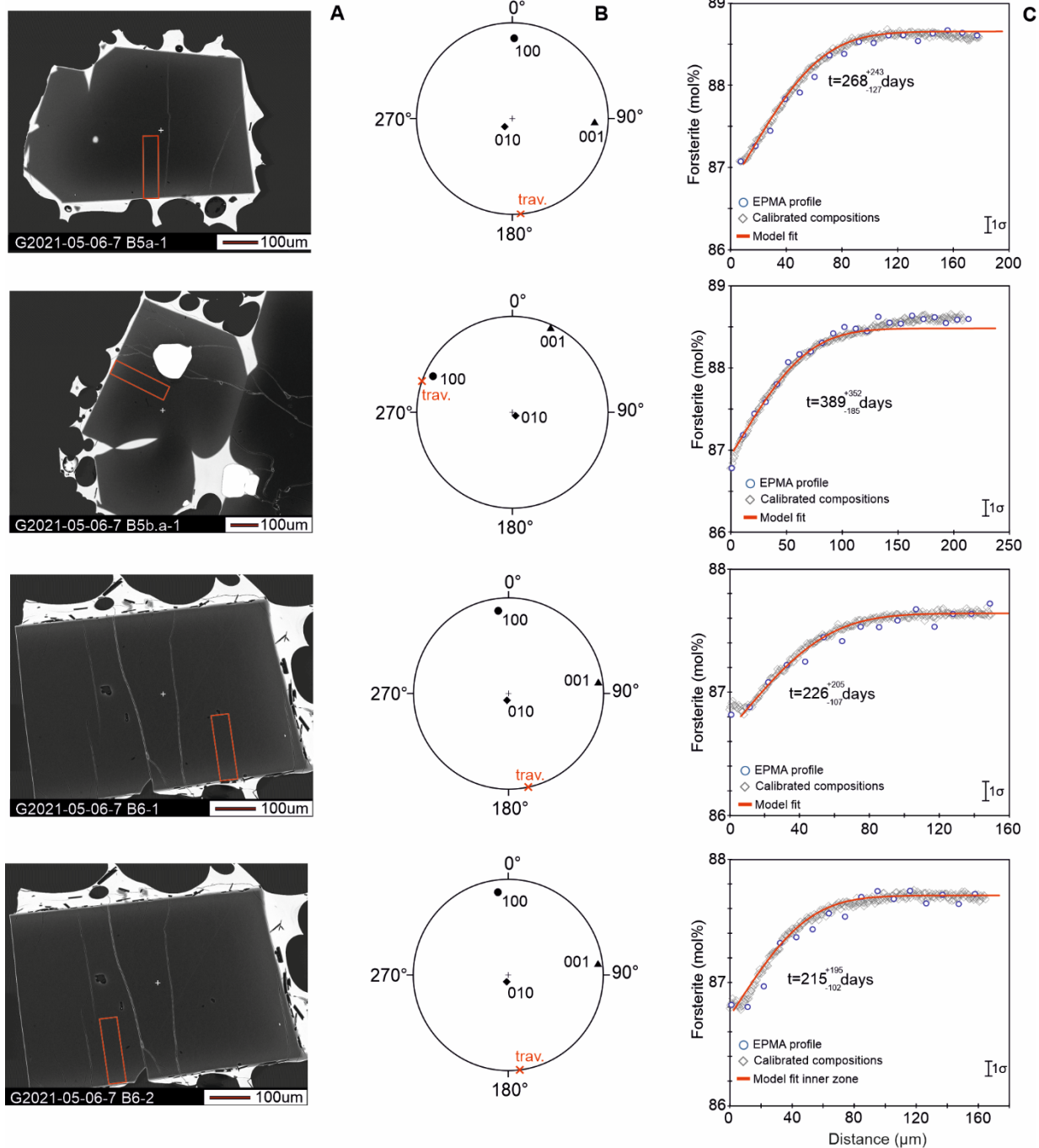


**Fig. S13. Data, initial conditions and best fit olivine diffusion models – May 06, 2021.**  
Caption the same as Supplemental Figure S5.

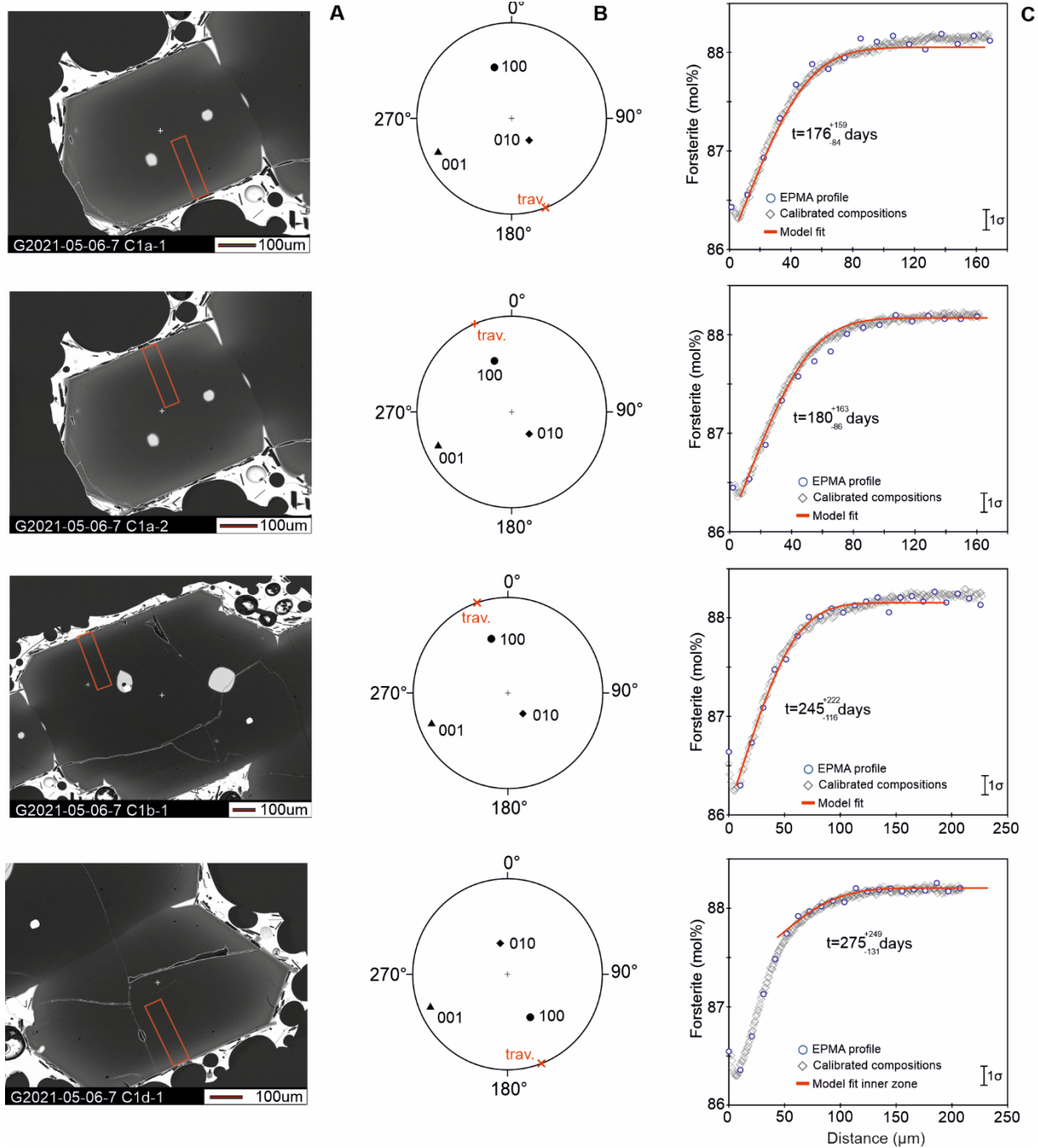


**Fig. S14. Data, initial conditions and best fit olivine diffusion models – May 06, 2021.**  
Caption the same as Supplemental Figure S5.

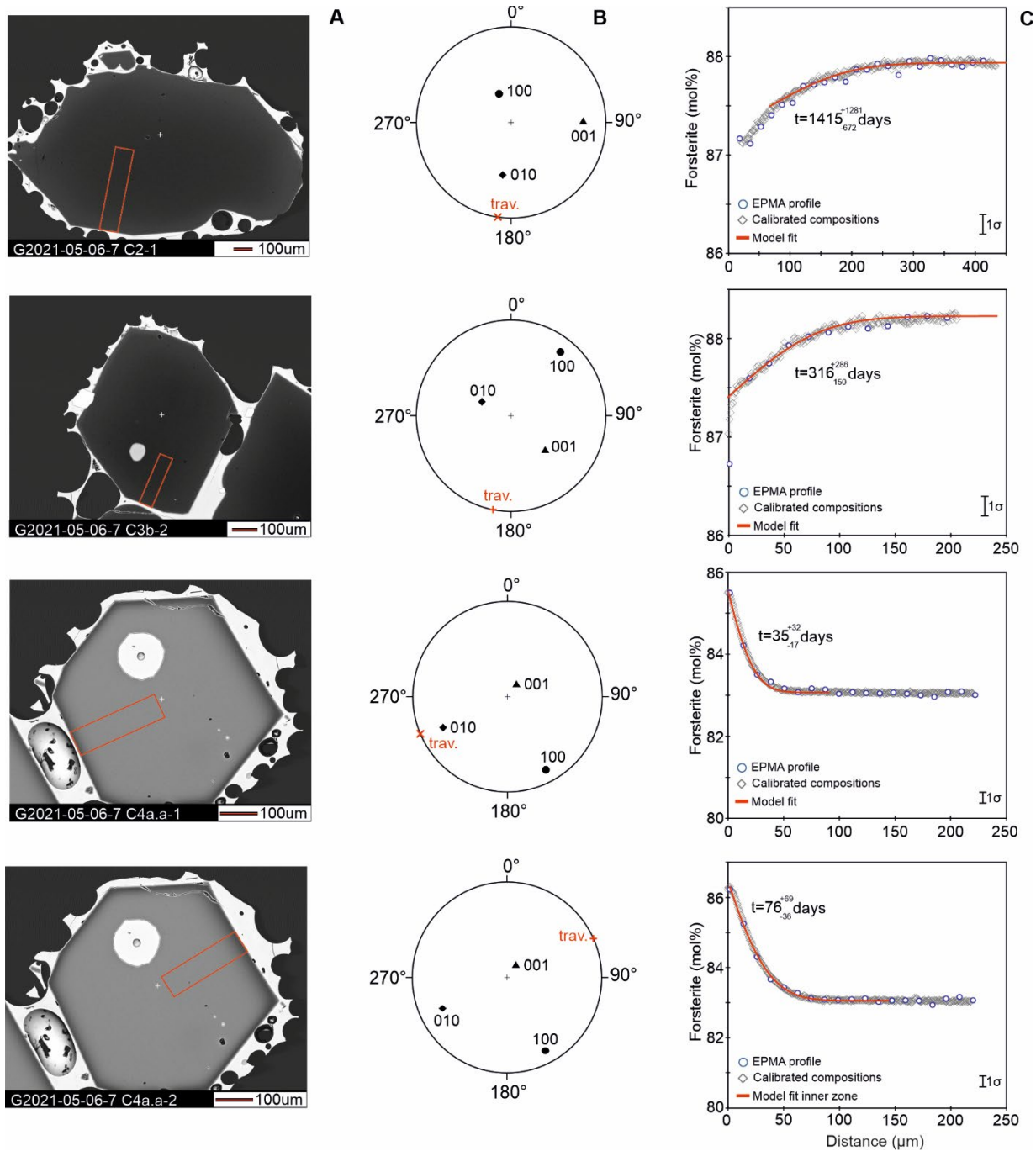


**Fig. S15. Data, initial conditions and best fit olivine diffusion models – May 06, 2021.**  
Caption the same as Supplemental Figure S5.

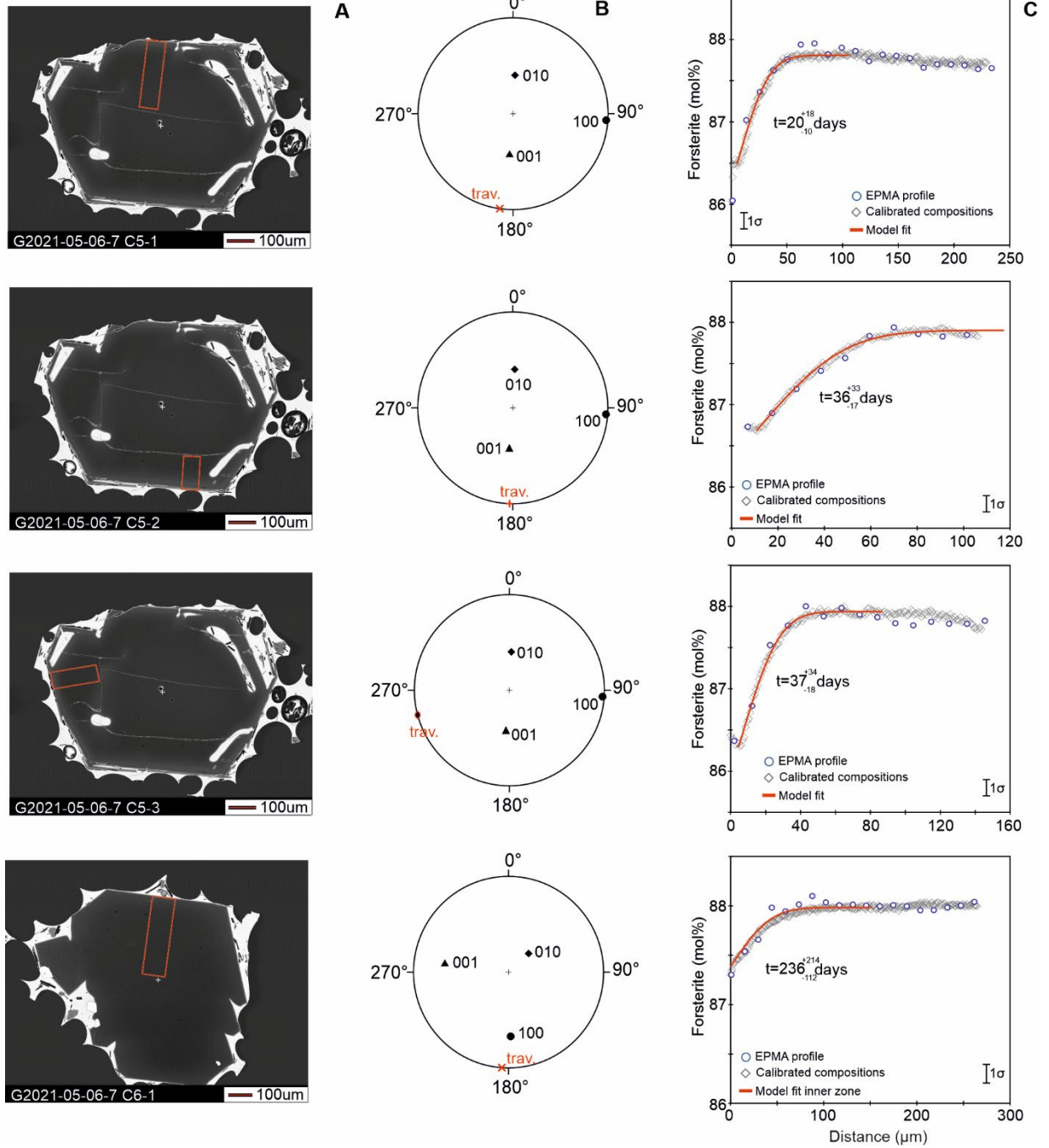


**Fig. S16. Data, initial conditions and best fit olivine diffusion models – May 06, 2021.**  
Caption the same as Supplemental Figure S5.

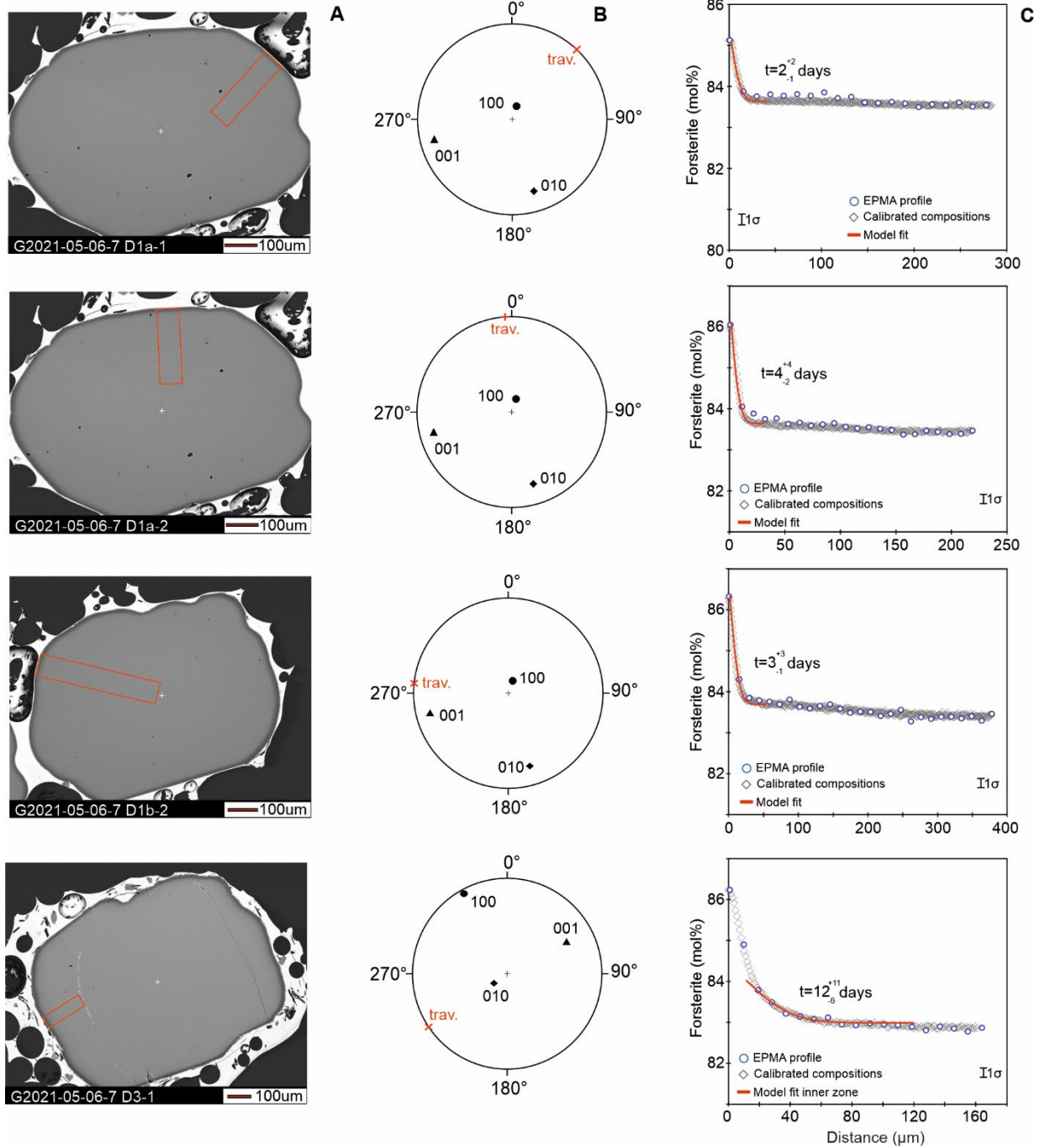


**Fig. S17. Data, initial conditions and best fit olivine diffusion models – May 06, 2021.**  
Caption the same as Supplemental Figure S5.

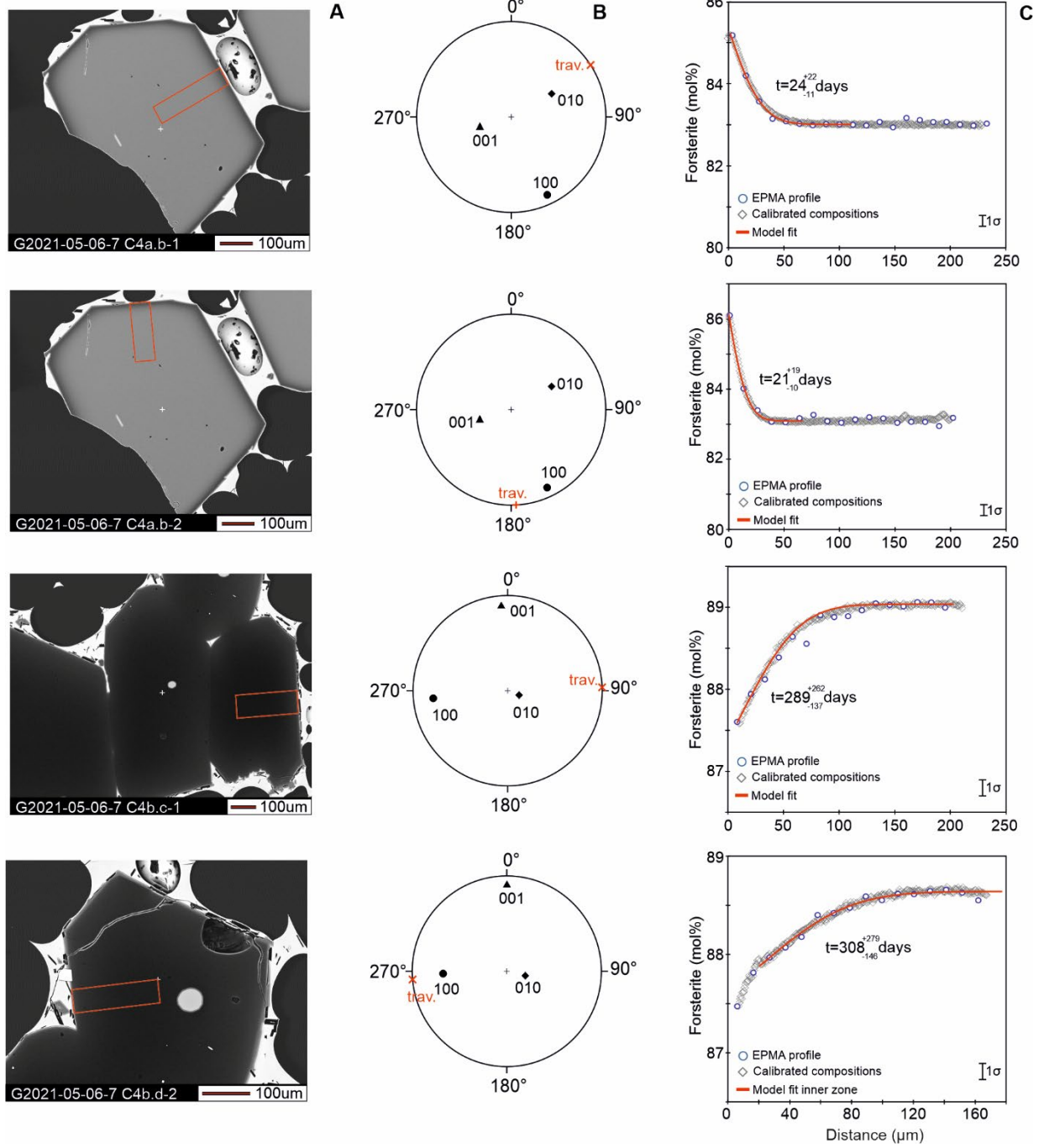


**Fig. S18. Data, initial conditions and best fit olivine diffusion models – May 06, 2021.**  
Caption the same as Supplemental Figure S5.

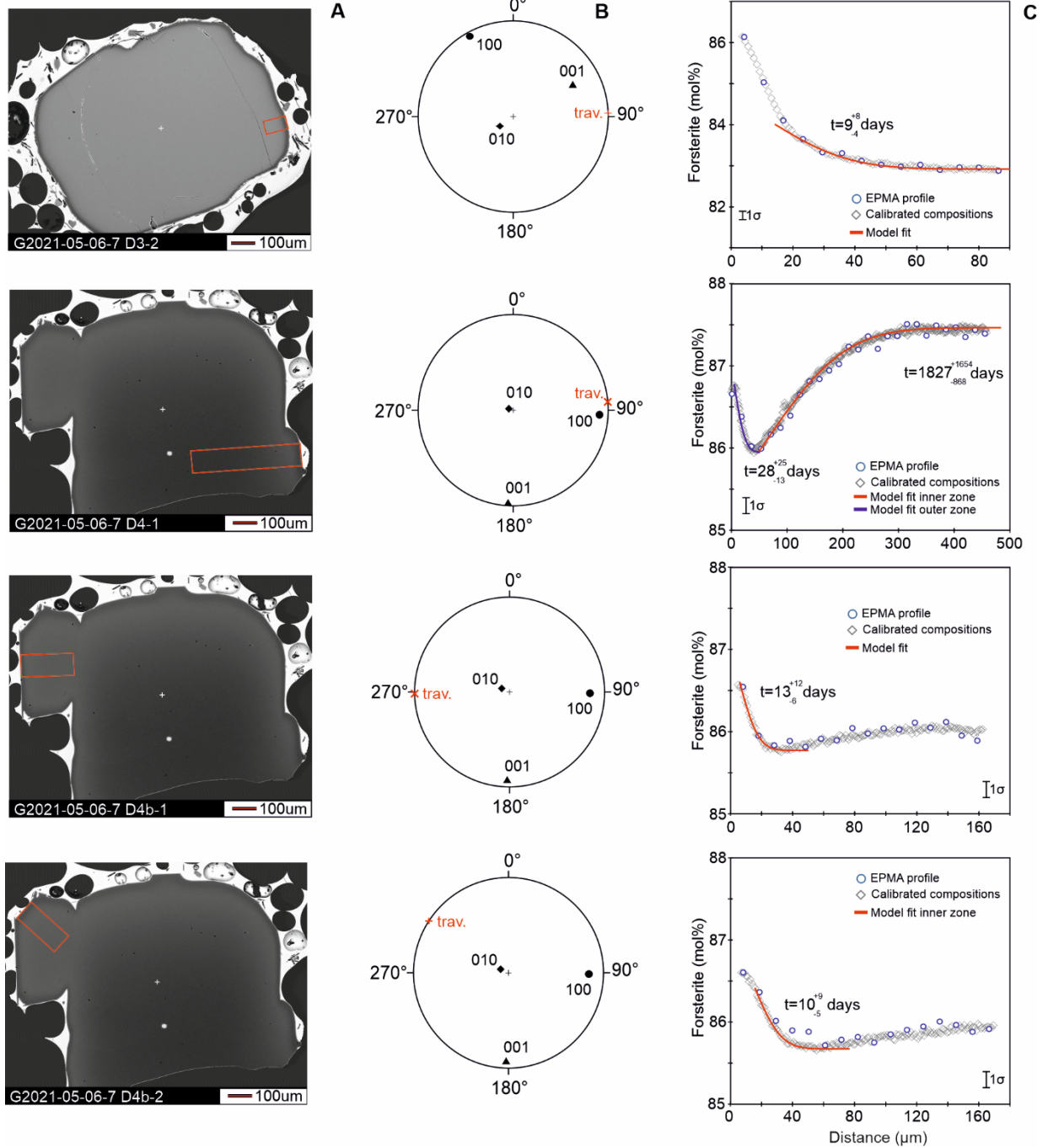


**Fig. S19. Data, initial conditions and best fit olivine diffusion models – May 06, 2021.**  
Caption the same as Supplemental Figure S5.

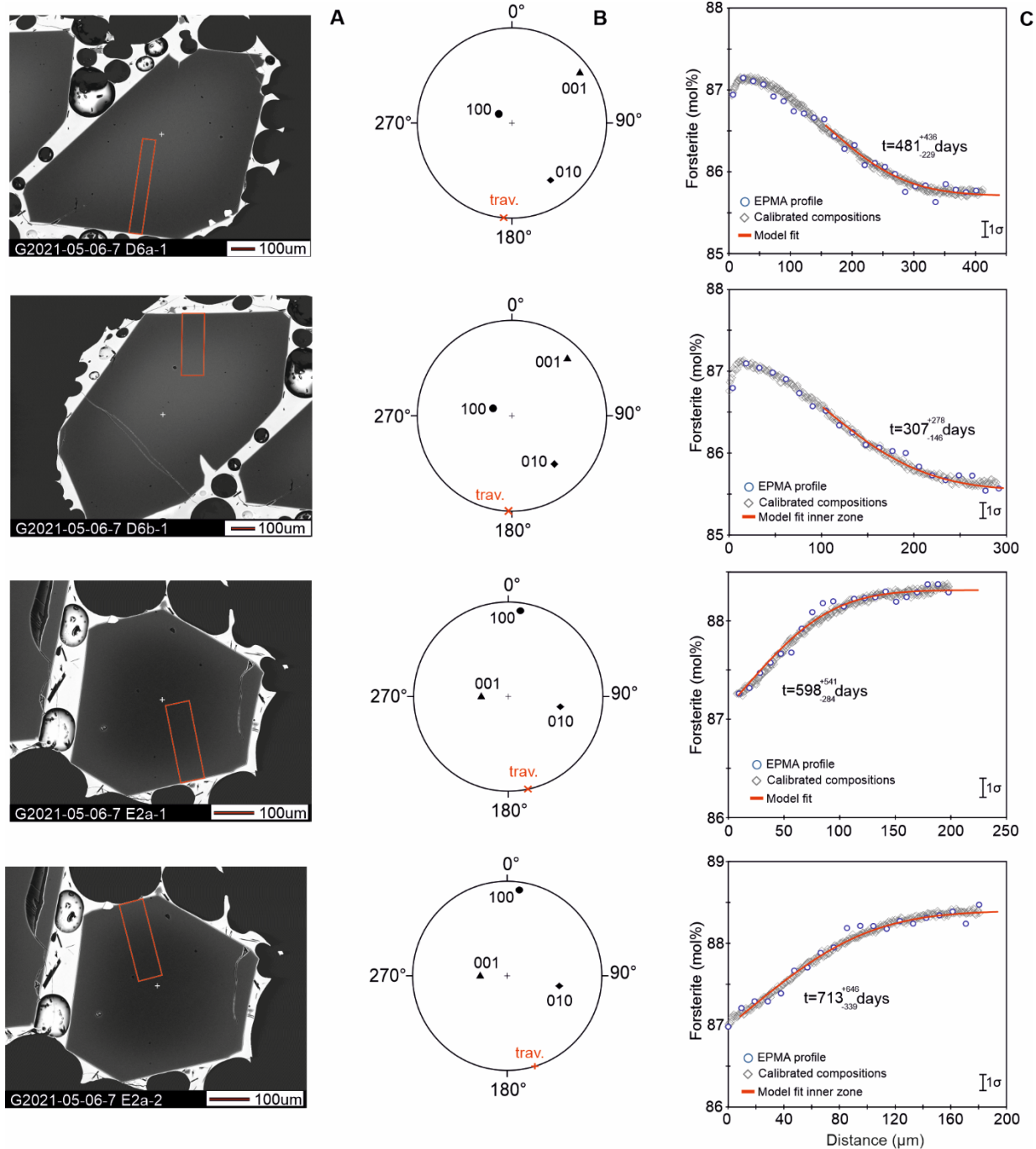


**Fig. S20. Data, initial conditions and best fit olivine diffusion models – May 06, 2021.**  
Caption the same as Supplemental Figure S5.

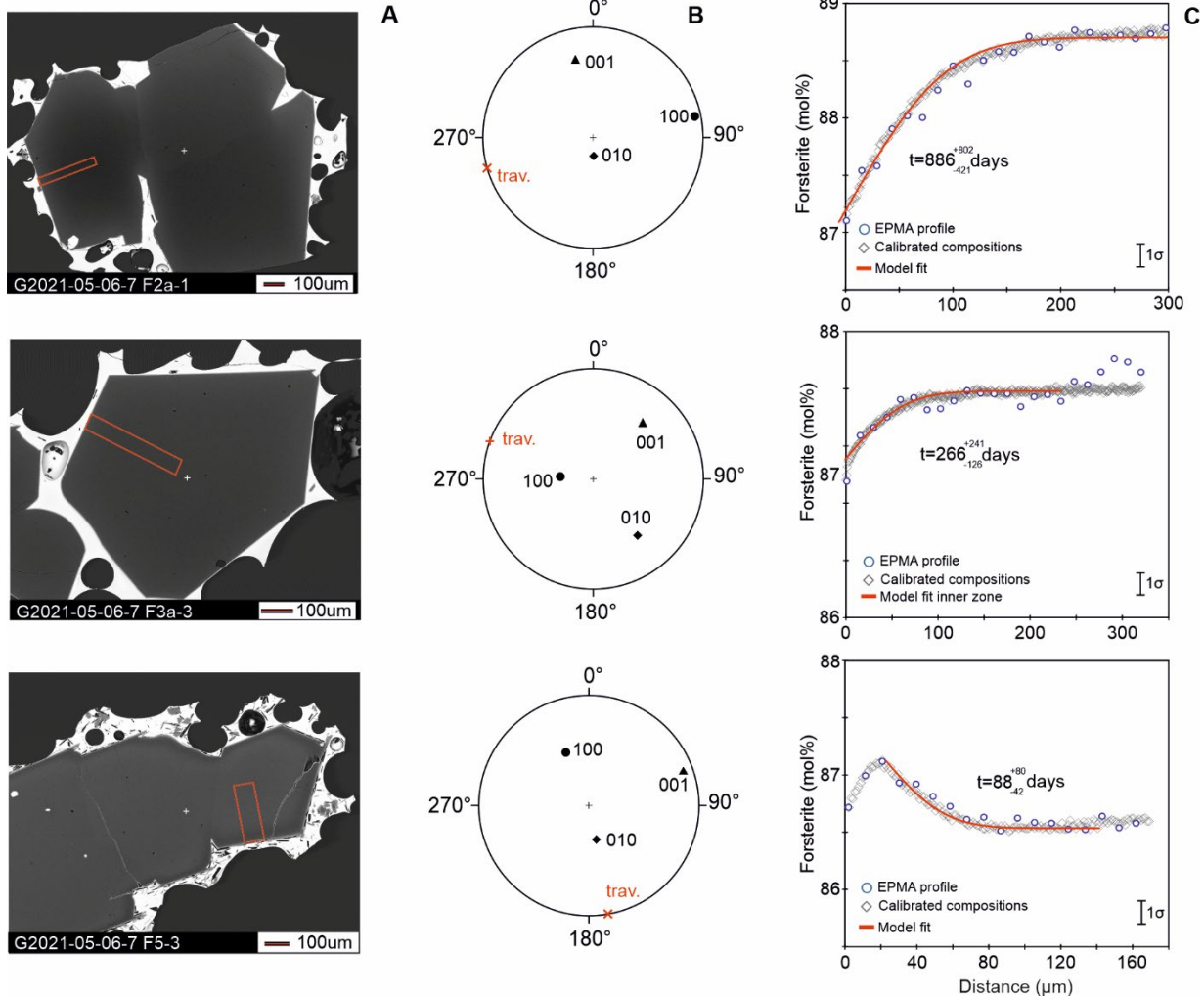


**Fig. S21. Data, initial conditions and best fit olivine diffusion models – May 06, 2021.**  
Caption the same as Supplemental Figure S5.

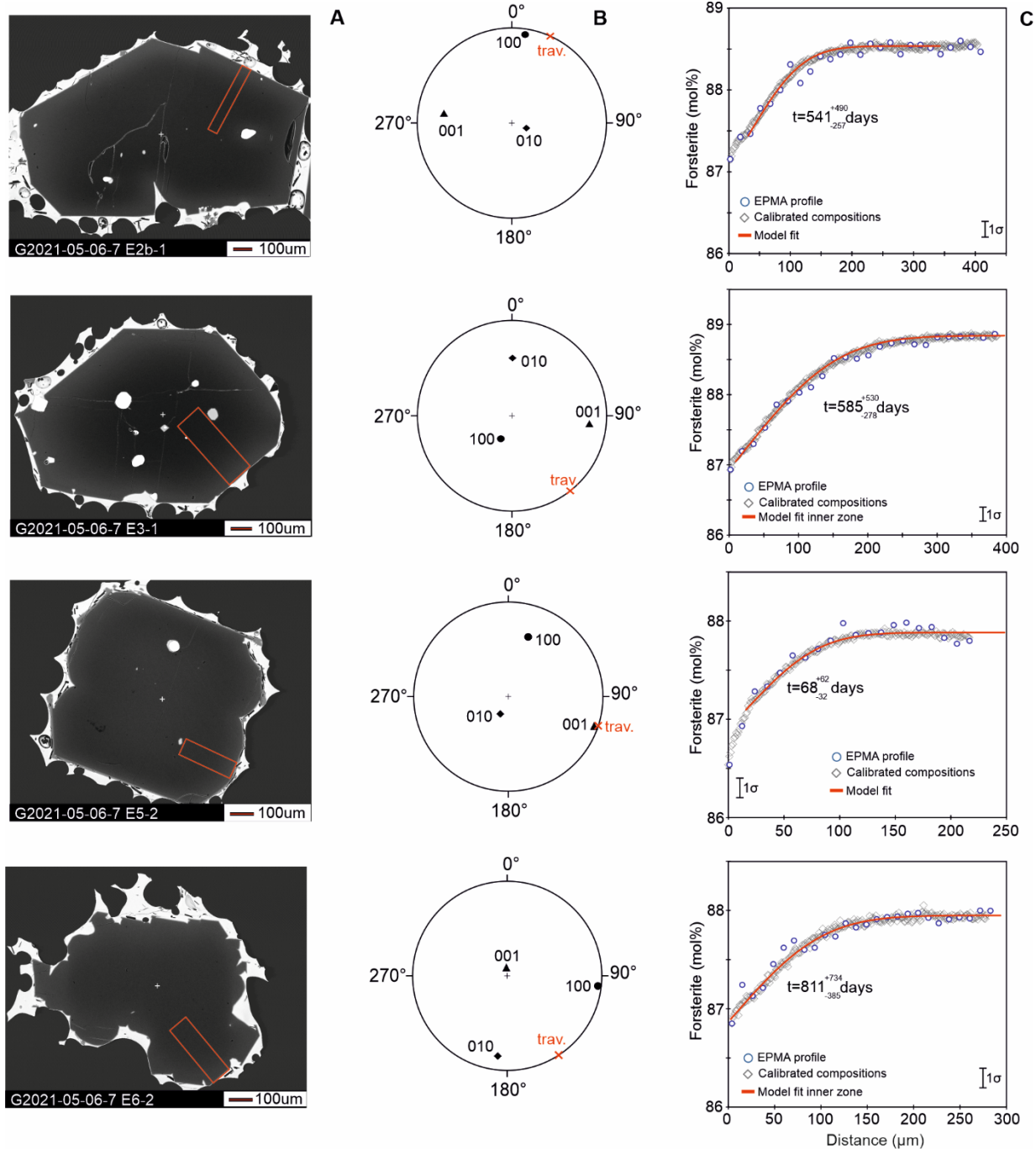


**Fig. S22. Data, initial conditions and best fit olivine diffusion models – May 06, 2021.**  
Caption the same as Supplemental Figure S5.

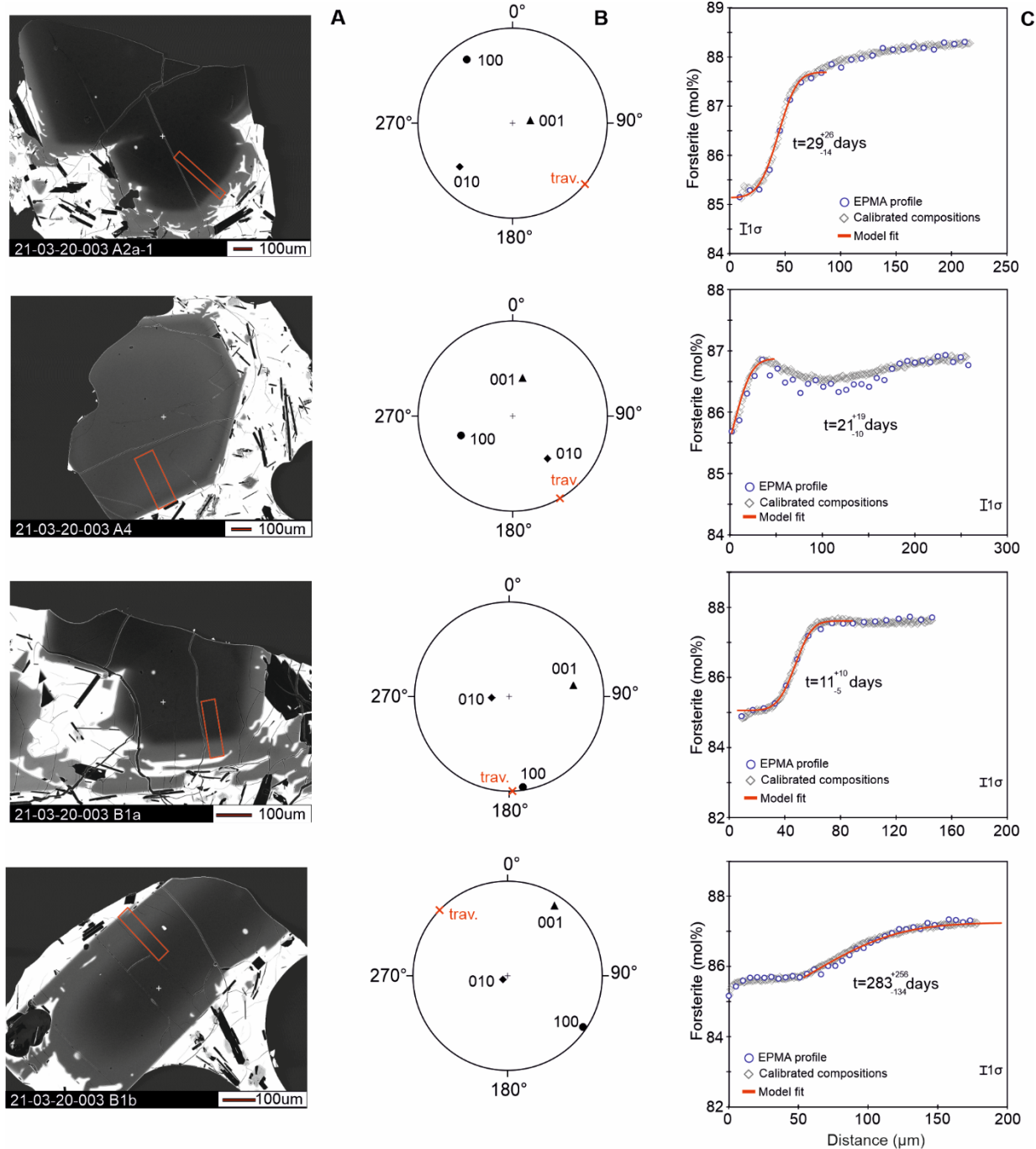


**Fig. S23. Data, initial conditions and best fit olivine diffusion models – March 20, 2021.**  
Caption the same as Supplemental Figure S5.

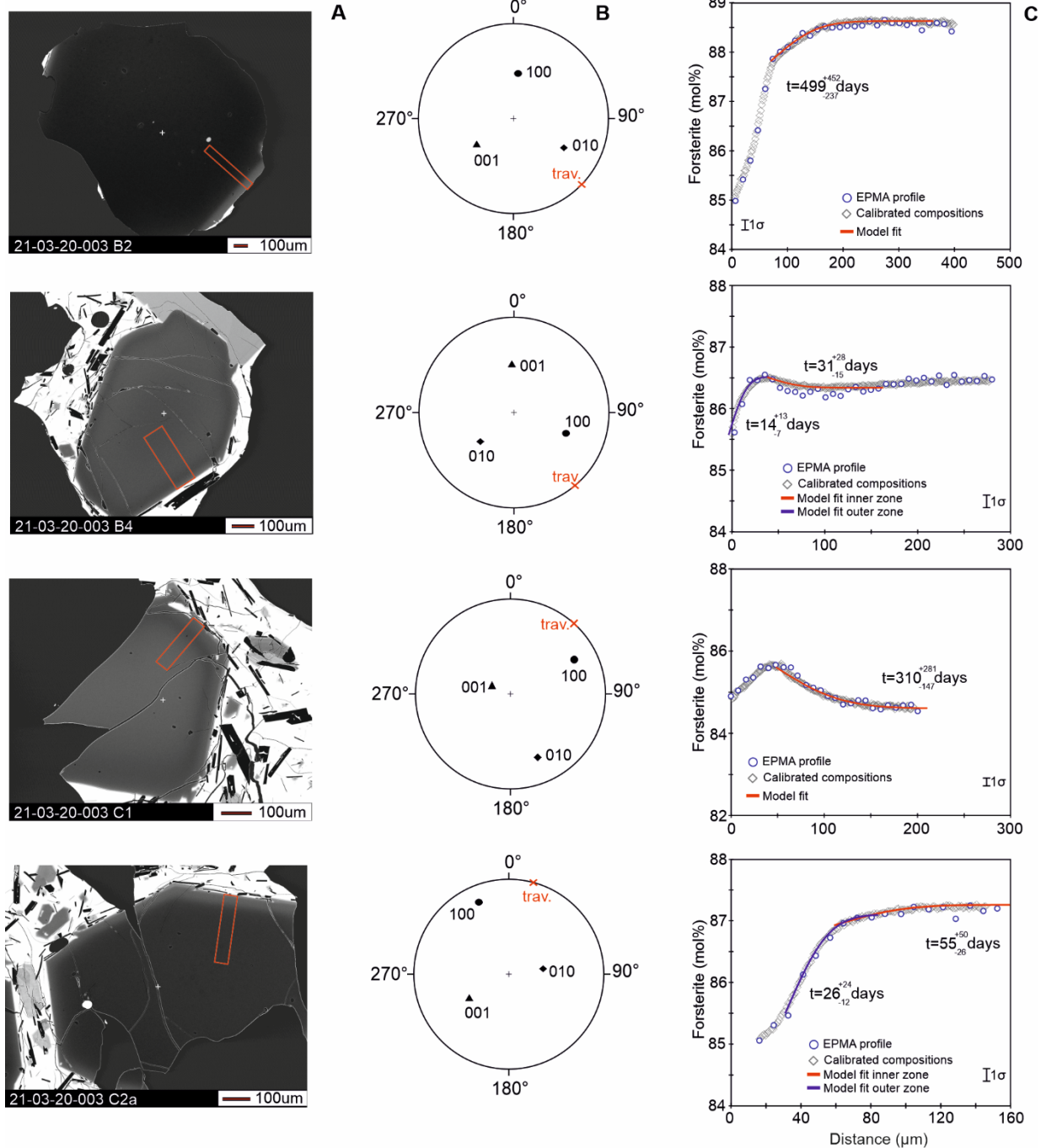


**Fig. S24. Data, initial conditions and best fit olivine diffusion models – March 20, 2021.**  
Caption the same as Supplemental Figure S5.

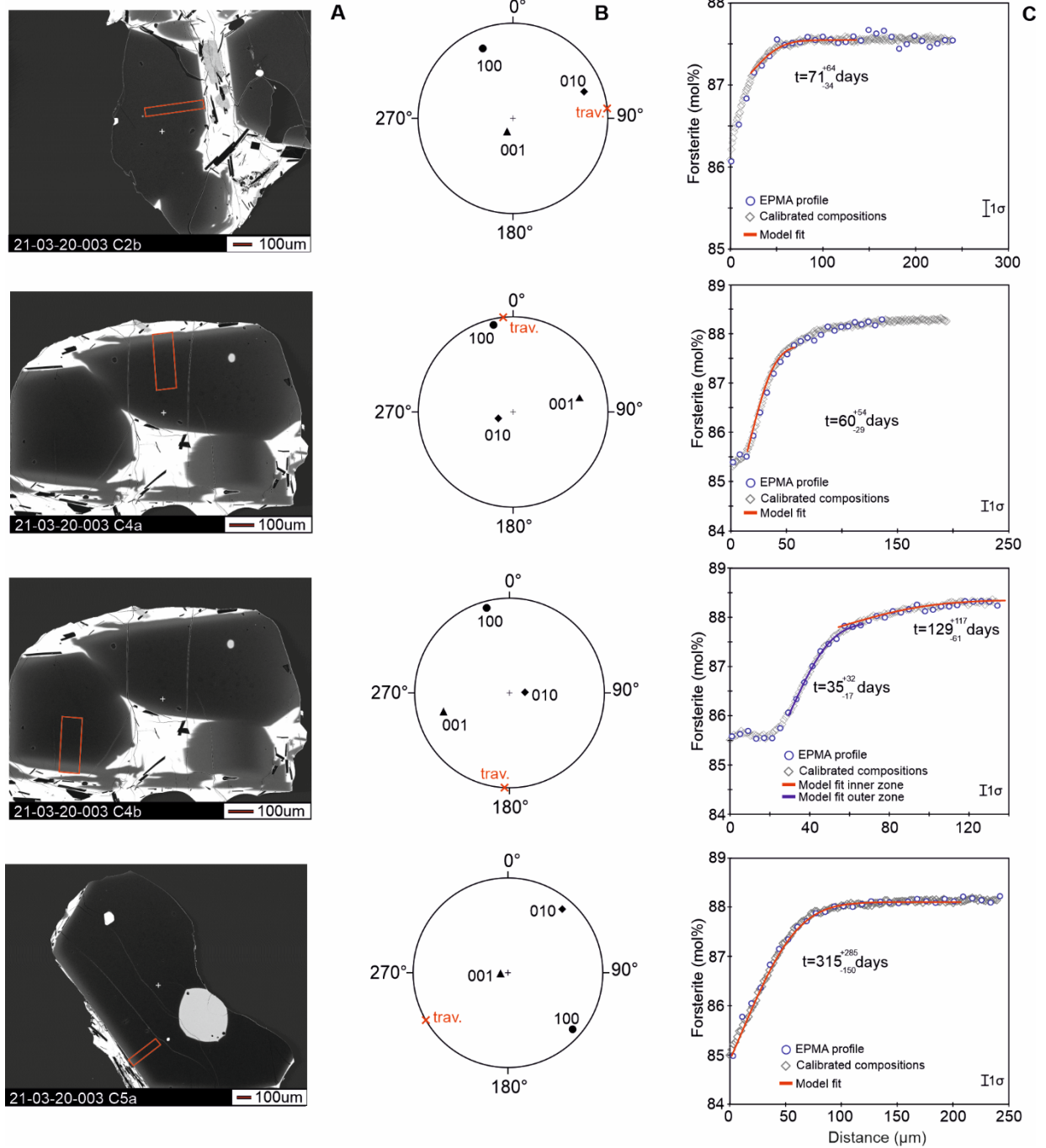


**Fig. S25. Data, initial conditions and best fit olivine diffusion models – March 20, 2021.**  
Caption the same as Supplemental Figure S5.

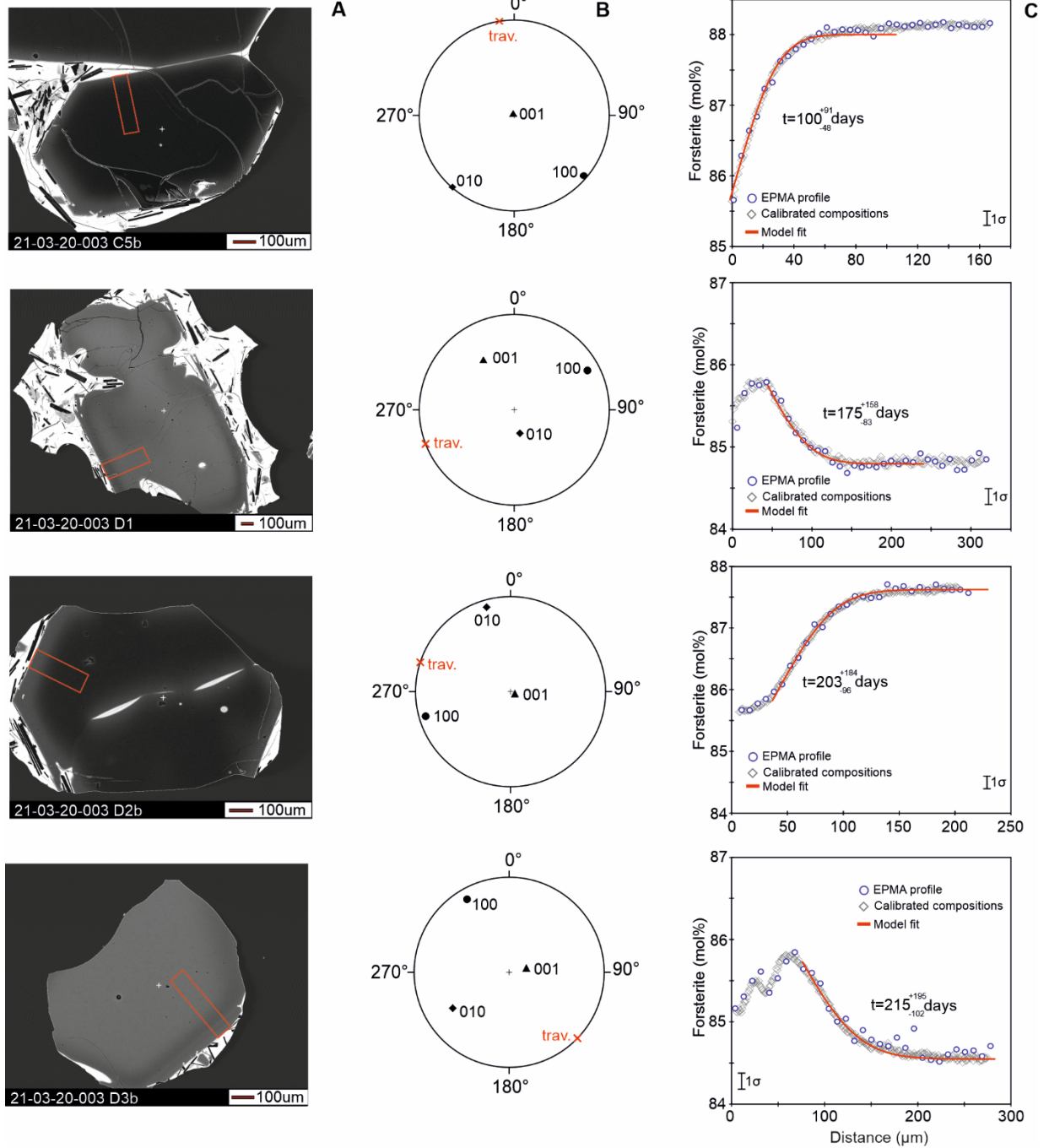


**Fig. S26. Data, initial conditions and best fit olivine diffusion models – March 20, 2021.**  
Caption the same as Supplemental Figure S5.

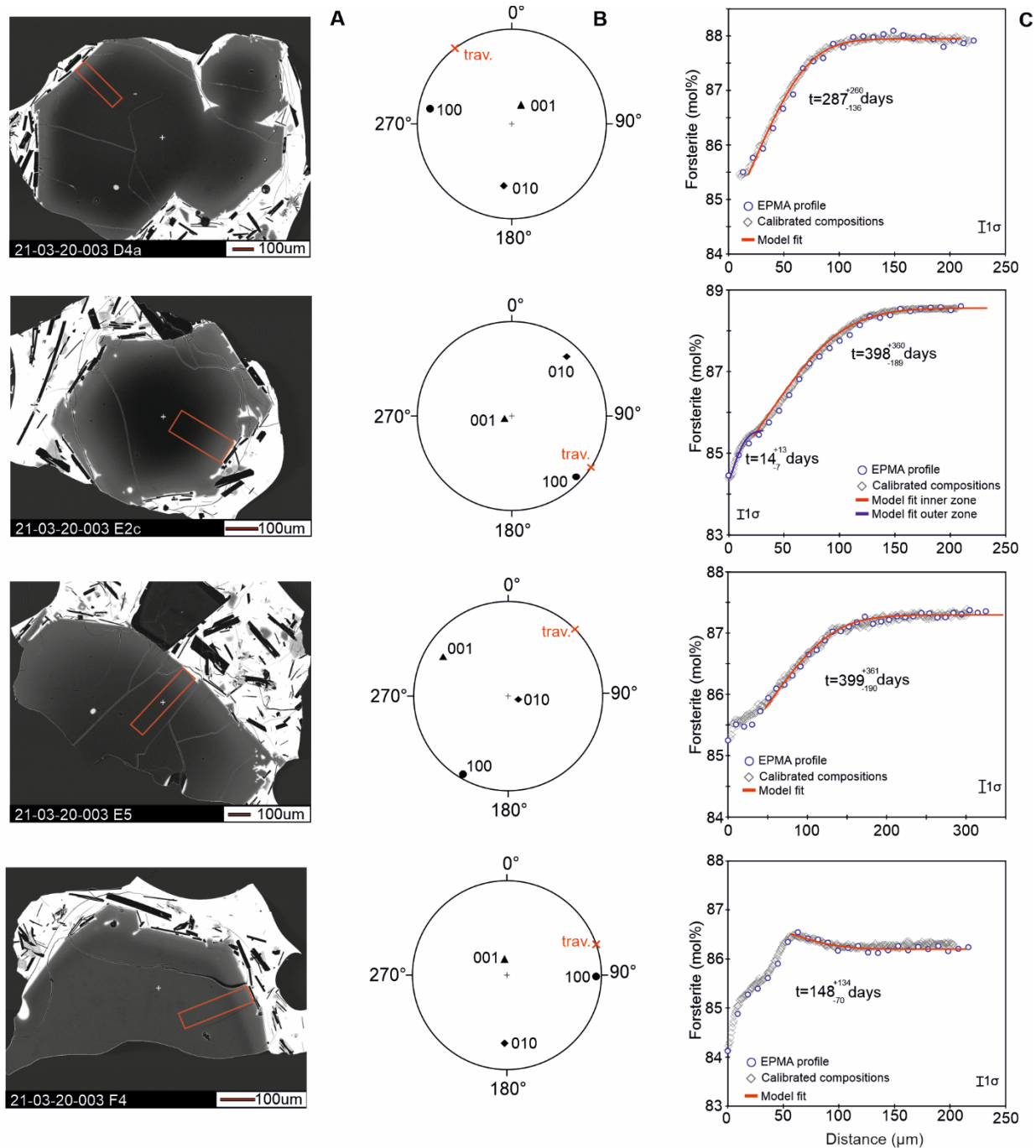


**Fig. S27. Data, initial conditions and best fit olivine diffusion models – March 20, 2021.**  
Caption the same as Supplemental Figure S5.

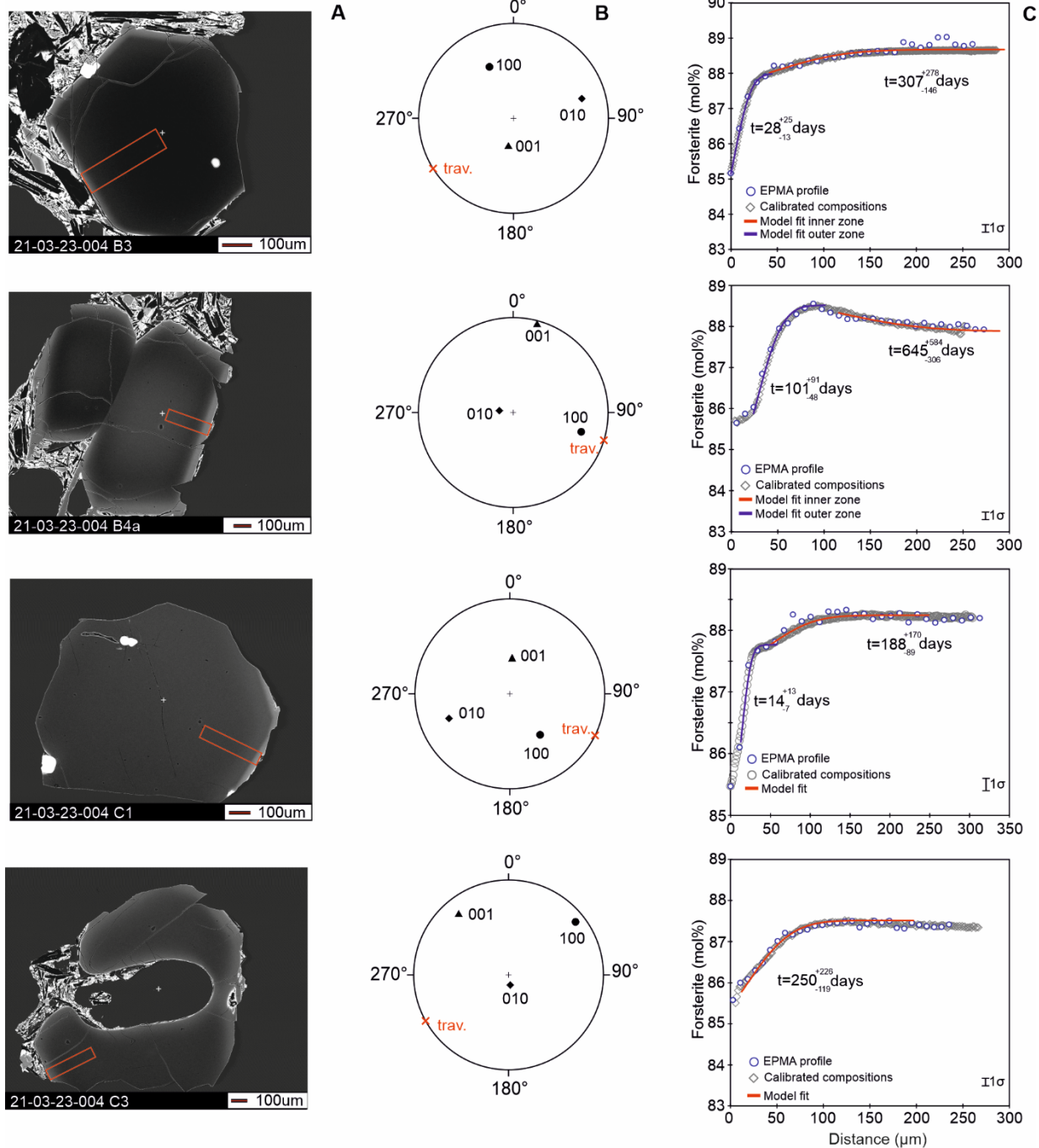


**Fig. S28. Data, initial conditions and best fit olivine diffusion models – March 23, 2021.**  
Caption the same as Supplemental Figure S5.

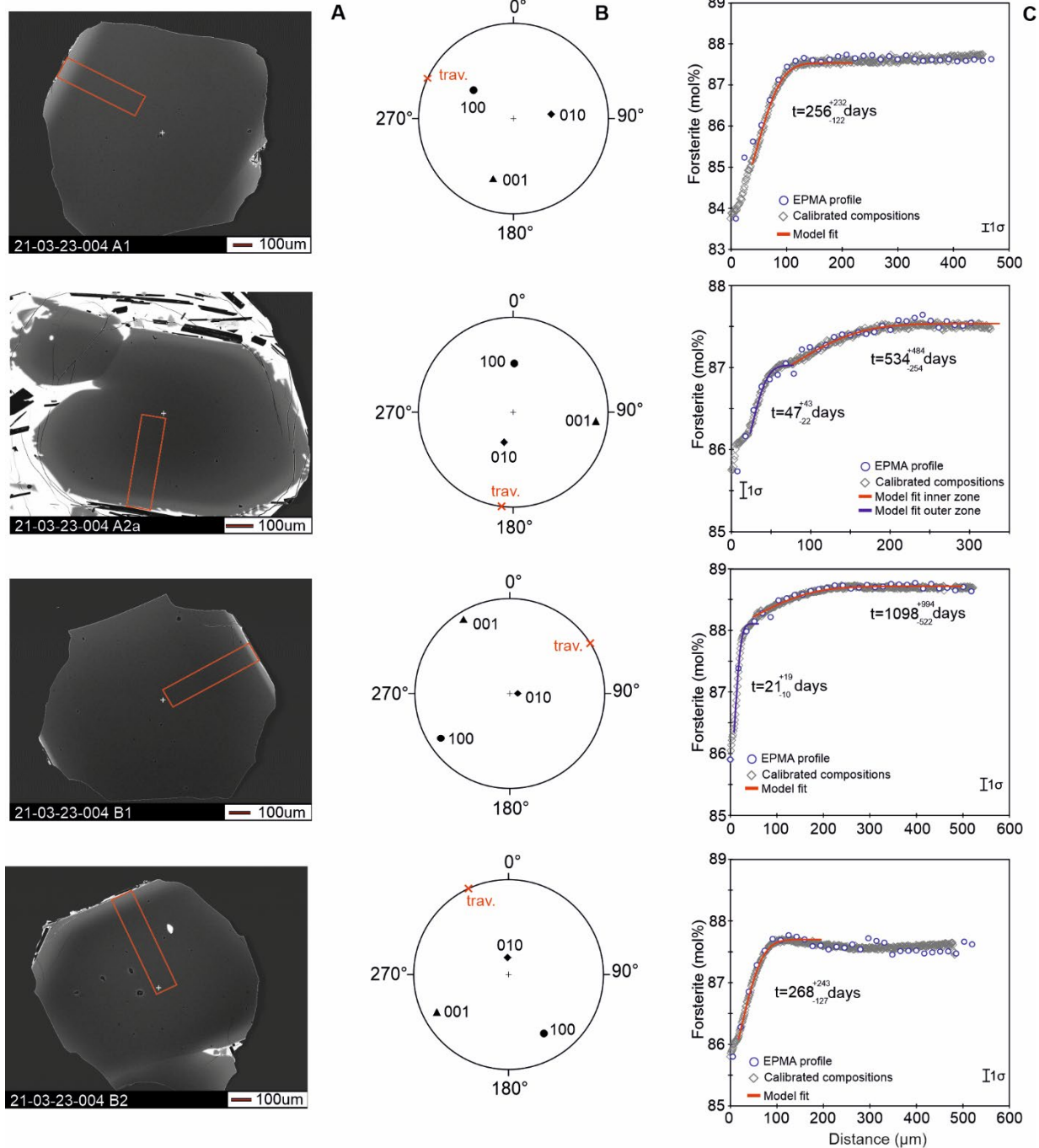


**Fig. S29. Data, initial conditions and best fit olivine diffusion models – March 23, 2021.**  
Caption the same as Supplemental Figure S5.

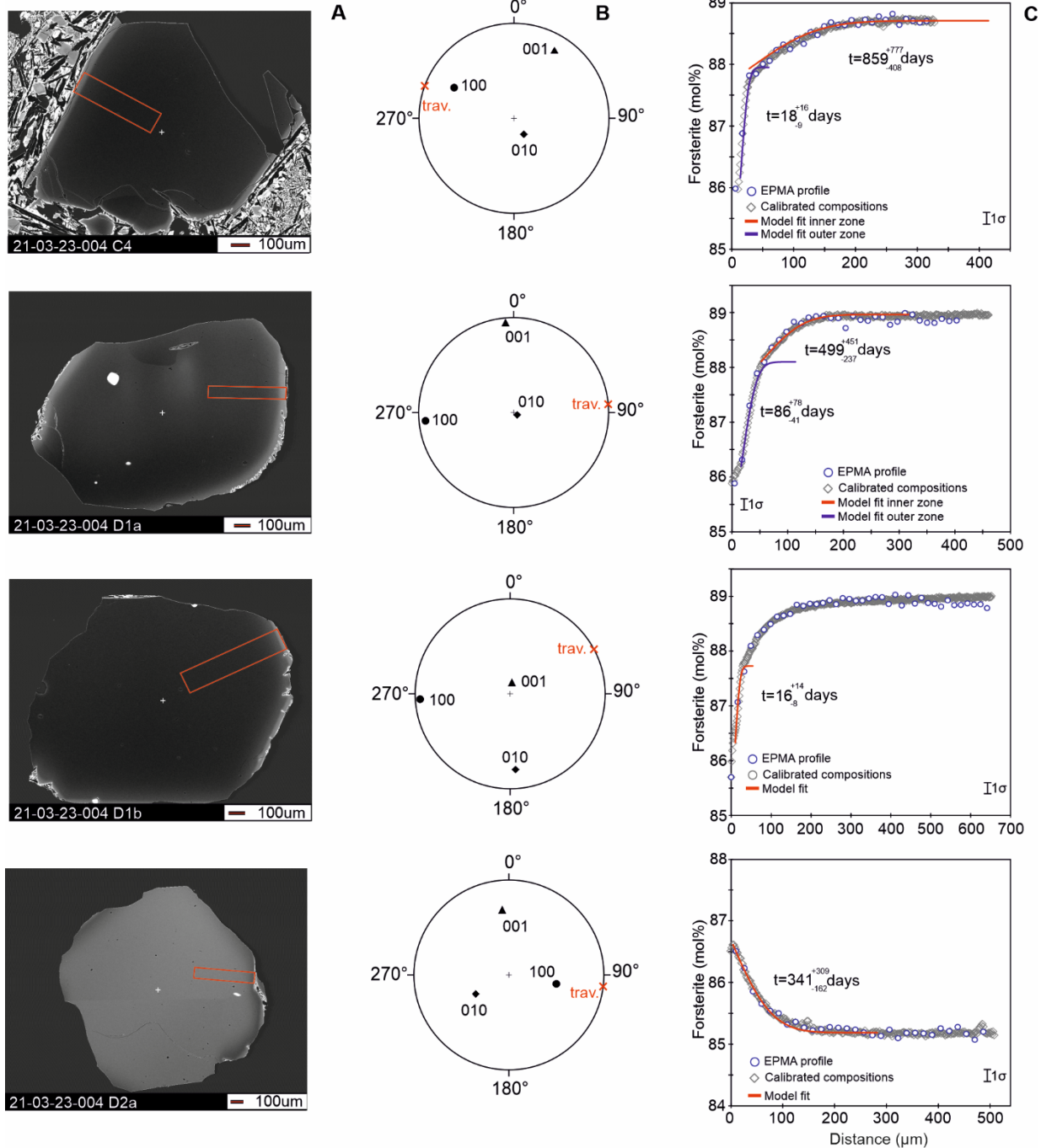


**Fig. S30. Data, initial conditions and best fit olivine diffusion models – March 23, 2021.**  
Caption the same as Supplemental Figure S5.

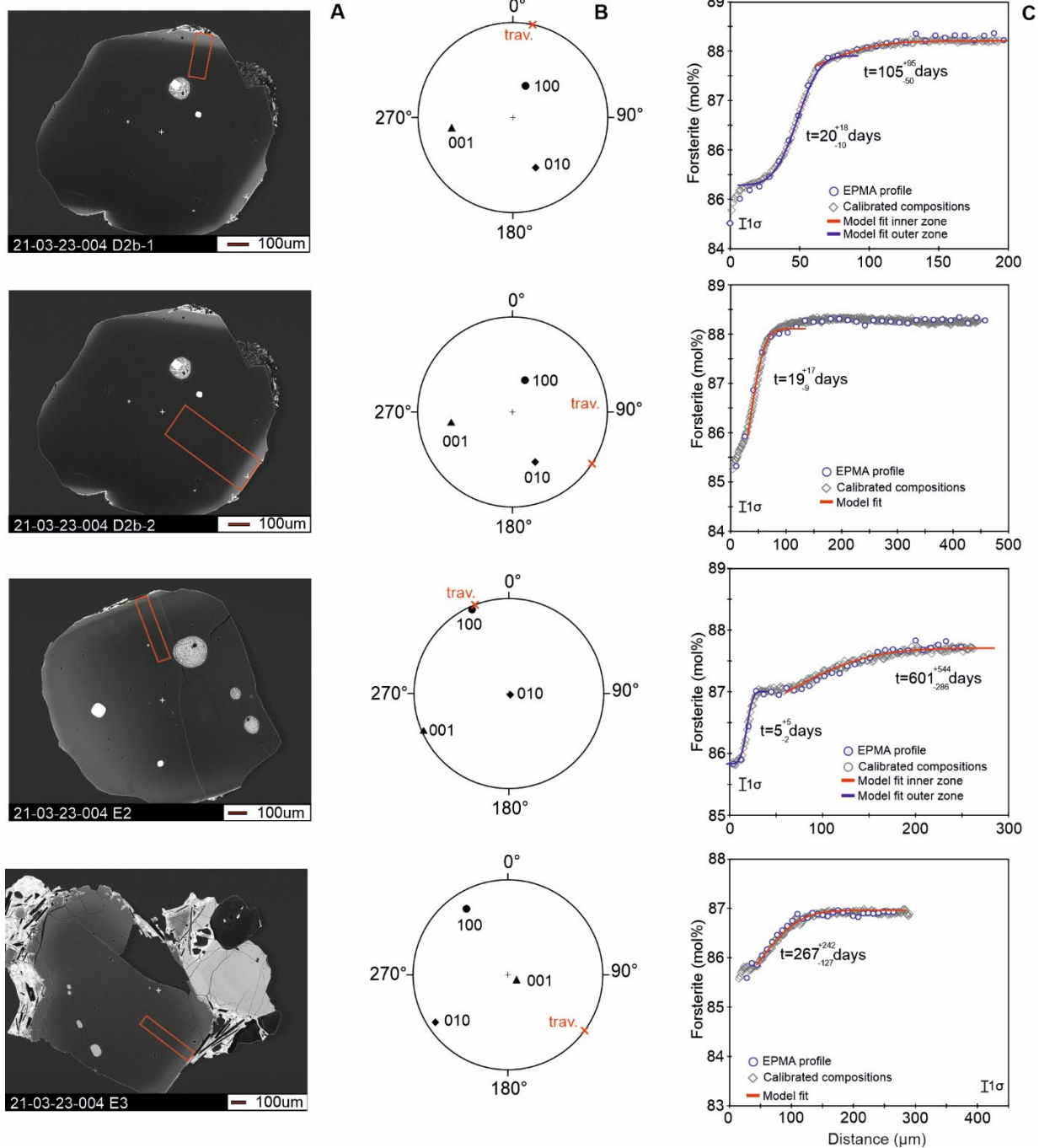


**Fig. S31. Data, initial conditions and best fit olivine diffusion models – March 23, 2021.**  
Caption the same as Supplemental Figure S5.

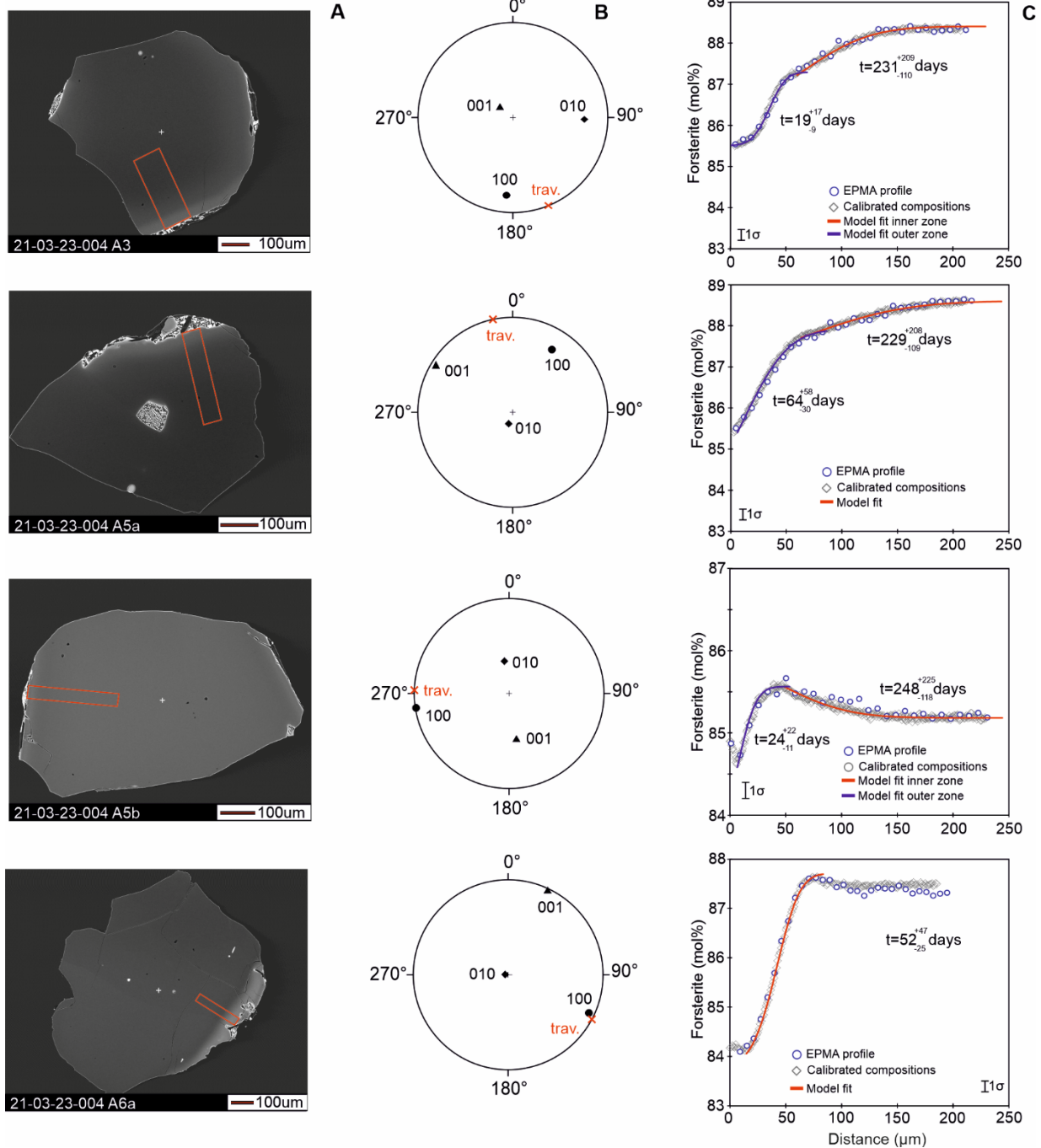


**Fig. S32. Data, initial conditions and best fit olivine diffusion models – March 23, 2021.**  
Caption the same as Supplemental Figure S5.

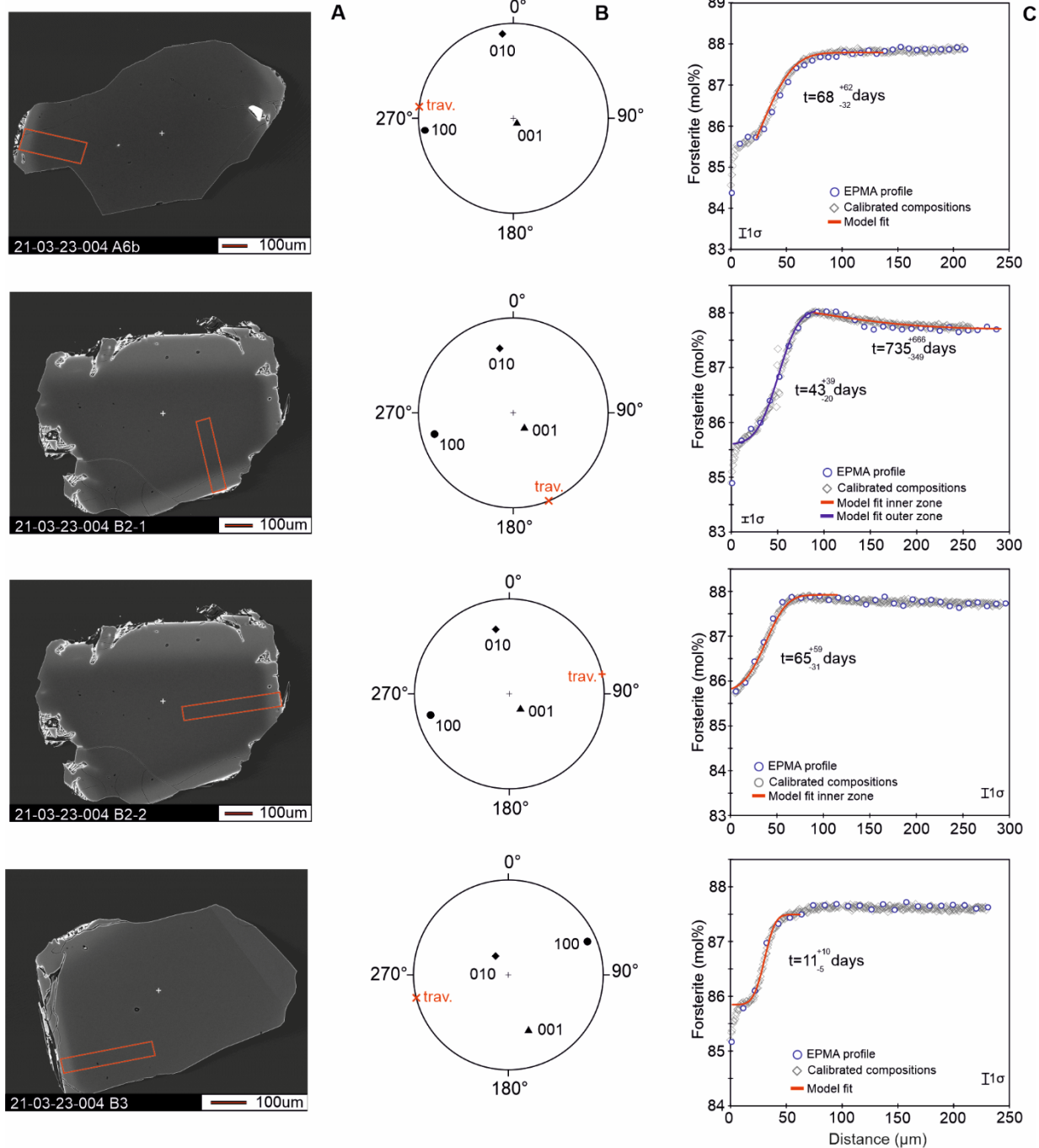


**Fig. S33. Data, initial conditions and best fit olivine diffusion models – March 23, 2021.**  
Caption the same as Supplemental Figure S5.

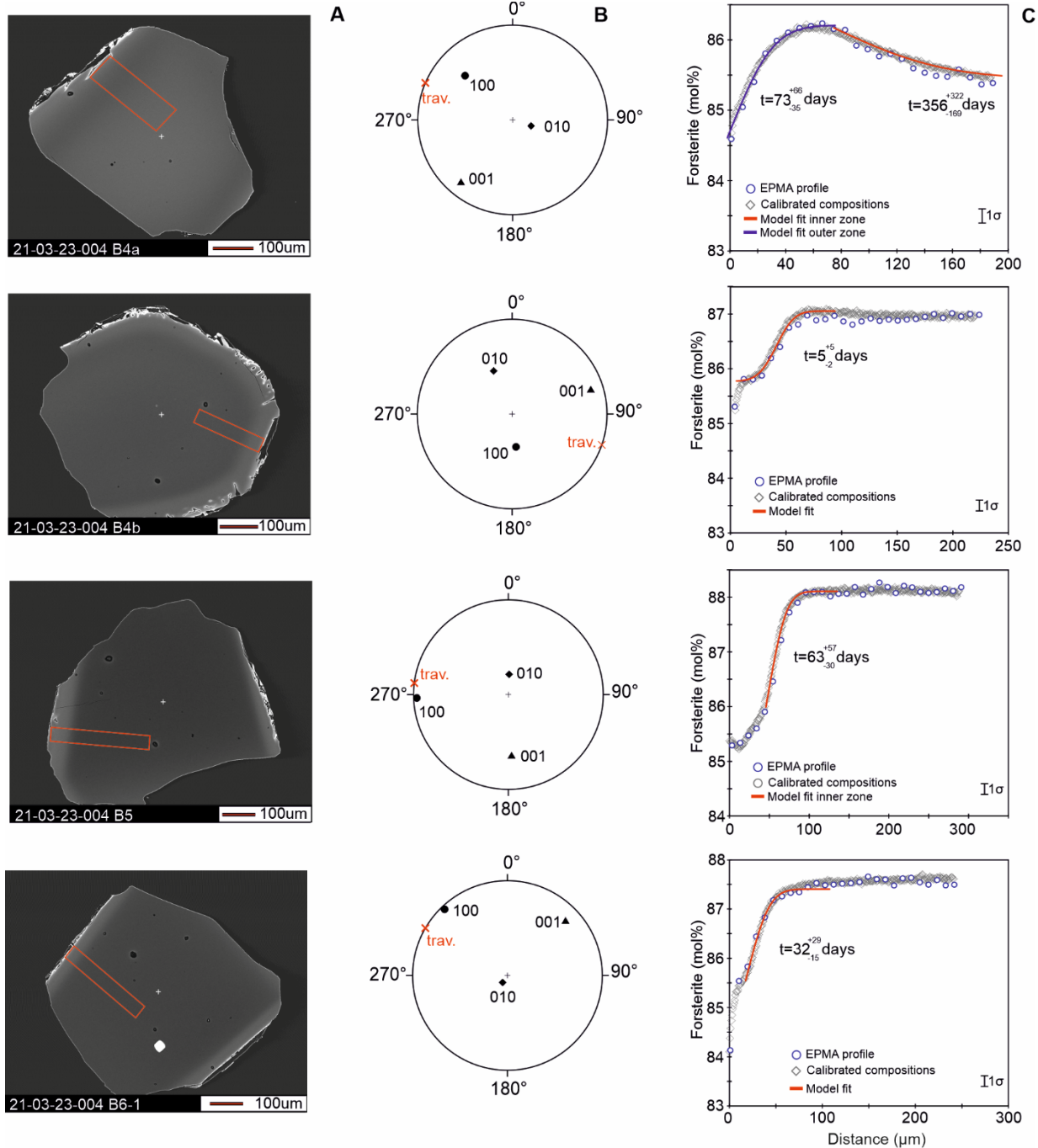


**Fig. S34. Data, initial conditions and best fit olivine diffusion models – March 23, 2021.**  
Caption the same as Supplemental Figure S5.

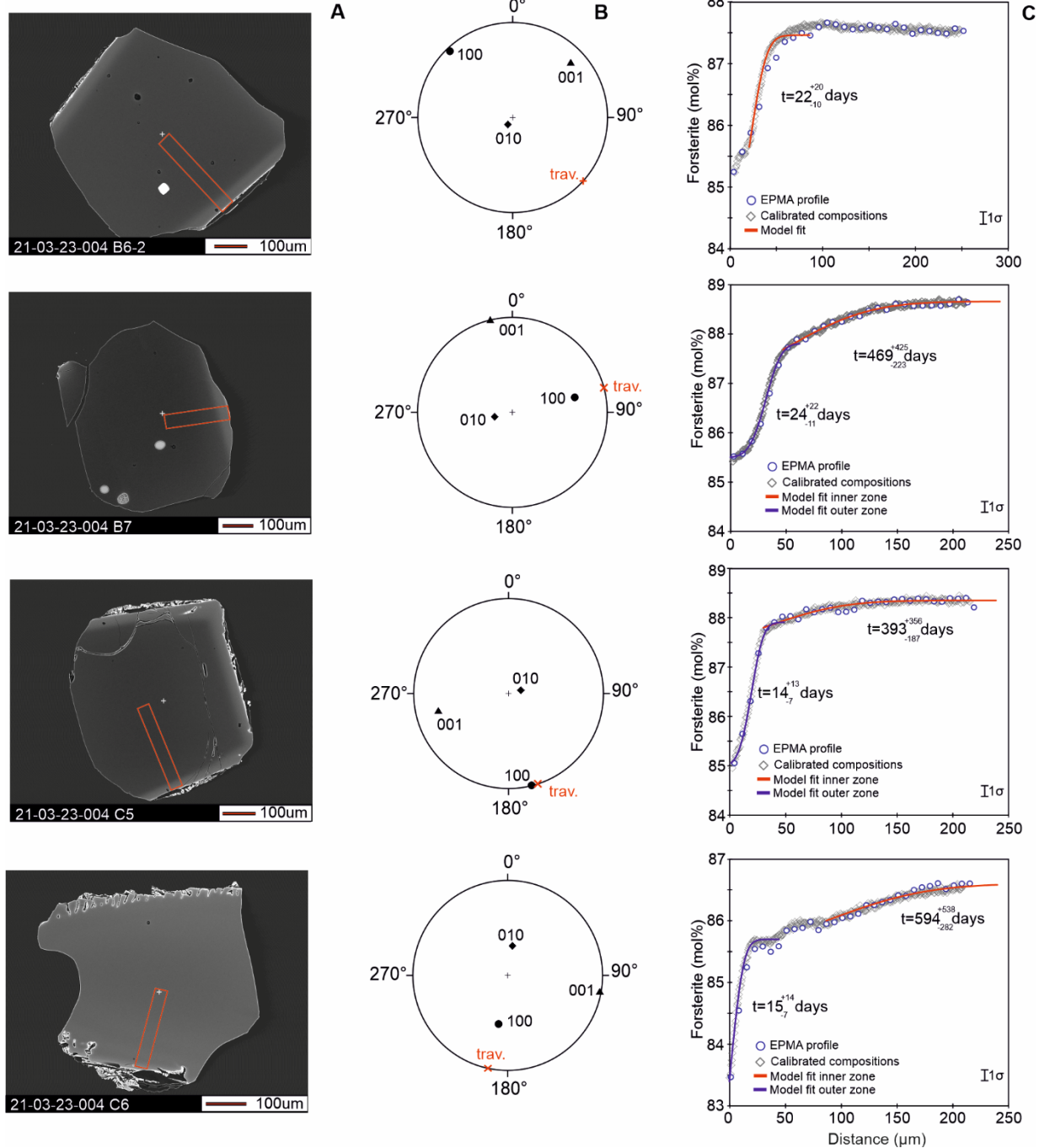


**Fig. S35. Data, initial conditions and best fit olivine diffusion models – March 23, 2021.**  
Caption the same as Supplemental Figure S5.

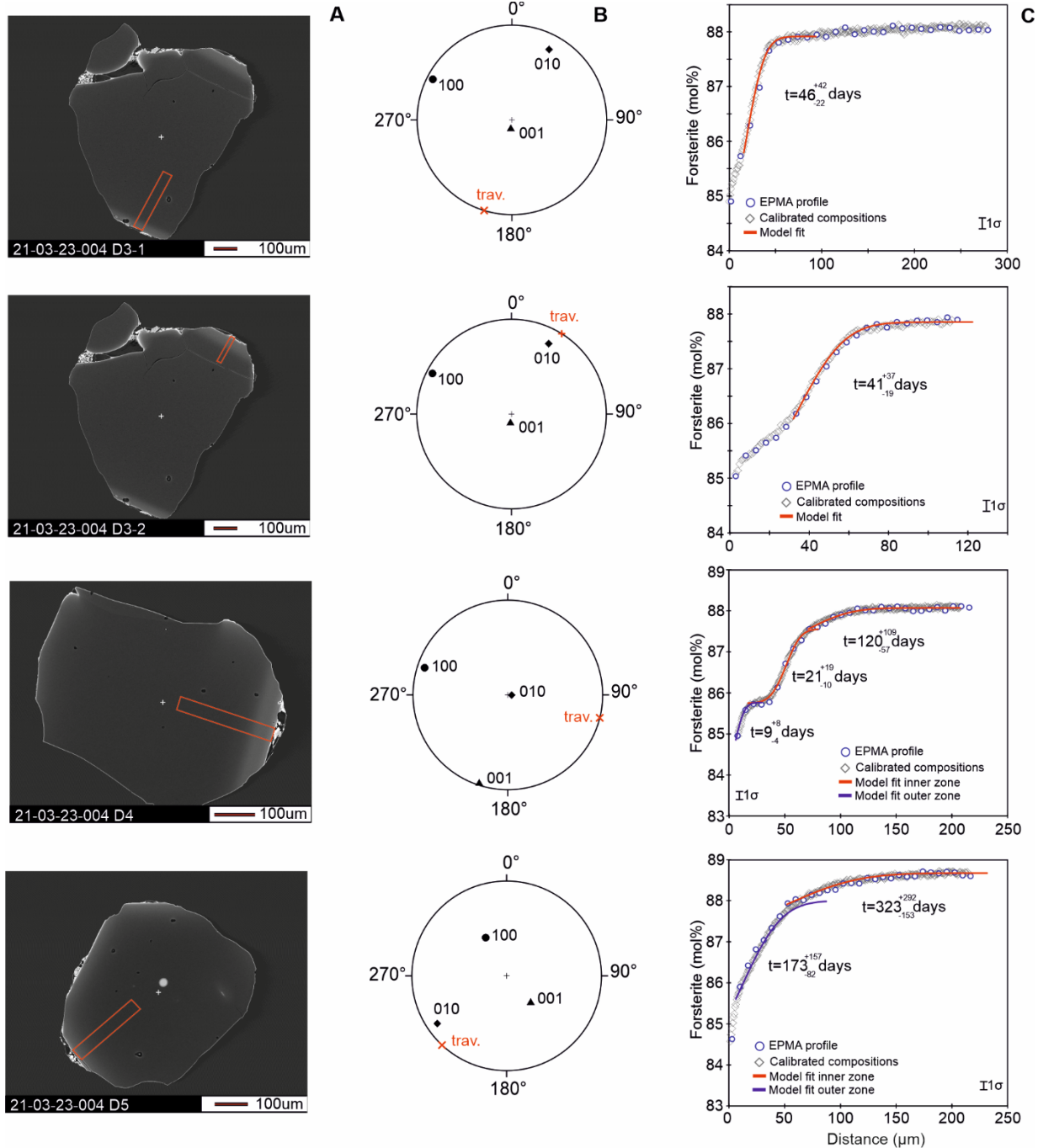


**Fig. S36. Data, initial conditions and best fit olivine diffusion models – March 23, 2021.**  
Caption the same as Supplemental Figure S5.

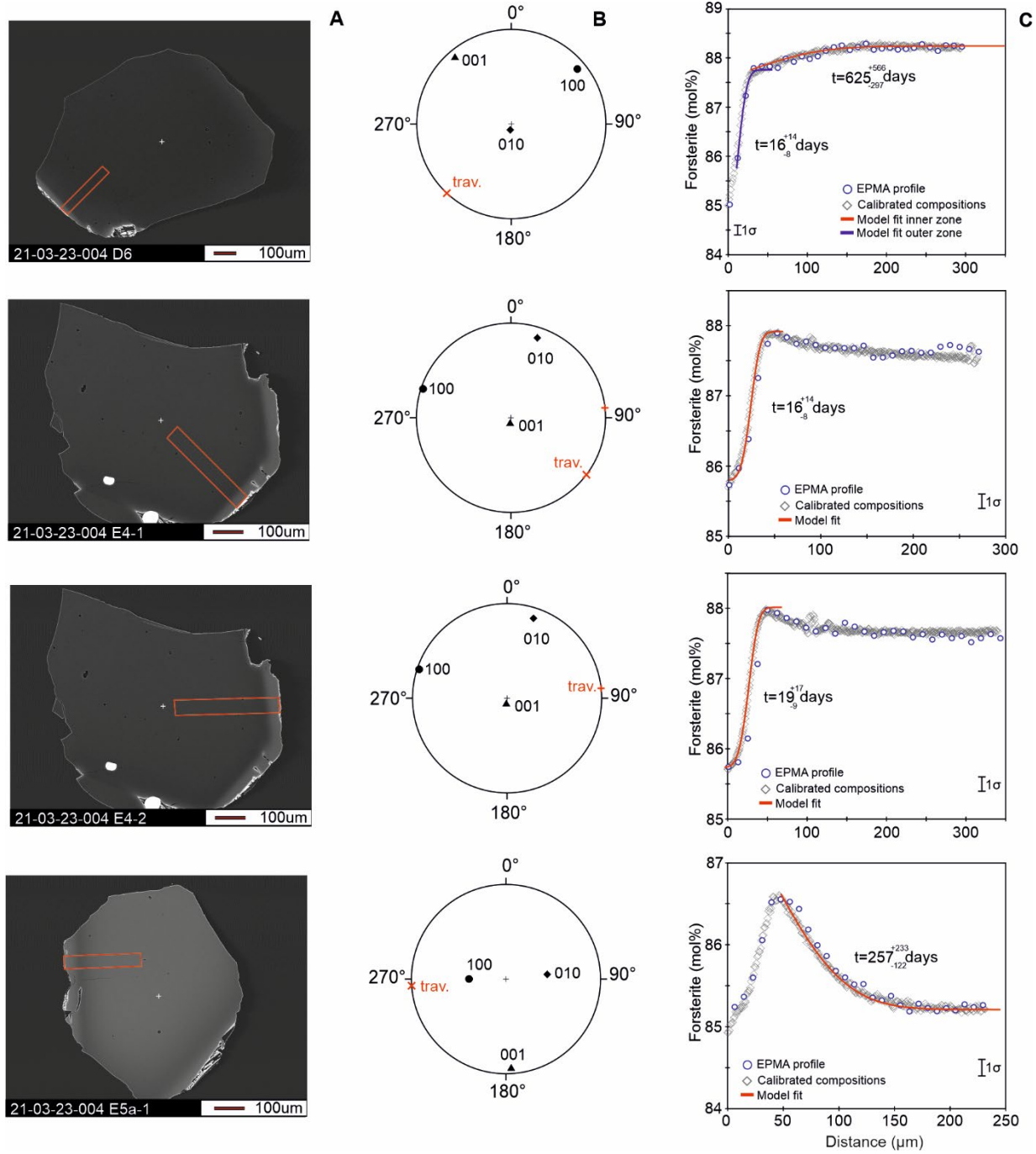


**Fig. S37. Data, initial conditions and best fit olivine diffusion models – March 23, 2021.**  
Caption the same as Supplemental Figure S5.

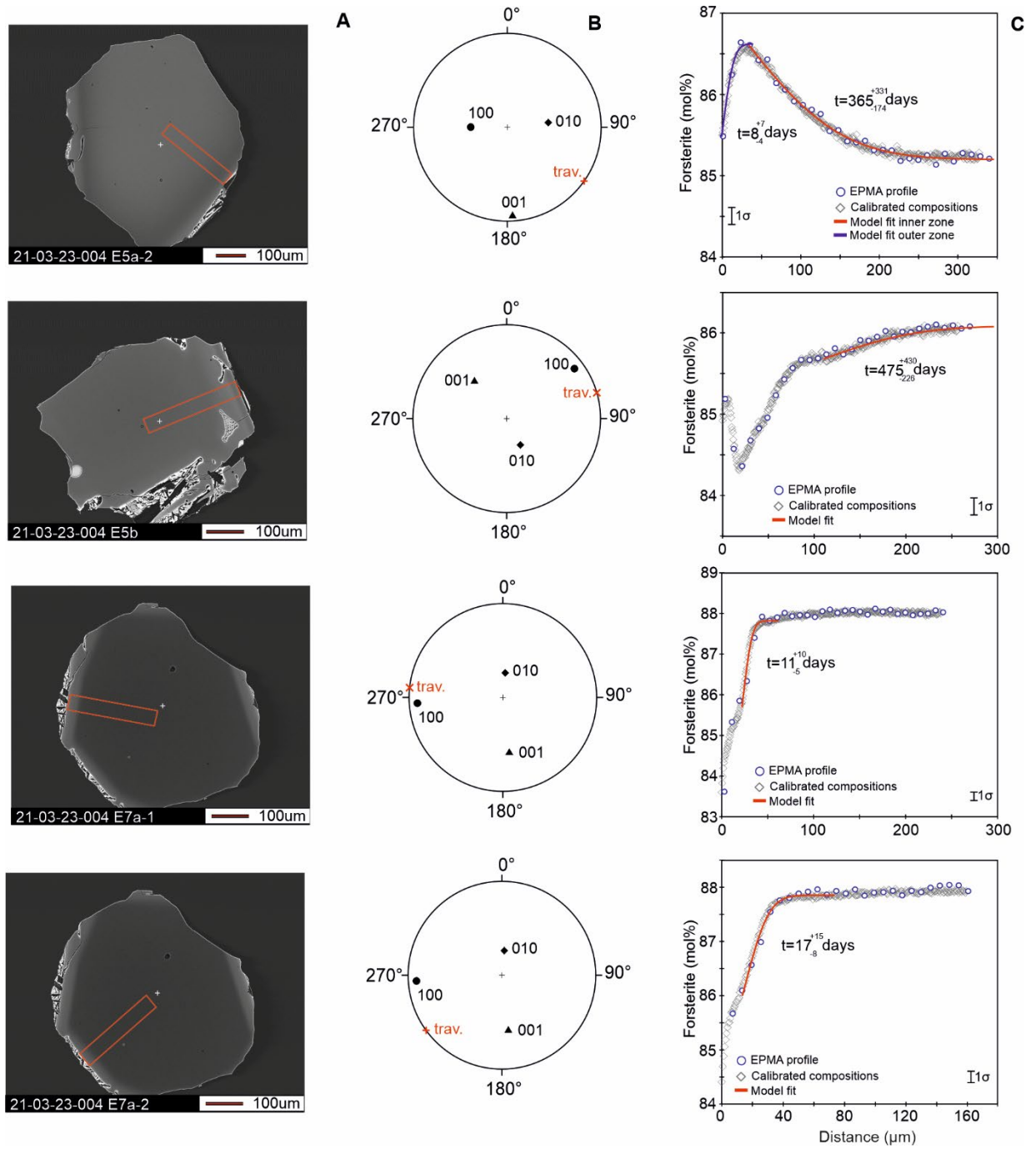


**Fig. S38. Data, initial conditions and best fit olivine diffusion models – March 23, 2021.**  
Caption the same as Supplemental Figure S5.

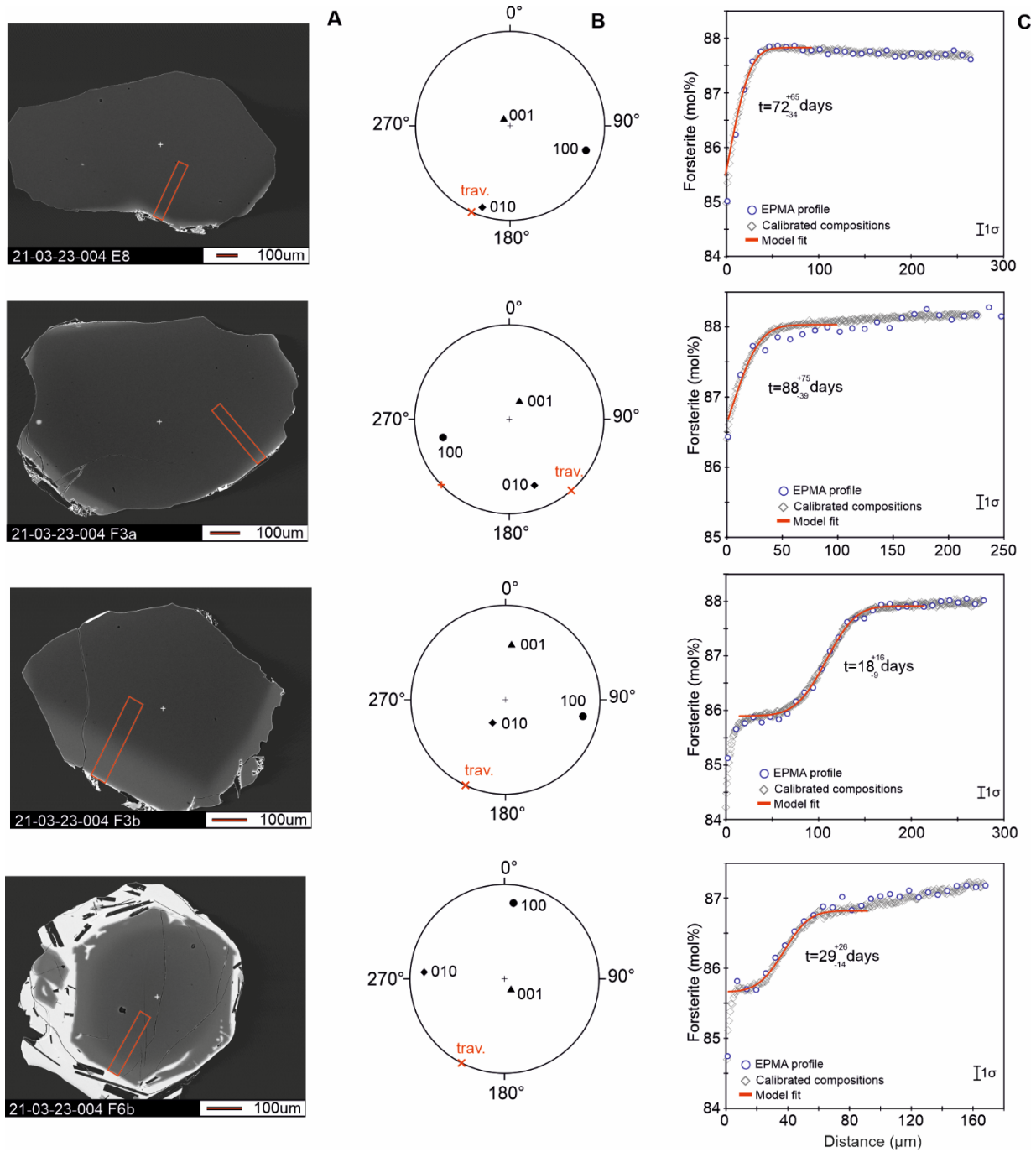


**Fig. S39. Data, initial conditions and best fit olivine diffusion models – March 23, 2021.**  
Caption the same as Supplemental Figure S5.

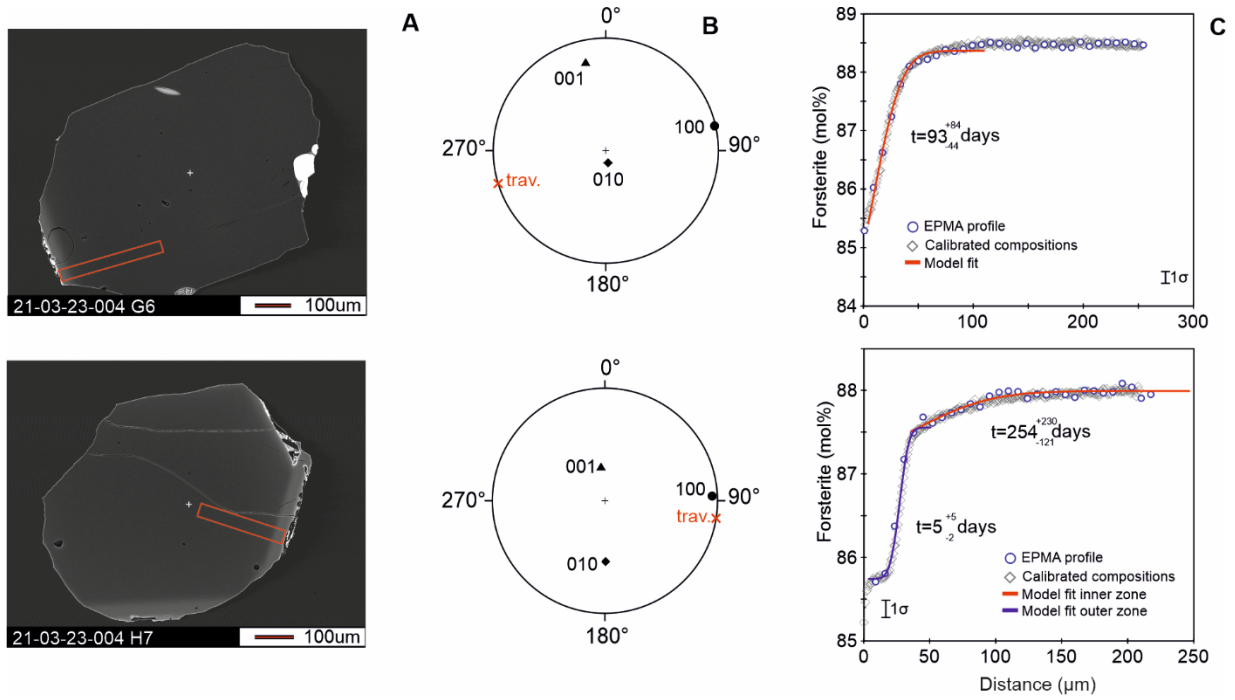


**Fig. S40. Data, initial conditions and best fit olivine diffusion models – March 23, 2021.**  
Caption the same as Supplemental Figure S5.

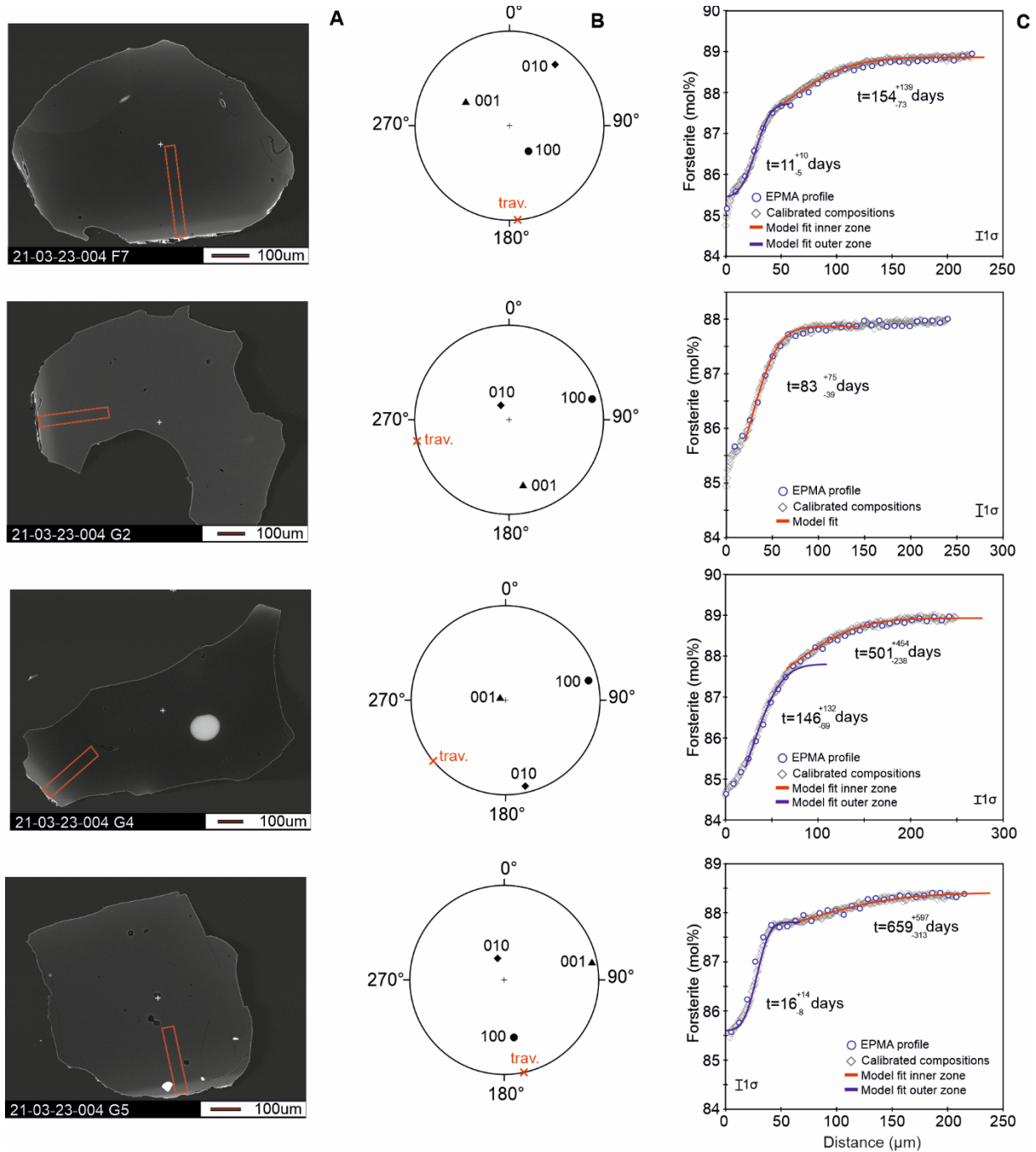


**Fig. S41. Data, initial conditions and best fit olivine diffusion models – March 23, 2021.**  
Caption the same as Supplemental Figure S5.

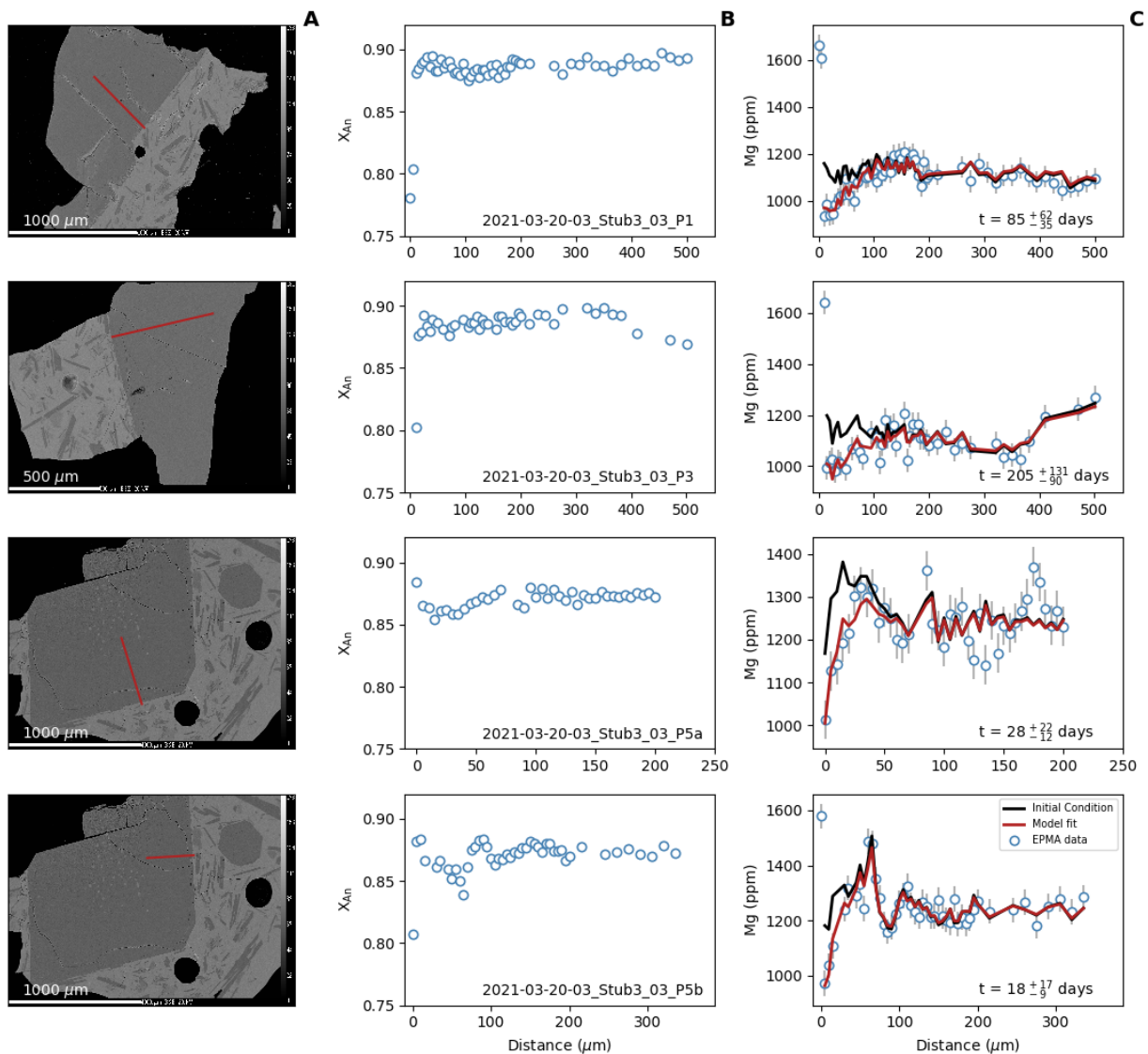


**Fig. S42. Data, initial conditions and best fit plagioclase diffusion models – March 20, 2021.** (A) Backscattered electron (BSE) images of the analyzed plagioclase crystals. The red lines indicate positions of EMP traverses. (B) Rim to core major element composition profiles of plagioclase crystals. Composition is expressed as anorthite content ( $X_{An} = Ca/(Ca + Na)$ ) in mol fraction. (C) Core to rim EMP traverses showing concentration profiles for Mg. Red lines, best-fit diffusion models for the observed zoning profiles. Black lines, model initial conditions. Numbers in days indicate diffusive timescales obtained from best-fit model solutions and their associated uncertainties.

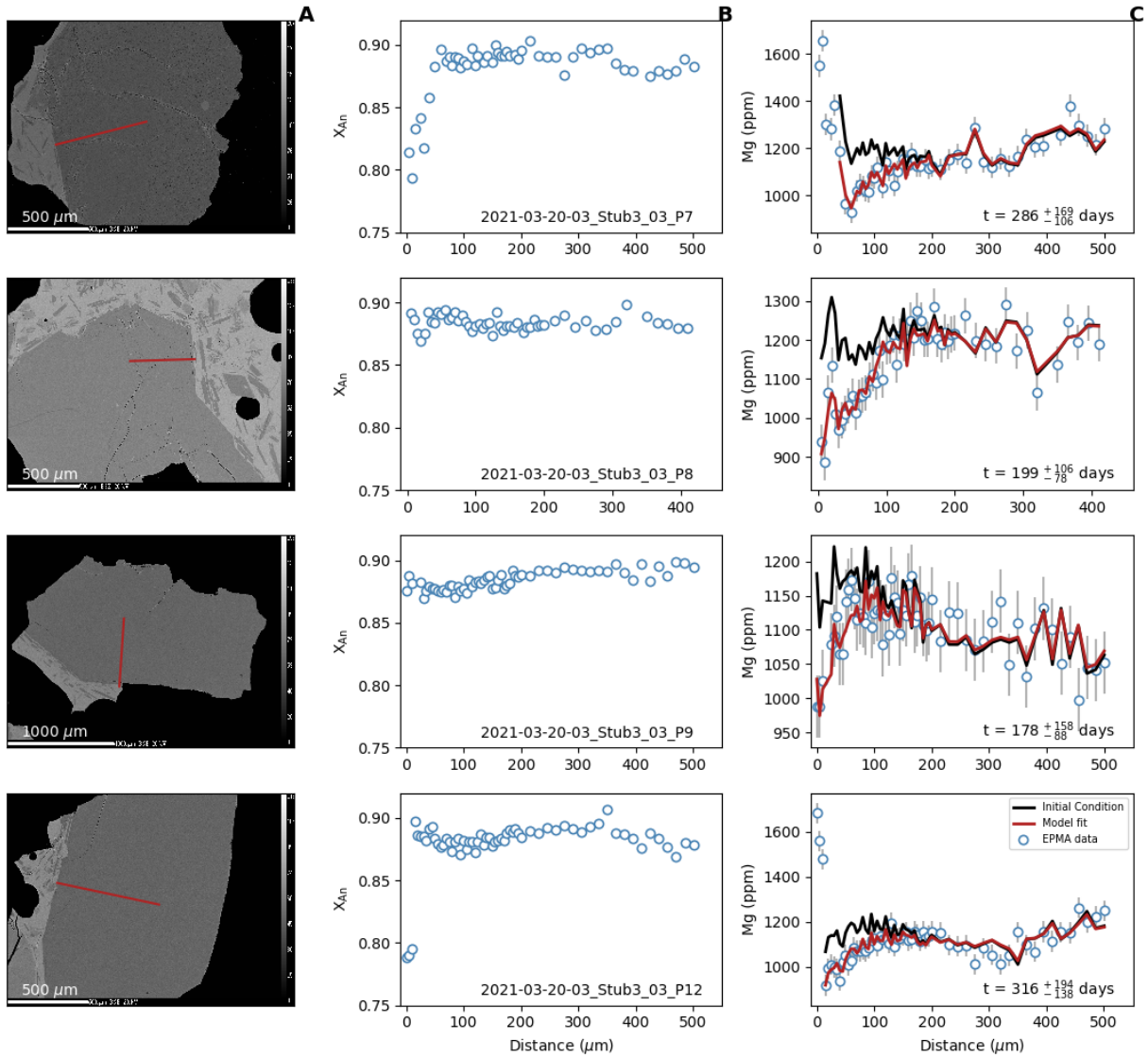


**Fig. S43. Data, initial conditions and best fit plagioclase diffusion models – March 20, 2021.**  
Caption the same as Supplemental Figure S43.

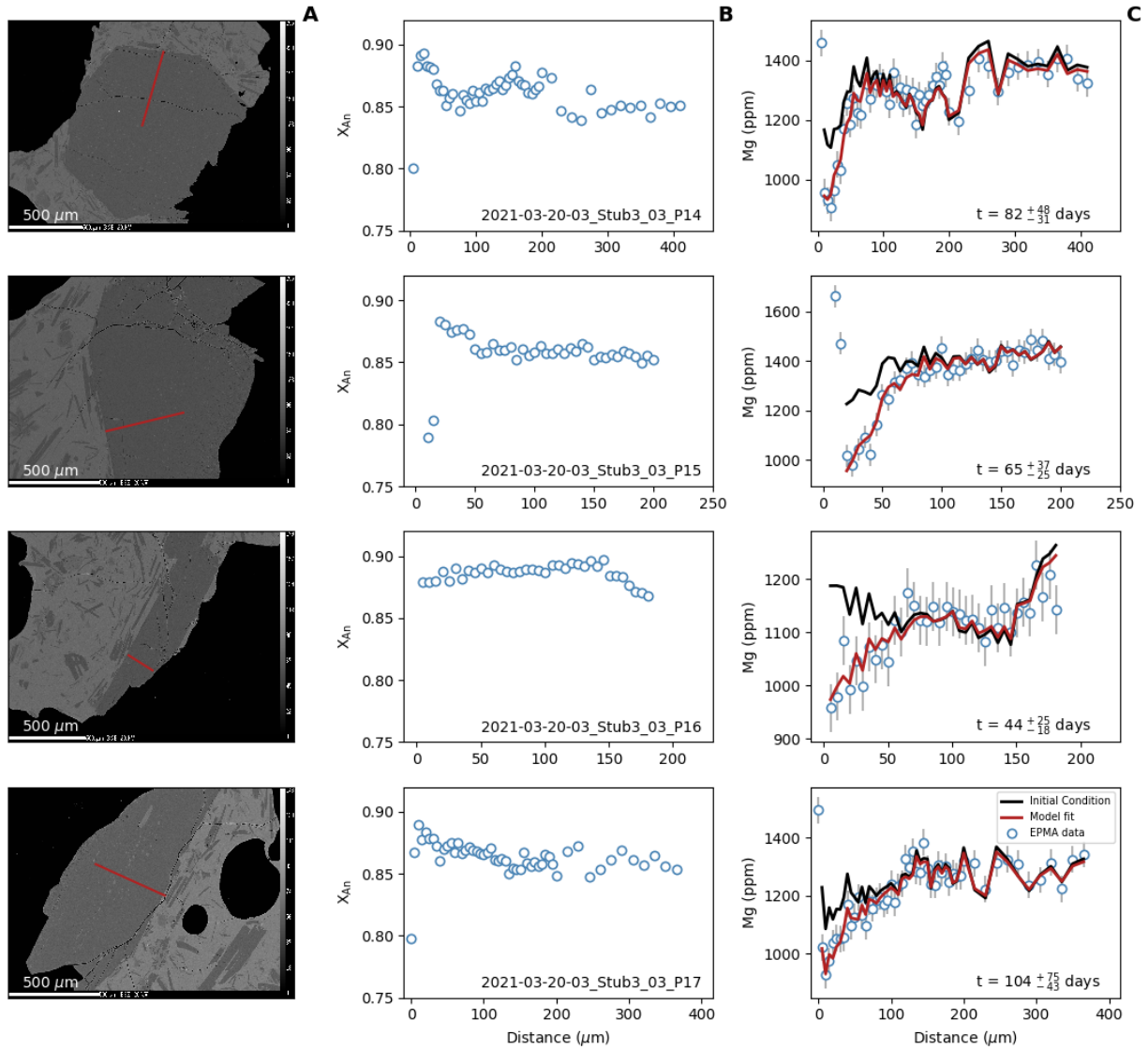


**Fig. S44. Data, initial conditions and best fit plagioclase diffusion models – March 20, 2021.**  
Caption the same as Supplemental Figure S43.

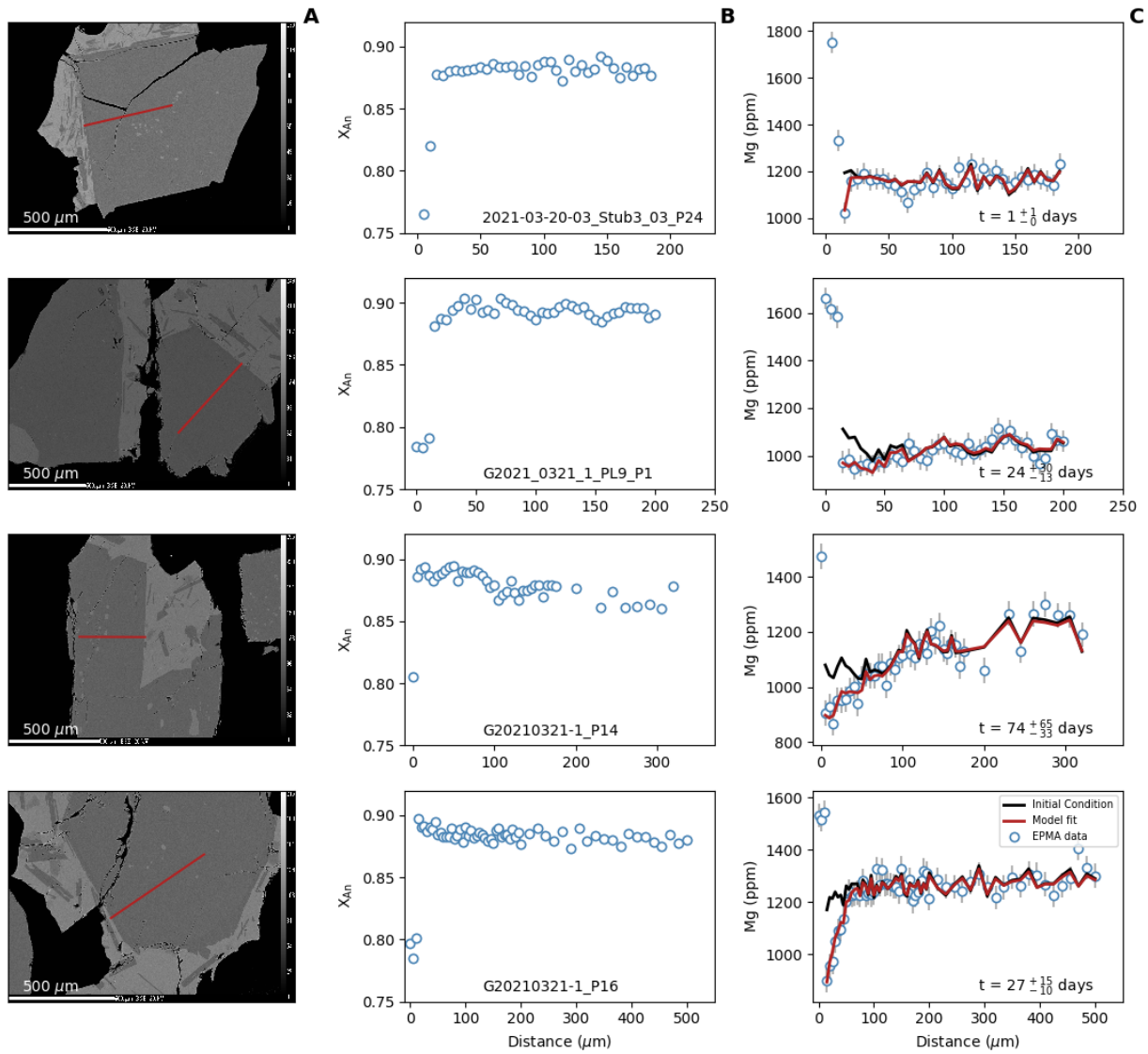


**Fig. S45. Data, initial conditions and best fit plagioclase diffusion models – March 20 & 21, 2021.** Caption the same as Supplemental Figure S43.

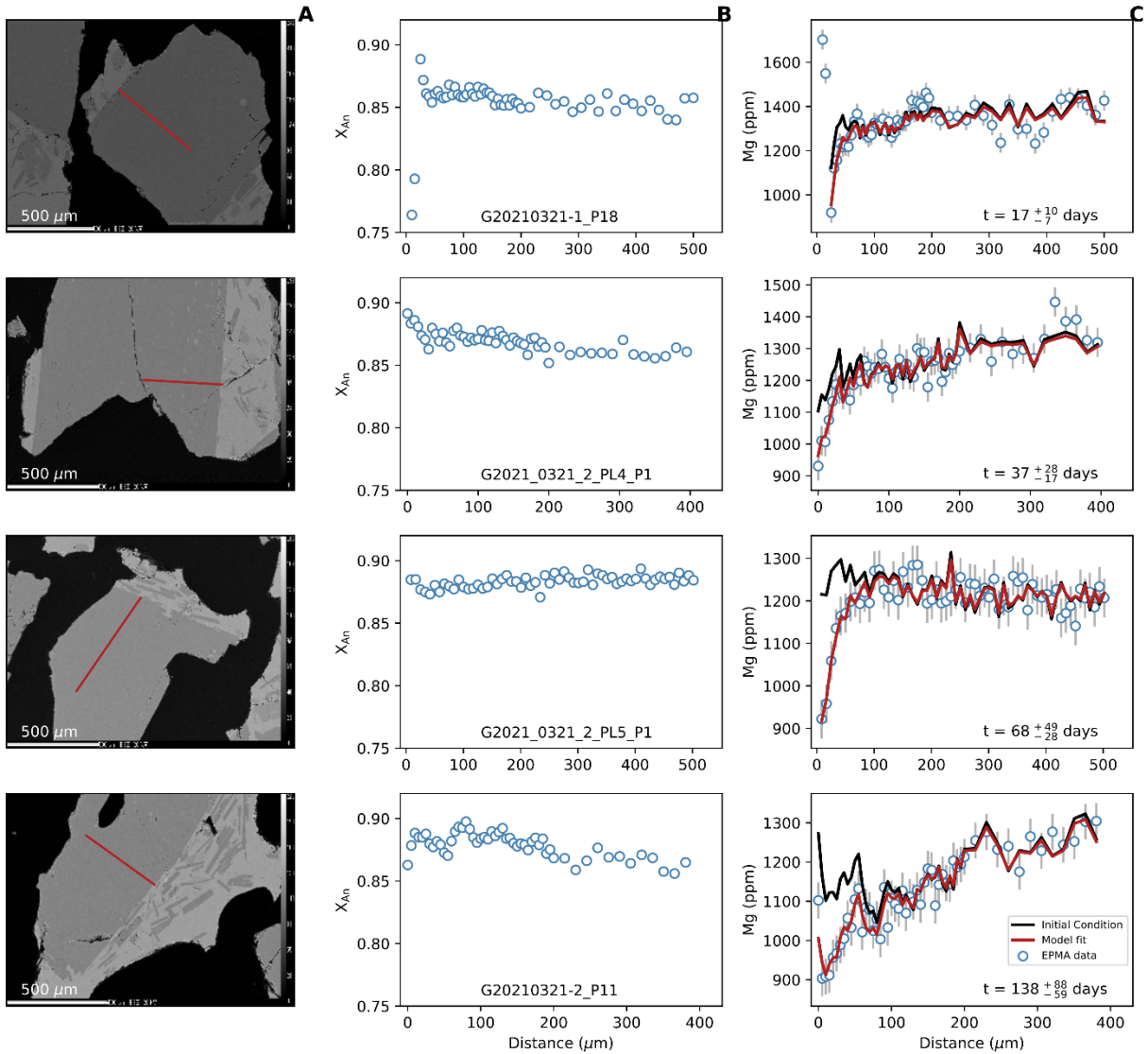


**Fig. S46. Data, initial conditions and best fit plagioclase diffusion models – March 21, 2021.**  
Caption the same as Supplemental Figure S43.

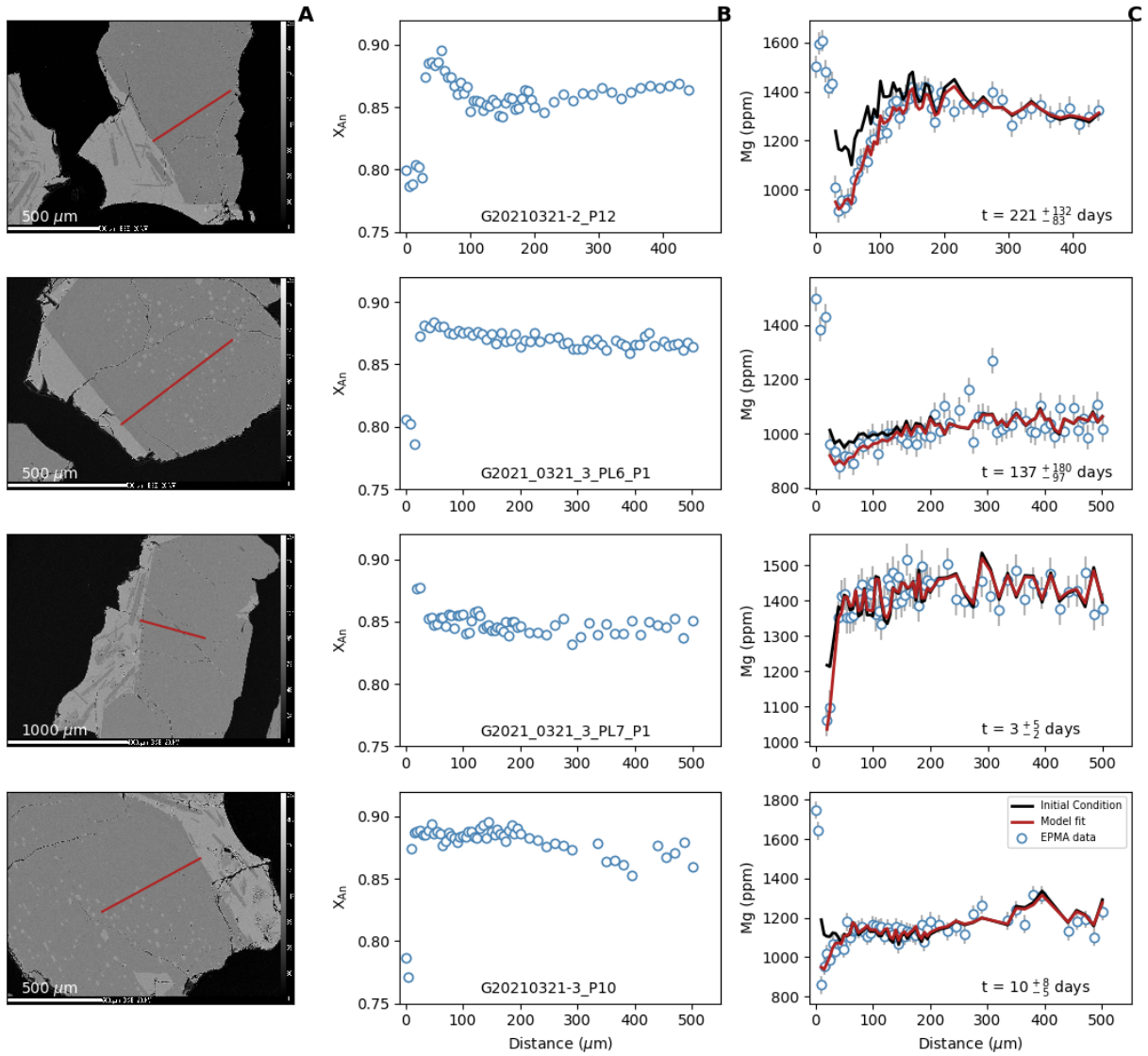


**Fig. S47. Data, initial conditions and best fit plagioclase diffusion models – March 21, 2021.**  
Caption the same as Supplemental Figure S43.

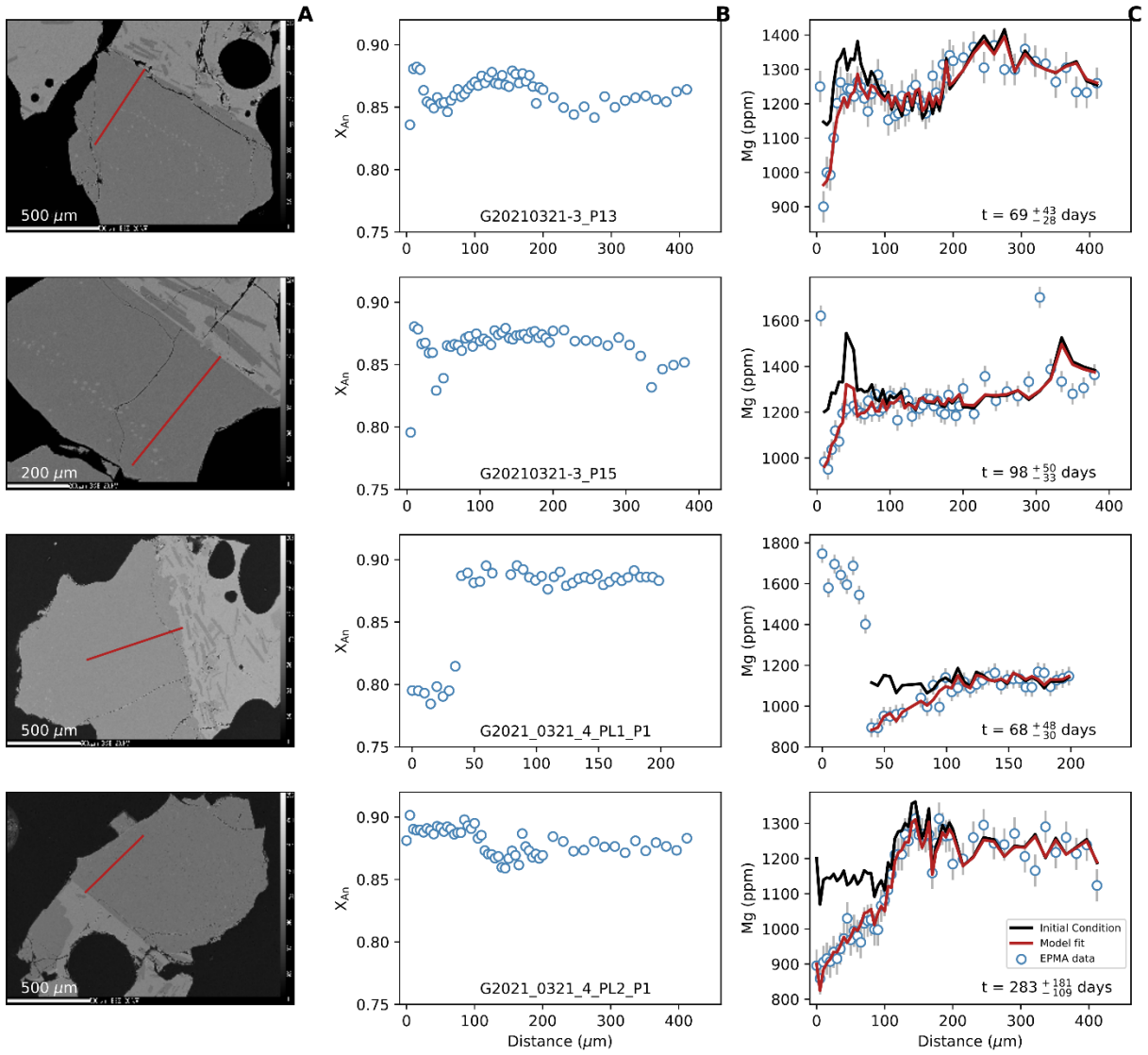


**Fig. S48. Data, initial conditions and best fit plagioclase diffusion models – March 21, 2021.**  
Caption the same as Supplemental Figure S43.

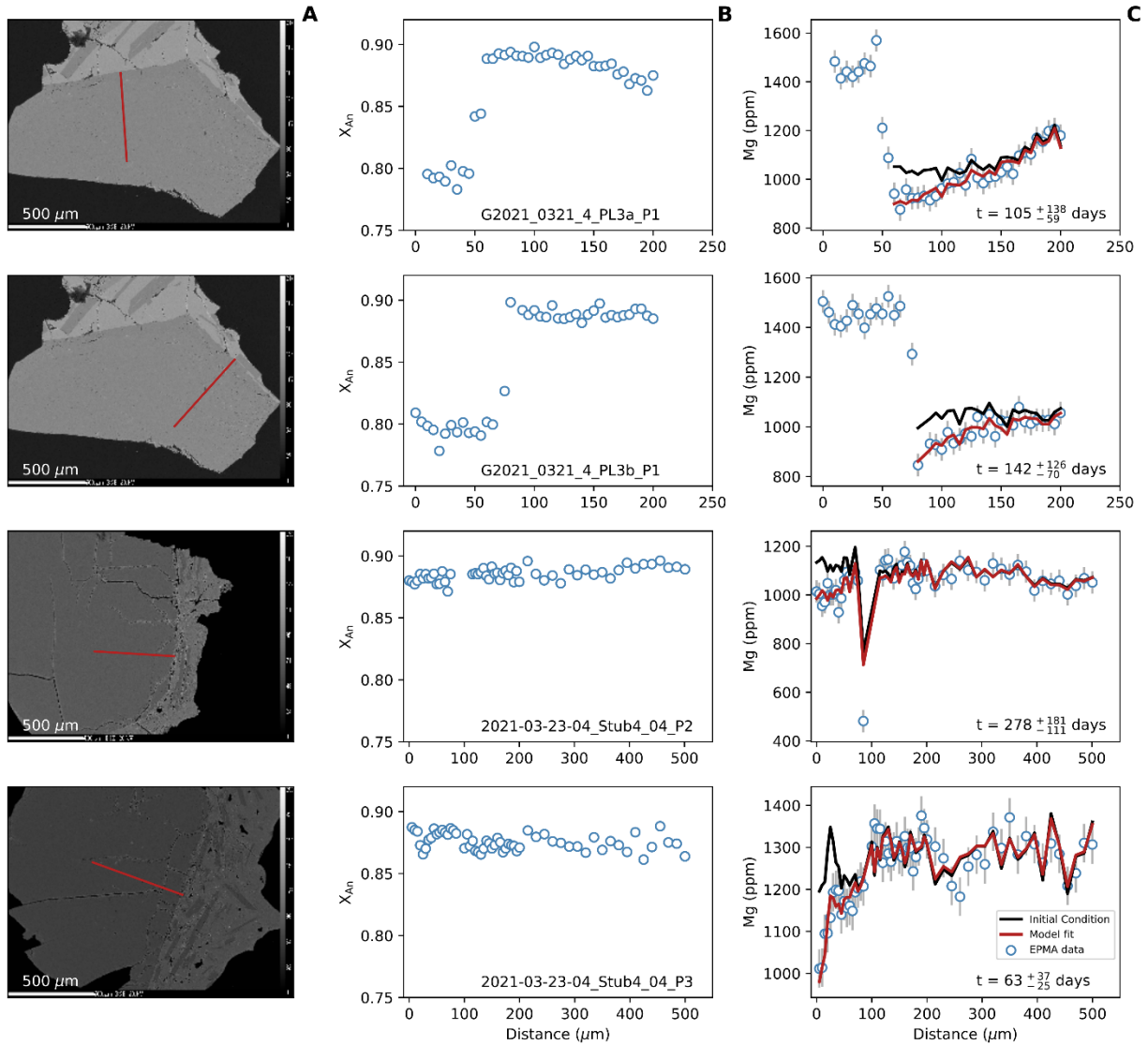


**Fig. S49. Data, initial conditions and best fit plagioclase diffusion models – March 23, 2021.**  
Caption the same as Supplemental Figure S43.

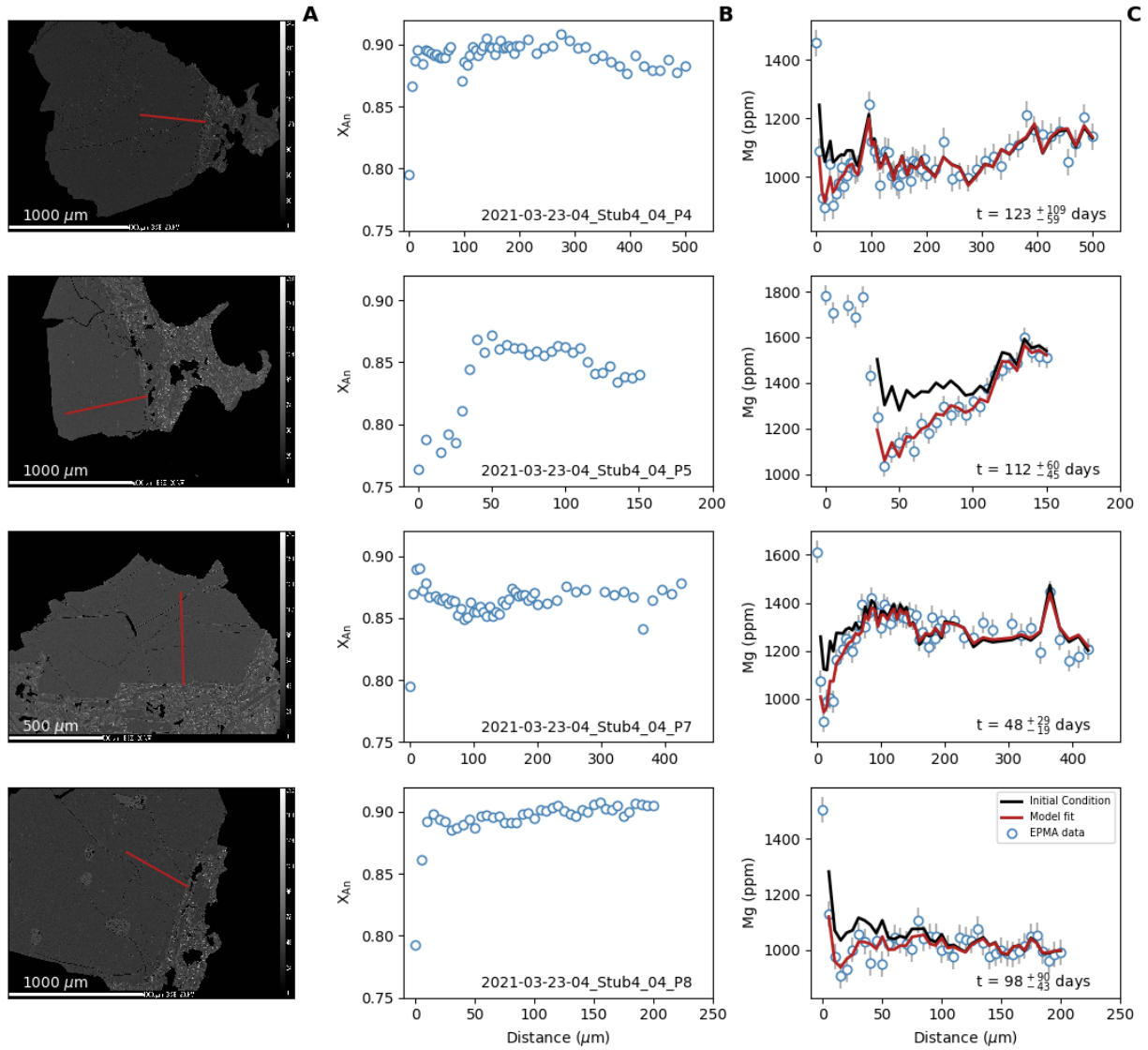


**Fig. S50. Data, initial conditions and best fit plagioclase diffusion models – March 23, 2021.**  
Caption the same as Supplemental Figure S43.

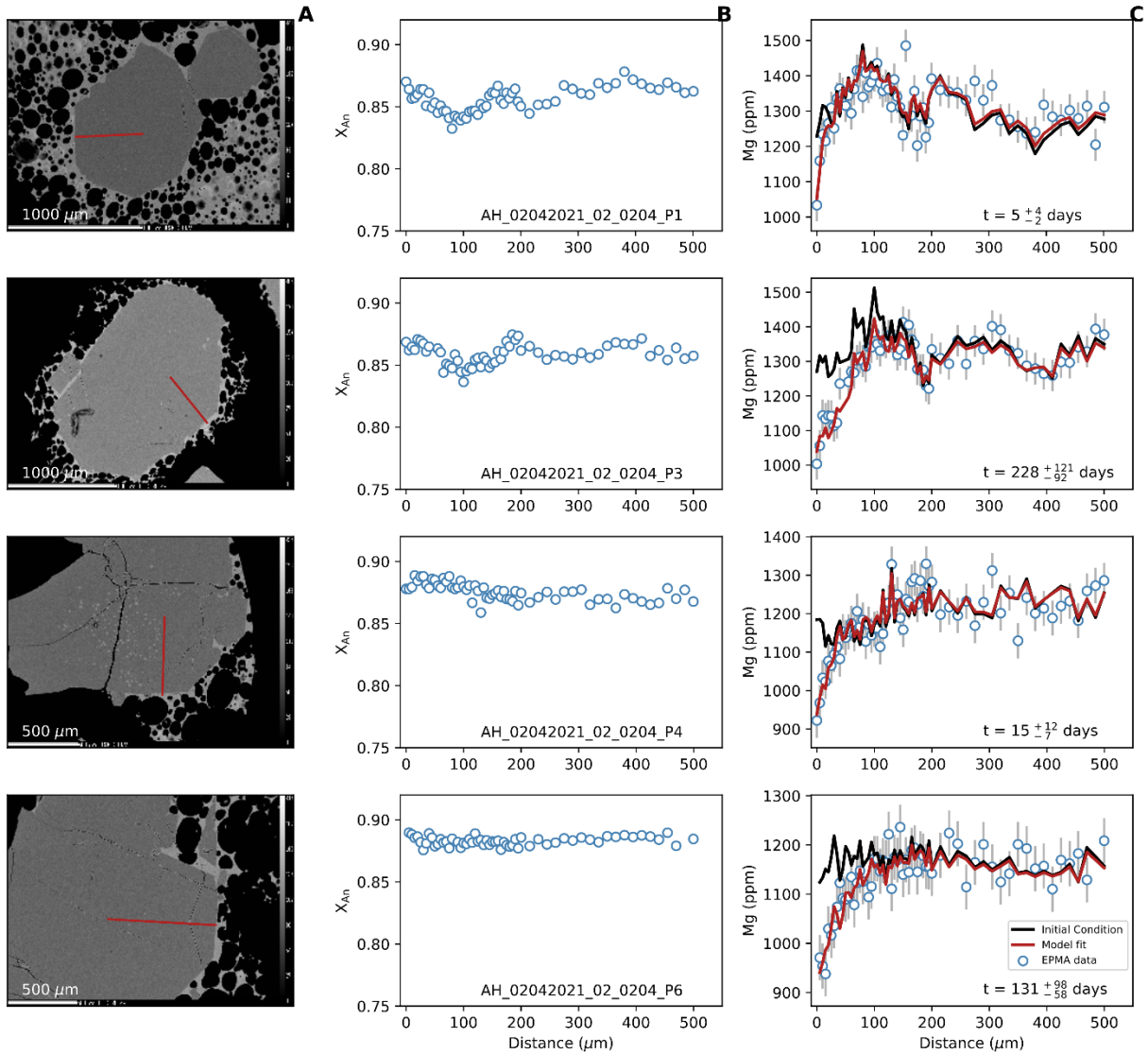


**Fig. S51. Data, initial conditions and best fit plagioclase diffusion models – April 02, 2021.**  
Caption the same as Supplemental Figure S43.

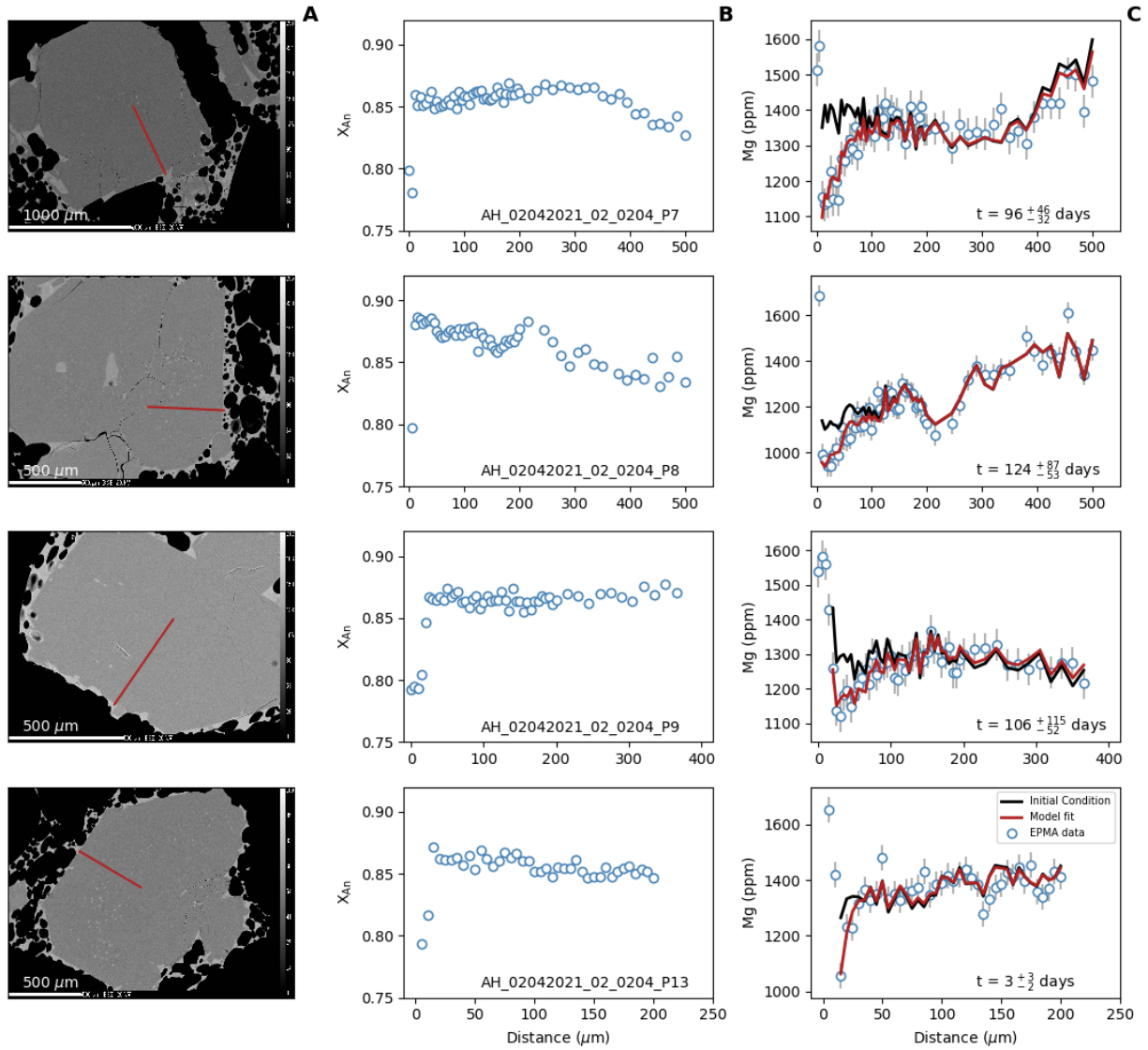


**Fig. S52. Data, initial conditions and best fit plagioclase diffusion models – April 02, 2021.**  
Caption the same as Supplemental Figure S43.

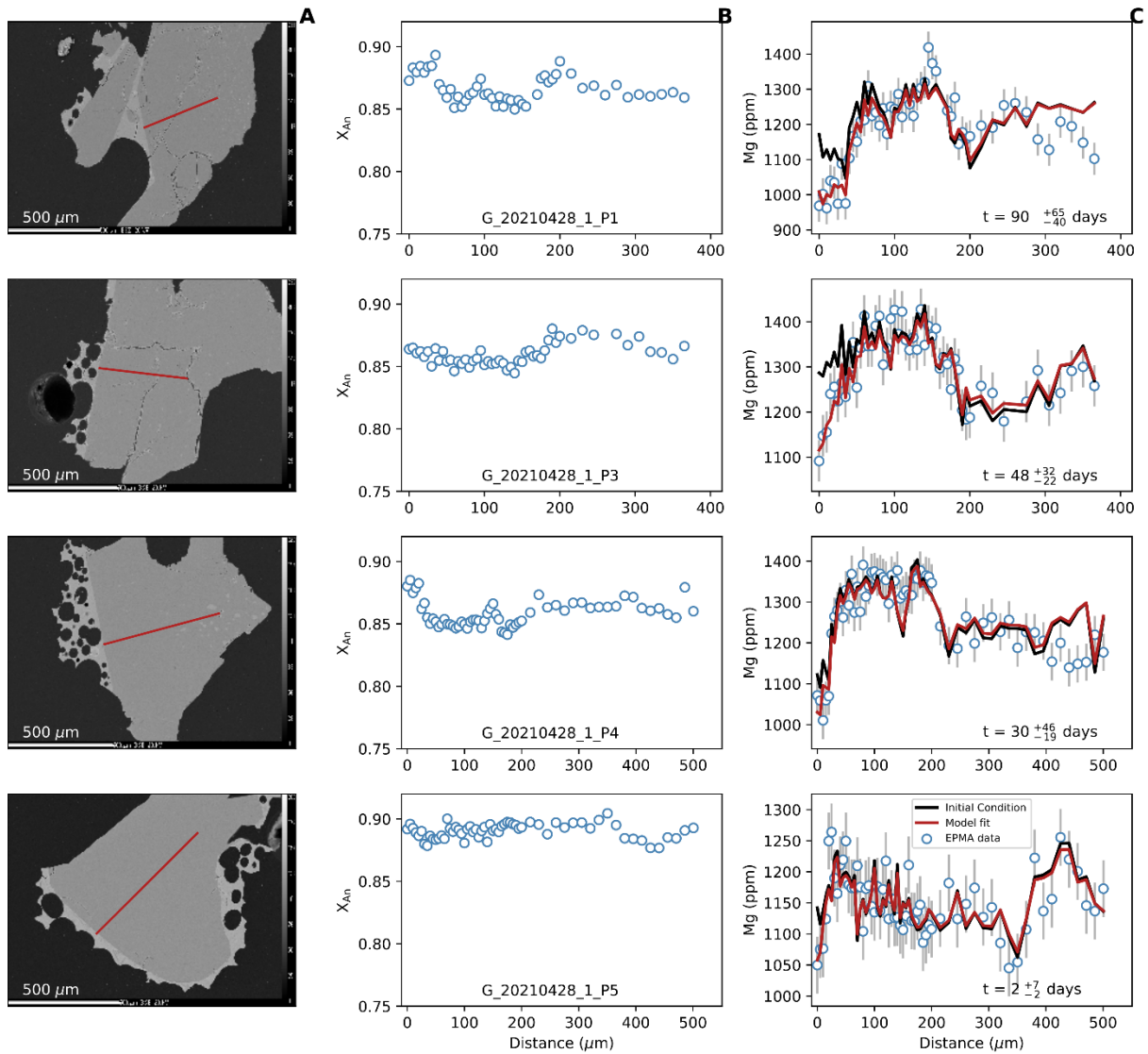


**Fig. S53. Data, initial conditions and best fit plagioclase diffusion models – April 28, 2021.**  
Caption the same as Supplemental Figure S43.

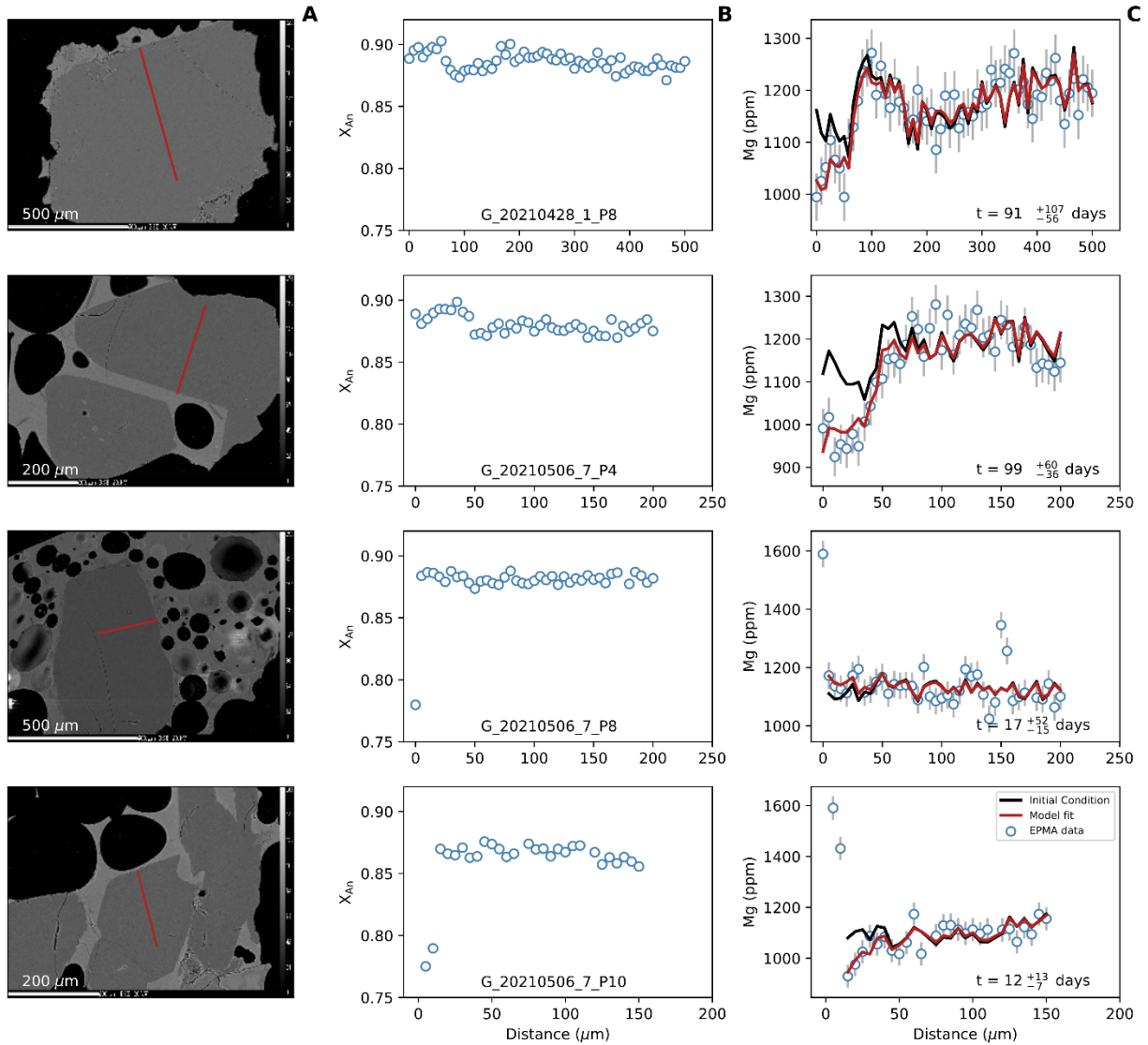


**Fig. S54. Data, initial conditions and best fit plagioclase diffusion models – May 06, 2021**  
Caption the same as Supplemental Figure S43.

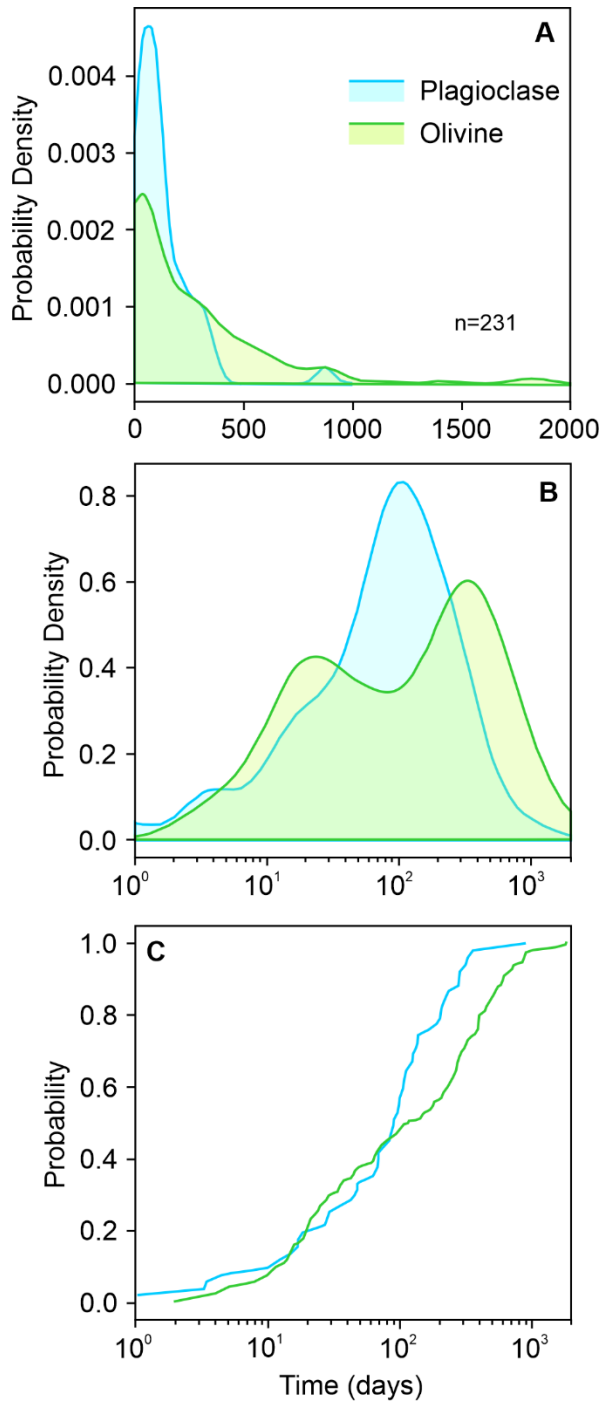


**Fig. S55. Timescale of deep magma mobilization.** Timescale distributions for olivine (green) and plagioclase (blue) macrocrysts modeled using Autodiff (Couperthwaite et al., 2021 and 2020; Pankhurst et al., 2018; Allan et al., 2017; Hartley et al., 2016) and DFENS (Mutch et al., 2021, 2019a, 2019b). (A and B) Kernel density estimates (KDEs) for olivine and plagioclase populations. The bandwidth for each KDE was calculated using Silverman’s rule (Mutch et al., 2021). (C) Cumulative density functions (CDFs) for olivine and plagioclase populations.

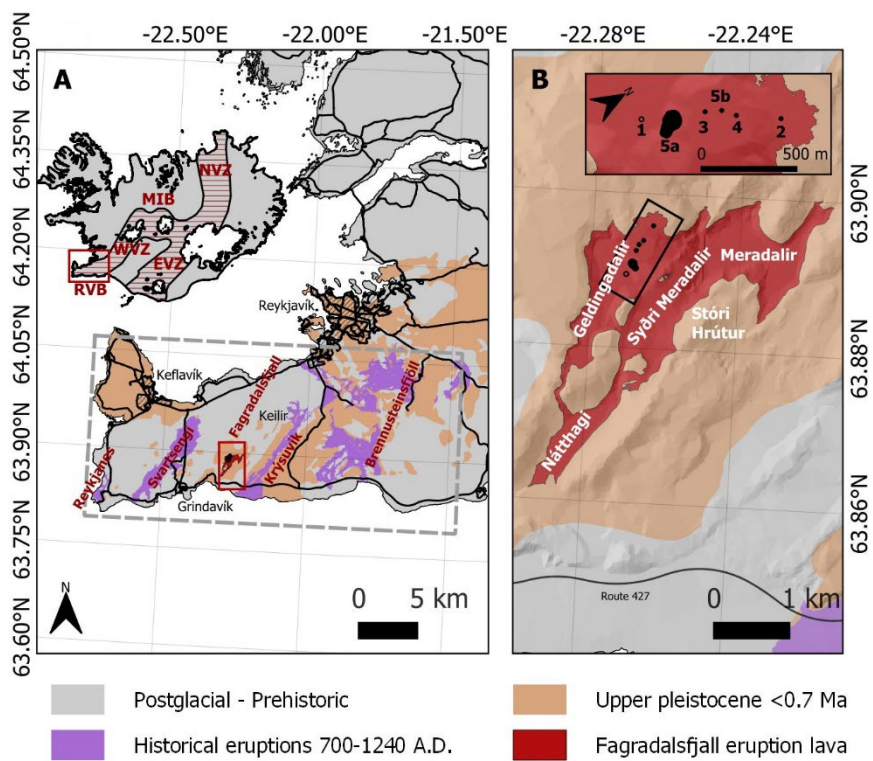


**Fig. S56. (A) Location and (b) flow map.** Grey box highlights the area the seismic data depicted in figure 3 are derived from.

## **Data Sets S1-S7. (in a Separate Excel file)**

### **Data S1.**

Sample information including sample type, eruption/ collection date and sample locations.

### **Data S2.**

Olivine electron backscatter diffraction (EBSD) and orientation data including trends of analytical traverses and angles between the EPMA profiles and the main crystallographic axis in olivine. These angles are incorporated into the anisotropy calculation used to determine the apparent diffusivity along the measured profiles.

### **Data S3.**

Compositional data of olivine. EMPA profile data in wt% including calculated mineral formulae for each point using stoichiometry. Forsterite content is presented as mol%.

### **Data S4.**

Compositional data of plagioclase. EMPA profile data in wt%. Mg data is presented as parts per million (ppm). Anorthite content is given in mol%.

### **Data S5.**

Olivine diffusion timescale data including  $1\sigma$  errors. Two different sets of initial and boundary conditions are used. Step function: Initially stranded (step) profile, interdiffusion is contained entirely within the crystal between two domains of differing but initially uniform forsterite content. Edge-buffered: Initially homogeneous crystal is changed by diffusive interaction with melt at the crystal margin, without any considerations of crystal growth. The higher diffusivity in the melt is represented through a fixed composition at the external margin of the crystal. Inner and outer boundary compositions are also shown. All timescales presented are relative to the time of eruption. For crystals with multiple modellable boundaries [denoted "outer" (rimward) and "inner" (coreward)] the timescale presented for crystal cores is the combined times of residence at  $1236^{\circ}\text{C}$  and at  $1200^{\circ}\text{C}$ . To determine the residence time at  $1236^{\circ}\text{C}$ , the rim residence time (denoted "outer" in most cases) was deducted from the core residence time (denoted "inner").

### **Data S6.**

Plagioclase median timescales and  $1\sigma$  errors obtained from the posterior distributions of the Nested Sampling Bayesian inversion conducted on each plagioclase profile. Diffusion data of Faak et al. (2013) have been used.

### **Data S7.**

Seismic data measured between January 2016 and August 2021 at Fagradalsfjall on the Reykjanes Peninsula, SW Iceland. Data include date/time, depth, location of seismic foci, local moment magnitude ( $M_{wl}$ ), energy and seismic moment release. It also contains the cumulative energy and seismic moment release and the cumulative number of earthquakes. Data from Icelandic Met Office (IMO) seismic catalogue (e.g. Böðvarsson et al., 1999; Icelandic Met Office (Veðurstofa Íslands). <https://skjalftalisa.vedur.is/>).

### **Data S8.**

Mineral-melt equilibrium data calculated using average glass compositions of early erupted lava (20<sup>th</sup>, 21<sup>st</sup> and 23<sup>rd</sup> 2020) and tephra (24<sup>th</sup> March 2020) samples and tephra samples from fire fountaining episodes (28<sup>th</sup> April and 06<sup>th</sup> May 2020).

## REFERENCES CITED

- Allan, A.S.R. et al., 2017, A cascade of magmatic events during the assembly and eruption of a super-sized magma body: *Contributions to Mineralogy and Petrology*, v. 172, 49, doi: 10.1007/s00410-017-1367-8.
- Alnæs, M. et al., 2008, The FEniCS project version 1.5: *Archive of Numerical Software*, v. 3, pp. 9-23.
- Árnadóttir, T., Geirsson, H., Jiang, W., 2008, Crustal deformation in Iceland: plate spreading and earthquake deformation: *Jökull*, v. 58, pp. 59-74.
- Bindeman, Y.N. et al., 2022, Diverse mantle components with invariant oxygen isotopes in the 2021 Fagradalsfjall eruption, Iceland: *Nature Communications*, v. 13, 3737, doi: 10.1038/s41467-022-31348-7
- Buchner, J. et al., 2014, X-ray spectral modelling of the AGN obscuring region in the CDFS: Bayesian model selection and catalogue: *Astronomy & Astrophysics*, v. 564, p. A125, doi: 10.1051/0004-6361/201322971.
- Chakraborty, S., 2010, Diffusion coefficients in olivine, wadsleyite and ringwoodite: *Reviews in Mineralogy and Geochemistry*, v. 72, pp. 603-639, doi: 10.2138/rmg.2010.72.13.
- Clifton, A.E., Kattenhorn, S.A., 2006, Structural architecture of a highly oblique divergent plate boundary segment: *Tectonophysics*, v. 419, pp. 27-40, doi: 10.1016/j.tecto.2006.03.016.
- Costa, F., Morgan, D.J., 2010, “Time constraints from chemical equilibration in magmatic crystals” in *Timescales of Magmatic Processes: From Core to Atmosphere*, A. Dosseto, S. P. Turner, J. A. van Orman, Eds. (Wiley-Blackwell, 2010), pp.125-159.
- Costa, F., Chakraborty, S., 2004, Decadal time gaps between mafic intrusion and silicic eruption obtained from chemical zoning patterns in olivine: *Earth and Planetary Science Letters*, v. 227, pp. 517-530, doi: 10.1016/j.epsl.2004.08.011.
- Couperthwaite, F.K., Morgan, D.J., Pankhurst, M.J., Lee, P.D., Day, J.M.D., 2021, Reducing epistemic and model uncertainty in ionic inter-diffusion chronology: A 3D observation and dynamic modeling approach using olivine from Piton de la Fournaise, La Réunion: *American Mineralogist*, v. 106, pp. 481-494, doi: 10.2138/am-2021-7296CCBY.
- Dohmen, R., Chakraborty, S., 2007, Fe-Mg diffusion in olivine II: point defect chemistry, change of diffusion mechanisms and a model for calculation of diffusion coefficients in natural olivine: *Physics and Chemistry of Minerals*, v. 34, pp. 409-430, doi: 10.1007/s00269-007-0158-6.
- Dohmen, R., Becker, H.-W., Chakraborty, S., 2007, Fe-Mg diffusion in olivine I: experimental determination between 700 and 1,200 °C as a function of composition, crystal orientation and oxygen fugacity: *Physics and Chemistry of Minerals*, v. 34, pp. 389-407, doi: 10.1007/s00269-007-0157-7.
- Faak, K., Chakraborty, S., Coogan, L.A., 2013, Mg in plagioclase: Experimental calibration of a new geothermometer and diffusion coefficients: *Geochimica et Cosmochimica Acta*, v. 123, pp. 195-217, doi: 10.1016/j.gca.2013.05.009.

- Feroz, F., Hobson, M., Bridges, M., 2009, MultiNest: an efficient and robust Bayesian inference tool for cosmology and particle physics: *Monthly Notices of the Royal Astronomical Society*, v. 398, pp. 1601-1614, doi: 10.1111/j.1365-2966.2009.14548.x.
- Gee, M.A.M., Taylor, R.N., Thirlwall, M.F., Murton, B. J., 1998, Glacioisostasy controls chemical and isotopic characteristics of tholeiites from the Reykjanes Peninsula, SW Iceland: *Earth and Planetary Science Letters*, v. 164, pp. 1-5, doi: 10.1016/S0012-821X(98)00246-5.
- Ghiorso, M.S., Sack, R.O., 1995, Chemical mass transfer in magmatic processes IV. A revised and internally consistent thermodynamic model for the interpolation and extrapolation of liquid-solid equilibria in magmatic systems at elevated temperatures and pressures: *Contributions to Mineralogy and Petrology*, v. 119, pp. 197-212, doi: 10.1007/BF00307281.
- Gualda, G.A.R., Ghiorso, M.S., Lemons, R.V., Carley, T.L., 2012, Rhyolite-MELTS: a modified calibration of melts optimized for silica-rich, fluid-bearing magmatic systems: *Journal of Petrology*, v. 53, pp. 875-890, doi: 10.1093/petrology/egr080.
- Hanks, T. C. & Kanamori, H., 1979, A moment magnitude scale: *Journal of Geophysical Research Solid Earth*, v. 84, pp. 2348-2350, doi: 10.1029/JB084iB05p02348.
- Hartley, M.E., Bali, E., MacLennan, J., Neave, D.A., Halldórsson, S., 2018, Melt inclusion constraints on petrogenesis of the 2014-2015 Holuhraun eruption, Iceland: *Contributions to Mineralogy and Petrology*, v. 173, p.10, doi: 10.1007/s00410-017-1435-0.
- Hreinsdóttir, S., Einarsson, P., Sigmundsson, F., 2001, Crustal deformation at the oblique spreading Reykjanes peninsula: GPS measurements from 1993-1998: *Journal of Geophysical Research*, v. 106, pp. 13803-13816, doi: 10.1029/2001JB000428.
- Jakobsson, S.J., Jónasson, K., Sigurdsson, L.A., 2008, The three igneous rock series of Iceland: *Jökull*, v. 58, pp. 117-138.
- Jakobsson, S.P., Jónsson, J., Shido, F., 1978, Petrology of the western Reykjanes peninsula, Iceland: *Journal of Petrology*, v. 19, pp. 669-705, doi: 10.1093/petrology/19.4.669.
- Jónsson, J., 1978, Jarðfræðikort af Reykjaneskaga (geological map of Reykjanes peninsula), Orkustofnun JHD (Iceland Energy Authority). 7831 303 p., 30 plates, 20 map sheets 1:25,000.
- Mollo, S., Putirka, K.D., Misiti, V., Soligo, M., Scarlato, P., 2013, A new test for equilibrium based on clinopyroxene-melt pairs: clues on the solidification temperatures of etnean alkaline melts at post-eruptive conditions: *Chemical Geology*, v. 352, pp. 92-100, doi: 10.1016/j.chemgeo.2013.05.026.
- Neave, D.A. et al., 2019, Clinopyroxene-liquid equilibria and geothermobarometry in natural and experimental tholeiites: the 2014-2015 Holuhraun eruption, Iceland: *Journal of Petrology*, v. 60, pp. 1653-1680, doi: 10.1093/petrology/egz042.
- Neave, D.A., Putirka, K.D., 2017, A new clinopyroxene-liquid barometer, and implications for magma storage pressures under Icelandic rift zones: *American Mineralogist*, v. 102, pp. 777-794, doi: 10.2138/am-2017-5968.
- Nikolaev, G.A., Ariskin, A.A., Barmina, G.S., Nazarov, M.A., Almeev, R.R., 2016, Test of the Ballhaus-Berry-Green ol-opx-sp oxybarometer and calibration of a new equation for

- estimating the redox state of melts saturated with olivine and spinel: *Geochemistry International*, v. 54, pp. 301-320, doi: 10.1134/S0016702916040078.
- Peate, D.W. et al., 2009, Historic magmatism on the Reykjanes peninsula, Iceland: a snap-shot of melt generation at a ridge segment: *Contributions to Mineralogy and Petrology*, v. 157, pp. 359-382, doi: 10.1007/s00410-008-0339-4.
- Pedersen, G. B. M. et al., 2022, Volume, effusion rate, and lava transport during the 2021 Fagradalsfjall eruption: Results from near real-time photogrammetric monitoring: *Geophysical Research Letters*, v. 49, e2021GL097125, doi: 10.1029/2021GL097125.
- Prior, D.J. et al., 1999, The application of electron backscatter diffraction and orientation contrast imaging in the SEM to textural problems in rocks: *American Mineralogist*, v. 84, pp. 1741-1759, doi: 10.2138/am-1999-11-1204.
- Putirka, K.D., 2008, Thermometers and barometers for volcanic systems: *Reviews in Mineralogy and Geochemistry*, v. 69, pp. 61-120, doi: 10.2138/rmg.2008.69.3.
- Sæmundsson, K. et al., 2016, Geological Map of Southwest Iceland, 1:100.000. 2nd ed. Iceland GeoSurvey, Reykjavik.
- Sigmundsson, F., et al., 2022, Deformation and seismicity decline before the 2021 Fagradalsfjall eruption: *Nature*, v. 609, pp. 523-528, doi: 10.1038/s41586-022-05083-4.
- Sinton, J., Grönvold, K., Saemundsson, K., 2005, Postglacial eruptive history of the western volcanic zone, Iceland: *Geochemistry Geophysics Geosystems*, v. 6, Q12009, doi: 10.1029/2005GC001021.
- Thordarson, T., Höskuldsson, Á., 2008, Postglacial volcanism in Iceland: *Jökull*, v. 58, pp. 197-228.
- Van der Meer, Q.H.A., Bali, E., Guðfinnsson, G.H., Kahl, M., Rasmussen, M.B., 2021, Warm and slightly reduced mantle under the off-rift Snæfellsnes volcanic zone, Iceland: *Journal of Petrology*, v. 62, egab057, doi: 10.1093/petrology/egab057.
- Van Orman, J.A., Cherniak, D.J., Kita, N. T., 2014, Magnesium diffusion in plagioclase: dependence on composition, and implications for thermal resetting of the <sup>26</sup>Al-<sup>26</sup>Mg early solar system chronometer: *Earth and Planetary Science Letters*, v. 385, pp. 79-88, doi: 10.1016/j.epsl.2013.10.026.
- Yang, H.-J., Kinzler, R.J., Grove, T.L., 1996, Experiments and models of anhydrous, basaltic olivine-plagioclase-augite saturated melts from 0.001 to 10 kbar: *Contributions to Mineralogy and Petrology*, v. 124, pp. 1-18, doi: 10.1007/s004100050169.